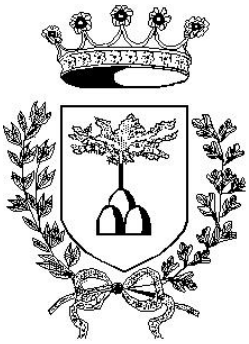

Università degli Studi di Ferrara
Dipartimento di Fisica e Scienze della Terra

Dottorato di Ricerca in

Fisica

Settore Scientifico Disciplinare

FIS/01

Coordinatore

Prof. V. Guidi

Innovative approaches for Monte Carlo simulations of orientational effects in crystals and their experimental verification

Tutore
Prof. Vincenzo Guidi

Dottorando
Dott. Enrico Bagli

Dottorato di Ricerca
XXVI Ciclo. 2011-2013

Contents

Introduction

Interaction of either charged or neutral particles with crystals is an area of science under development. Coherent effects of ultra-relativistic particles in crystals allow manipulating particle trajectories thanks to the strong electrical field generated between atomic planes and axes [1–3]. Important examples of interaction of neutral particles in crystals are production of electron-positron pairs and birefringence of high energy gamma quanta [4, 5]. Radiation emission due to curved trajectories in bent crystals has been studied to enhance photon production through bremsstrahlung, channeling radiation, PXR, undulators [6–10] and recently through volume reflection and multiple volume reflection [11, 12]. Inelastic nuclear interaction rate has been proved to be modified by channeling and volume reflection [13]. Various applications of orientational phenomena with crystals have been proposed and investigated such as beam steering [14], extraction and collimation [15–18] in circular accelerators, as well as splitting and focusing [19] of external beams.

On the strength of recent optimization in the manufacture techniques [20, 21] and crystal holder [22], bent crystals have also been proposed as beam collimator [23] and extractor [24, 25] for LHC. In deed, reduction of nuclear interaction rate for channeled positive particle in bent crystals [13] has been proved to lower beam losses in all the SPS synchrotron [26]. In addition, crystals were proved to work in the same way also for Pb ions [27]. Beam extraction with bent crystals take advantage of no-need of electric current and maintenance cost to deflect a particle beam, especially at high-energy.

Coherent effects for interaction of particles with aligned structures always exploited opportunity furnished by the most advanced calculators and calculation methods of the current period. In 1963 Oen and Robinson [28] investigated particle behavior in crystal lattices using an IBM 7090 and noticed that particles moving near planes and axes had anomalously long ranges. Their Monte Carlo code was based on binary collision model and was capable of predicting the experimental results observed in 1963 [29]. In 1965 Lindhard showed [30] that the motion of relativistic charged particles under channeling condition is well approximated with classical physics equations and, as a consequence,

also the potential and its related quantities. In particular, Lindhard proposed the so-called continuous potential approximation [30]. By adopting the continuous approximation many codes for the integration of particles trajectories in crystals have been developed [31–35]. As an example of the capability of such method, in 1987 Vorobiev and Taratin [3] predicted the volume reflection phenomenon in bent crystal which was firstly observed only after nineteen years in 2006 by the H8RD22 collaboration [36] . In the last years experiments at CERN external lines [13, 37–52] have made available a large amount of high-resolution data thanks to the possibility to track trajectories of ultra-relativistic particles with μrad resolution [53]. Such improvement in experimental knowledge of orientational effects has led to the development of Monte Carlo simulation based on the experimental cross sections of orientational phenomena [50, 54]. In 2013 a model for the simulation of planar channeling of positive particles in bent crystal has been proposed [55] for Fluka [56]. The model relies on the continuous potential approximation for the potential.

In this work we will present some of the experimental results obtained in the three experiments and the developed Monte Carlo codes used for the simulation and the analysis of the results.

In the last years, the Ferrara Sensor and Semiconductor Labs have taken part to three experiments on coherent interactions with high-energy charged particles, UA9, COHERENT and ICERAD experiments. The UA9 experiment is devoted to the fabrication and the test of a prototype of crystal collimator for the SPS synchrotron. Main goal of UA9 is to adopt a crystal collimator to reduce the beam losses in the LHC, in order to increase the available luminosity and to collimate high-Z ion-beams. The COHERENT project studies orientational phenomena in complex atomic structures and to observe new orientational phenomena for particles with hundreds of GeV/c momentum. Aim of the project is to demonstrate the capability to search for new materials and effects to improve manipulation via coherent interactions. The ICERAD project is devoted to the study of radiation emitted by particles under orientational phenomena and to study orientational phenomena at hundreds of MeV at the Mainz Microtron (MAMI). The first goal is to prove the possibility to deflect sub-GeV electrons with bent crystals through planar channeling at full bending angle.

Many ways have been explored to simulate coherent interactions. The `DYNECHARM++` code has been developed to simulate and emulate the results of the interaction. The core of the code is based on the integration of the equation of motion for charged particles under continuous potential approximation. The electrical characteristics are computed accordingly to the models adopted in the ECHARM code. Thanks to the object-oriented capability of C++ programming language, expansions can be added to the original in

order to implement defects or undulating structures. A specific version for the Xeon Phi coprocessors has been studied to exploit parallelization at thread and vector levels.

An addition to the Geant4 toolkit has been written to implement orientational effects into Geant4 and study the modification of other physics processes due to channeling and related effects. A model for the orientational effects in crystals has been specifically studied for Geant4 in order to limit the computational cost with respect to the model used for `DYNECHARM++`. The addition to the Geant4 toolkit has been developed in collaboration with the Geant4 team of SLAC National Accelerator Laboratories during a five months visiting period at SLAC.

List of published articles

The work presented in this thesis is based on the following articles and proceedings:

A1: E Bagli, V Guidi, V A Maisheev, Phys. Rev. E **81** (2010) 026708, *Calculation of the potential for interaction of particles with complex atomic structures*

A2: W Scandale *et al*, Eur. Phys. Lett. **93** (2011) 56002, *Observation of multiple volume reflection by different planes in one bent silicon crystal for high-energy negative particles*

A3: D De Salvador *et al*, Applied Phys. Lett. **98** (2011) 234102, *Steering of an ultrarelativistic proton beam by a bent germanium crystal*

A4: W Scandale *et al*, Phys. Lett. B **703** (2011) 547, *Comparative results on collimation of the SPS beam of protons and Pb ions with bent crystals*

A5: E Bagli *et al*, JINST **7** (2012) P04002, *A topologically connected multistrip crystal for efficient steering of high-energy beam*

A6: W Scandale *et al*, Phys. Lett. B **719** (2013) 70, *Measurement of the dechanneling length for high-energy negative pions*

A7: E Bagli, V Guidi, Nucl. Instr. Meth. B **309** (2013) 124, *DYNECHARM++: a toolkit to simulate coherent interactions of high-energy charged particles in complex structures*

A8: E Bagli *et al*, Phys. Rev. Lett. **110** (2013) 175502, *Coherent Effects of High-Energy Particles in a Graded $Si_{1-x}Ge_x$ Crystal*

A9: D De Salvador *et al*, J. App. Phys. **114** (2013) 154902, *Highly bent (110) Ge crystals for efficient steering of ultrarelativistic beams*

A10: E Bagli *et al*, Eur. Phys. J. C (2014) *to be published*, *Steering efficiency of a ultrarelativistic proton beam in a thin bent crystal*

A11: A Mazzolari *et al*, submitted to Phys. Rev. Lett. (2014), *Steering of a sub-GeV electron beam through planar channeling enhanced by rechanneling*

A12: E Bagli, V Guidi, V A Maisheev, Proc. of 1st Int. Part. Acc. Conf.: IPAC'10 (2010) TUPEA070, *ECHARM - a Software for Calculation of Physical Quantities of Interest in Coherent Interaction of Relativistic Particles with Crystals*

A13: D De Salvador *et al*, AIP Conf. Proc. **1530** (2013) 103, *Planar channeling steering of an ultrarelativistic proton beam through a bent germanium crystal*

Articles and proceeding not included in the thesis published before and during the PhD:

N1: W Scandale *et al*, Phys. Lett. B **680** (2009) 129, *High-efficiency deflection of high-energy negative particles through axial channeling in a bent crystal*

N2: W Scandale *et al*, Phys. Lett. B **681** (2009) 233, *Observation of channeling and volume reflection in bent crystals for high-energy negative particles*

N3: W Scandale *et al*, Phys. Lett. B **682** (2009) 274, *First observation of multiple volume reflection by different planes in one bent silicon crystal for high-energy protons*

N4: W Scandale *et al*, Phys. Lett. B **688** (2010) 284, *Multiple volume reflections of high-energy protons in a sequence of bent silicon crystals assisted by volume capture*

N5: W Scandale *et al*, Nucl. Instr. Meth. B **268** (2010) 2655, *Probability of inelastic nuclear interactions of high-energy protons in a bent crystal*

N6: W Scandale *et al*, Phys. Lett. B **692** (2010) 78, *First results on the SPS beam collimation with bent crystals*

N7: W Scandale *et al*, Phys. Lett. B **693** (2010) 545, *Deflection of high-energy negative particles in a bent crystal through axial channeling and multiple volume reflection stimulated by doughnut scattering*

N8: W Scandale *et al*, Phys. Lett. B **701** (2011) 180, *Observation of parametric X-rays produced by 400 GeV/c protons in bent crystals*

N9: W Scandale *et al*, JINST **6** (2011) T10002, *The UA9 experimental layout*

N10: D Lietti *et al*, Nucl. Instr. Meth. B **283** (2012) 84, *Radiation emission phenomena in bent silicon crystals: Theoretical and experimental studies with 120 GeV/c positrons*

N11: W Scandale *et al*, Phys. Lett. B **714** (2012) 231, *Strong reduction of the off-momentum halo in crystal assisted collimation of the SPS beam*

N12: L Bandiera *et al*, Nucl. Instr. Meth. B **309** (2013) 135, *On the radiation accompanying volume reflection*

N13: W Scandale *et al*, Phys. Lett. B **726** (2013) 182, *Optimization of the crystal assisted collimation of the SPS beam*

N14: L Bandiera *et al*, Phys. Rev. Lett. **111** (2013) 255502, *Broad and Intense Radiation Accompanying Multiple Volume Reflection of Ultrarelativistic Electrons in a Bent Crystal*

N15: V Guidi *et al.*, Proc. of 1st Int. Part. Acc. Conf.: IPAC'10 (2010) THPD052, *Manipulation of Negatively Charged Beams via Coherent Effects in Bent Crystals*

N16: A Mazzolari *et al.*, Proc. of 1st Int. Part. Acc. Conf.: IPAC'10 (2010) TUPEC080, *Fabrication of Silicon Strip Crystals for UA9 Experiment*

N17: A Mazzolari *et al.*, Proc. of Part. Acc. Conf.: PAC'11 (2011) MOODN3, *Advanced bent crystal collimation studies at the Tevatron (T-980)*

Chapter 1

Orientational effects in crystals

This chapter is dedicated to an overview of the main concepts of coherent interactions for a charged particles moving in a crystal [57].

In 1912 Stark [58] had the first idea that the atomic order in crystal may be important for this type of processes, but these old ideas of the directional effects for a charged particle moving in a crystal were dormant until the early 1960s, when the channeling effect was discovered in computer simulations [28] and experiments [29], which observed too much long ranges of ions in crystal. The theoretical explanation of the channeling effects has been given by Lindhard [30]: by channeling is meant that a particle path near the channel center along a major axis (plane) in a crystal may have a certain stability.

In the 1976 Tsyganov proposed to use slightly bent monocrystals to deflect high-energy particle beams [1]; his idea was that a channeled particle would follow the direction of the bent atomic planes (or axes), thus deviating from its initial direction by an angle equal to the bending angle of the crystal. In 1979 the possibility of steering beams of charged particles using bent crystal was first demonstrated in an experiment on the deflection of 8.4 GeV protons beam extracted from the synchrophasotron of the Laboratory of High Energies, JINR [14].

In the following years many other effects was discovered studying through Monte Carlo simulations bent crystals such as volume capture and volume reflection. The first one consists in the phenomenon of capturing a charged particle into a channeling mode in the depth of a bent single crystal in the region where the particle trajectories are tangential to the crystallographic planes; it was discovered in 1982 using a beam of 1 GeV protons [59–61]. The second one consists in the deflection of particles tangent to the crystal curvature in a direction opposite to the crystal bending and hence opposite to the one of the channeled particles deflection; this effect called volume reflection was found in computer simulations

in 1987 [3] and experimentally proved in 2006 [36].

1.1 Coherent Interactions in Straight Crystals

In this section the theoretical explanation of the channeling phenomenon given by Lindhard is presented [30]. He has shown that when a charged particle has a small incident angle with respect to the crystallographic axis (or plane) the successive collisions of the particle with the lattice atoms are correlated, i.e. coherent scattering, and hence one has to consider the interaction of the charged particle with the atomic string (plane).

Any charged particle traversing an amorphous medium (characterized by homogeneity, isotropy and randomness) or a misaligned crystal makes uncorrelated collisions with single atoms. These collisions may be of different nature , depending on different impact parameters; the most common are angular scattering in multiple collisions with atomic nuclei and energy loss in collisions with atomic electrons. So in a random system the slowing-down process is independent of direction and hence the probability distribution in energy loss and scattering angle depends only on the mass per cm^2 penetrated, and it has to be computed in a familiar way from single collisions. This is essentially a gas picture, and may be called a random system, implying homogeneity, isotropy and random collisions. However, it is important to realize that the approximation of a random system is not confined to randomly distributed atoms or molecules, but may be also applied to media with lattice structure.

An anisotropy due to lattice structure can thus result in some kind of correlations between collisions, i.e.coherent interactions. A single crystal is a typical example of a medium in which directional effect in stopping might appear, due to both inhomogeneity, anisotropy and lack of randomness. In fact, a crystal is a regular arrangement of atoms located on a lattice so that, depending on the point of view of the observer, the atoms are arranged in strings or plane.

The directional effects for charged particles traversing crystal were found for a number of processes requiring a small impact parameter in a particle-atom collision, e.g., nuclear reactions, large-angle scattering and energy loss. We may classify directional effects for charged particles moving through single crystal using two labels: ungoverned motion and governed motion. By ungoverned motion is meant the approximation where the path of the particle may be assumed to be essentially unaffected by the structure of the substance. Governed motion means that a path deviates definitely from the one in a random system, because the path is determined by the structure of the medium. Governed motion leads

to more fundamental changes in physical processes, whereas ungoverned motion just show fluctuations in physical effects due to correlations.

For treatment of possible governed motion the scattering angle of the particle may be assumed to be small, because scattering by large angles would imply that the original direction is completely lost, as well as correlations associated with direction. The scattering of the particle is due to nuclear collisions, causing the interaction with the charge distribution of an atom as a whole through nearly elastic collision. Moreover, since collision requires that the particle comes close to the atom, strong correlations between collisions occur if the particle moves at a small angle with a row of atoms; if it passes close to one atom in a row, it must also passes close to the neighboring atoms in the same row. This leads us to the concept of string of atoms that is characterized merely by the constant distance of separation, d, of atoms placed on a straight line; we assume this as the perfect string.

When the motion of a charged particle is aligned (or at a small angle) with a string (or plane), a coherent scattering with the atoms of the string (or plane) can occur. In the low-angle approximation we can replace the potentials of the single atoms with an averaged continuous potential. The atomic string (plane) in the continuum approximation gently steers a particle away from the atoms, therefore suppressing the encounters with small impact parameters listed above. The channeling phenomenon is due to the fact that the fields of the atomic axes and planes form the potential wells, where the particle may be trapped. Particles can be trapped between planes or axes, under planar or axial channeling, respectively.

1.1.1 Continuous approximation

The continuous approximation by Lindhard was developed to describe channeling and its related phenomena, but can be extended to all orientational phenomena because the same approximations hold. Coherent effects are primary phenomena, i.e., they govern path of particles, and not secondary ones, which are determined by the path. Thus, four basic assumptions can be introduced for particles under orientational effects. First, angles of scattering may be assumed to be small. Indeed, scattering at large angles imply complete lost of the original direction. Secondly, because particle move at small angle with respect to an aligned pattern of atoms and collisions with atoms in a crystal demand proximity, correlations between collisions occur. Third, since coherent length l of scattering process ($l = 2E/q^2$, where E is the particle energy and q the transferred momentum) is larger than lattice constant, classical picture can be adopted. Fourth, idealized case of a perfect lattice may be used as a first approximation.

By following such assumptions, the continuous approximation can be inferred. Under such approximation, the potential of a plane of atoms $U(c)$ can be averaged along direction parallel to plane directions. Angle θ has to be greater than scattering angle ϕ with a single atom

$$U(x) = Nd_p \int \int_{-\infty}^{+\infty} dydzV(\mathbf{r}) \tag{1.1}$$

where d_p is the interplanar distance, N is the atomic density and $V(\mathbf{r})$ is the potential of a particle-atom interaction.

If the distance between the particle and the atom $r = \sqrt{x^2 + y^2 + z^2}$ is not very much larger that a_{TF} (the screening length of the particle-atom interaction), the Thomas-Fermi-like potential $V(\mathbf{r})$ can be described as

$$V_{TF}(r) = \frac{Z_1 Z_2 e^2}{r} \Phi\left(\frac{r}{a_{TF}}\right) \tag{1.2}$$

where Z_1 is the particle charge and Z_2 is the atomic number of the crystalline medium, e is the elementary charge, $\Phi(r/a_{TF})$ is the screening function. In the following it is often implicitly understood that $Z_1 \ll Z_2$ so that

$$a_{TF} = 0.8853 a_B \left(Z_1^{\frac{2}{3}} + Z_2^{\frac{2}{3}}\right)^{-\frac{1}{2}} \tag{1.3}$$

where $a_B = 0.529$Å is the Bohr radius. By using the Thomas-Fermi-like potential, interplanar potential becomes

$$U(x) = 2\pi N d_p Z_1 Z_2 e^2 a_{TF} \exp\left(-\frac{x}{a_{TF}}\right) = U_{max} \exp\left(-\frac{x}{a_{TF}}\right) \tag{1.4}$$

where U_{max} is the maximum of the potential.

Basis of the approximation relies on the qualitative assumption that many consecutive atoms contribute to deflection of a particle trajectory. Thus, for relativistic particles, the time of collision $\Delta t \approx c\Delta z$ multiplied by momentum component parallel to plane direction, $p_z \sim p\cos\theta$, has to be large compared to distance d_z between atoms along particle direction, where p is particle momentum, p_z is momentum component along particle direction and θ is angle between particle direction and crystal plane orientation. Since collision time is approximately $\sim r_{min}/(v\sin\theta)$, where r_{min} is the minimal distance of approach, the condition for continuous approximation holds

$$\frac{\Delta z}{c} p\cos\theta \approx \frac{r_{min}}{\theta} \gg d_z \tag{1.5}$$

In the most restrictive form r_{min} is determined by the condition that kinetic transverse energy can not exceed potential transverse energy at r_{min}.

$$\frac{1}{2}p\beta\theta^2 = U(r_{min}) \tag{1.6}$$

Therefore, from previous equations, a condition can be derived, for which the continuous approximation still valid

$$\frac{a_{TF}}{d_z\theta}\left(1 - \frac{p\beta}{2U_{max}}\theta^2\right) \gg 1 \tag{1.7}$$

Two terms appear in the condition. One refers to Lindhard angle of channeling $\theta_L = \sqrt{2U_{max}/(p\beta)}$, which determines maximum angle for channeling. The other term is more interesting because it implies that $\theta < a_{TF}/d_z \sim 0.5\text{Å}/1\text{Å} \sim 0.5$ is very large compared to θ_L at high-energy. Thus, the continuous approximation is still valid for angle greater than θ_L by imposing that particle does not approach plane center closer than r_{min}.

The continuous potential approximation can be extended to a region closer than r_{min} to atomic position by treating in more detail atomic displacement in the structure. In fact, since crystal temperature is usually higher than 0 K degree, atoms vibrate around their center of mass. By averaging thermal vibration amplitude can be averaged over space and time, probability density function for the position of atoms can be derived. Thus, continuous approximation can be extended to region closer to center of vibration of atoms. Because of the averaging is due to thermal fluctuations, such approximation is not valid at very low temperature and limits for continuous approximation have to be treated carefully.

1.1.2 Potential under continuous approximation

A positive particle feels the effect of a whole plane instead of the individual atoms that compose the plane; in the conditions described before the electric field of two neighboring planes can trap the particle and so it could be channeled between the planes (see Fig. 1.1).

As a first order approximation, let us consider a perfect static lattice with not atomic vibration. Several approximation can be used for the screening functions. By adopting the Lindhard approximation to the screening function

$$\Phi\left(\frac{r}{a_{TF}}\right) = 1 - \left(1 + \frac{3a^2{}_{TF}}{r^2}\right)^{-1/2} \tag{1.8}$$

the planar potential under continuous approximation is

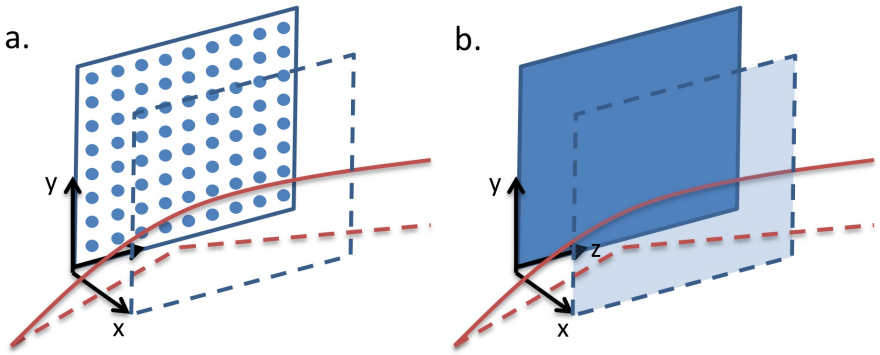

Figure 1.1: a. Trajectory of positive particle moving in a crystal misaligned with respect to the axis but at a small angle with respect to crystallographic plane. b. Continuous potential $U(x)$ is felt by the particle mainly due to the two neighboring planes

$$U_{pl}(x) = 2\pi N d_p Z_1 Z_2 e^2 \left(\sqrt{x^2 + 3{a_{TF}}^2} - x\right) \tag{1.9}$$

The Moliére screening function [62] is widely used and is described by the analytical expression

$$\Phi\left(\frac{r}{a_{TF}}\right) = \sum_i \alpha_i \exp\left(-\frac{\beta_i r}{a_{TF}}\right) \tag{1.10}$$

, where $\alpha = (0.1, 0.55, 0.35)$, $\beta = (6.0, 1.2, 0.3)$ are the Moliére's coefficients . Under such approximation the planar potential holds

$$U_{pl}(x) = 2\pi N d_p Z_1 Z_2 e^2 a_{TF} \sum_{i=1}^{3} \frac{\alpha_i}{\beta_i} \exp\left(-\frac{\beta_i x}{a_T F}\right) \tag{1.11}$$

When the particle travels aligned with a crystal axis it suffers the potential of the atomic row. The axis electric field is stronger than the planar. By averaging along the longitudinal coordinate of the string and by adopting the Lindhard approximation for the screening function, the axial continuous potential holds

$$U_{ax}(r) = \frac{Z_1 Z_2 e^2}{a_i} ln\left(1 + \frac{3{a_{TF}}^2}{r^2}\right) \tag{1.12}$$

where a_i is the interatomic spacing in the string and r is the minimum distance of the particle from the axis.

The above formulas well describe potential for a ideal case. Let us introduce in the calculation the displacement of the lattice due to thermal vibrations of atoms in the struc-

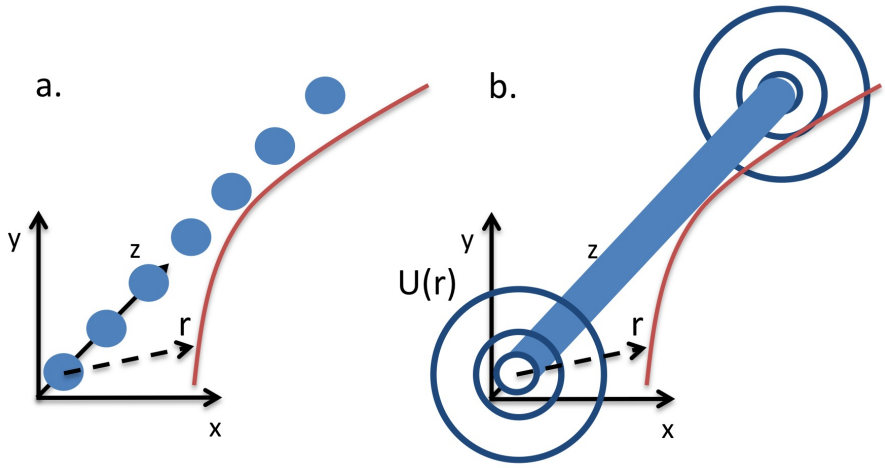

Figure 1.2: a. Trajectory of positive particle moving in a crystal aligned with respect to a crystal axis. b. Continuous potential $U(x)$ is felt by the particle mainly due to the neighboring axis

ture. Thus, the static-lattice potential near the plane has to be modified at a a distance of the order of thermal vibrations root-mean square amplitude u_T. By assuming the independence of vibration for each atom, the isotropy of the displacement, the thermal vibrations can be averaged over space and time. Thus, the position of the nuclei in the atoms can be approximated by a gaussian probability function.

Because the amplitude of thermal vibration is usually small compared to an interatomic distance, the introduction of thermal vibration mainly affects the calculation of the potential near the atomic planes or axes. As an example, the interplanar distance for Si (110) planes is 1.92Å, which is ~ 25 times greater than $u_T = 0.075$Å at 300 K. However, usage of potential averaged over thermal vibration has very important consequences. In particular, such improvement is fundamental to search for the solution of the equation of motion of quasi-channeled particles, which travel over the potential barrier and cross many planes. In fact, the sharp maximum for the ideal case is smoothed to a continuous function for the potential.

If a charged particle moves in a crystal at low-angle with respect to a crystal plane, the potential can be approximated by the sum of the potential of the singles planes. In particular, the major contributions of the two nearest planes dominate. Thus, the potential results

$$U_{pl}(x) \approx U_{pl}(d_p/2 - x) + U_{pl}(d_p/2 + x) - 2U_{pl}(d_p/2) \tag{1.13}$$

where x is expressed in unit of the interplanar distance and $U(0) = 0$. In Fig. 1.3 the planar potential averaged over thermal vibration and the planar potential for the Lindhard and Moliére approximations are shown.

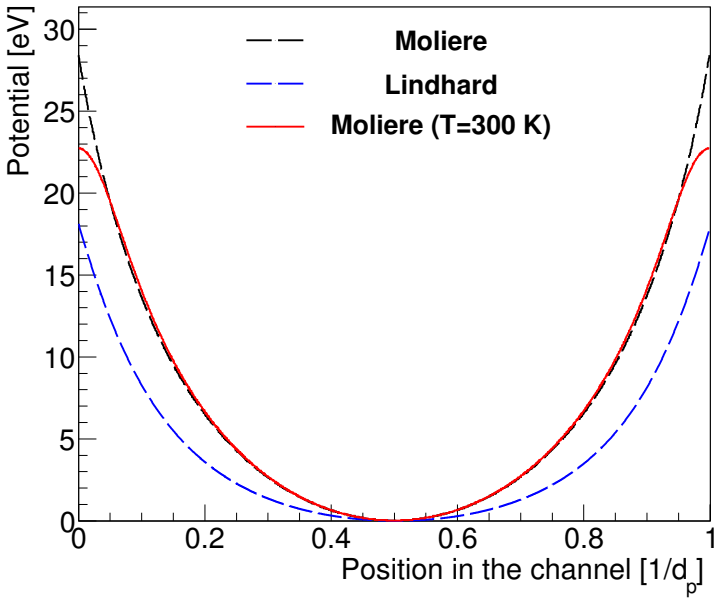

Figure 1.3: The planar continuous potential for the Si(110) planes at 300 K by adopting the Moliére and the Lindhard screening functions and by averaging over thermal vibration using the Moliére screening function.

The most used crystals for channeling experiments are made of Si. In fact, Si can be easily found with low impurity ($< 1/\text{ cm}^2$) thanks to the usage in semiconductor materials and crystal [63]. Si has a diamond lattice structure. In Tab. 1.1 the main parameters for major orientation of Si are shown. Since the interplanar potential is well approximated by a second order curve far from the atomic nuclei, the harmonic approximation $U(x) \simeq U_0(2x/d_p)^2$ is often used for analytic estimations concerning channeling.

Plane	d_p [Å]	a_{TF} [Å]	u_T [Å]	$U(x_c)$ [eV]	$U'(x_c)$ [GeV/cm]
(110)	1.92	0.194	0.075	16	5.7
(111)L	2.35	0.194	0.075	19	5.6
(111)S	0.78	0.194	0.075	4.2	3.5

Table 1.1: Parameters of some planes of Si. The potentials U are given at the distance $x_c = d_p/2 - 2u_T$ in the Moliére approximation.

1.1.3 Motion of charged particles under planar channeling

The transverse motion of a particle incident at small angle with respect to one of the crystal axes or planes is governed by the continuous potential of the crystal lattice. A charged particle moving in a crystal is in planar channeling condition if it has a transverse momentum that is not sufficient to exceed the barrier to a neighboring channel, in this case the particle can not escape from the channel.

The interaction of the channeled particle with a medium is very different from a particle interaction with an amorphous one or a misaligned crystal [57]. There are two main sources of energy loss by a charged particle: electronic stopping and nuclear stopping. Electronic stopping is due to electronic inelastic collisions, where the particle excites or ejects atomic electrons, with loss of energy [30]. The corresponding momentum transfered is small because electrons are light particles. Nuclear stopping arises from nearly-elastic collisions with atom, with transfer both energy and momentum. We assume here that the nuclei are much more massive than the incident particles so that the small energy transfer to the nucleus is negligible [64]. Ignoring spin effects and screening these collisions are individually governed by the well-known Rutherford formula where $\frac{d\sigma}{d\Omega} \propto 1/\sin^4(\theta/2)$, hence the vast majority of these collisions result in a small angular deflection of the particle (multiple Coulomb scattering), causing a random zigzag path through the medium. The cumulative effect of those small angles scattering is, however, a net deflection from the original particle direction. Such deflection can cause dechanneling of the particle (see Sections 1.1.4 and 1.1.5)

In the limit of high particle momenta the motion of particles in the channeling case (a series of correlated collisions) may be considered in the framework of classical mechanics, even though the single process of scattering is a quantum event . The classical approximation works better at high energy for two reasons: the first is that the wave lengths of incoming particles are sufficiently small to prevent the formation of interference patterns of waves; secondly classical mechanics is applicable thanks to the large number of energetic levels accessible in the interplanar potential (in analogy with the quantum harmonic oscillator). The second condition is always fulfilled for heavy particles, such as ions and protons, but for light particles (electrons, positrons) the classical approach starts to work in the $10 - 100MeV$ range.

Now we can rewrite the law of conservation of the total energy of the system in the classical approximation and in the law-angle approximation. Let us consider the motion of a particle in the continuous potential. Let us consider the classical equation of motion of a particle with energy:

$$\sqrt{p^2 + m^2} \tag{1.14}$$

When the transverse component p_x is much smaller than the longitudinal component p_z, we may rewrite the law of conservation of the total energy:

$$E = \sqrt{p_x^2 + p_z^2 + m^2} + U(x) = const \tag{1.15}$$

as

$$\frac{p_x^2}{2E_z} + U(x) + E_z = const \tag{1.16}$$

with $E_z = \sqrt{p_z^2 + m^2}$.

For motion in the potential $U(x)$ the longitudinal component of the momentum is conserved, implying the conservation of the transverse energy:

$$E_T = \frac{p_x^2}{2E_z} + U(x) \tag{1.17}$$

By defining $p_x = p_z\theta$ and assuming $E_z \approx E$, $p_z \approx p$, using the known relation $p = \beta E$, where β is the particle velocity, we may rewrite E_T as:

$$E_T = \frac{p\beta}{2}\theta^2 + U(x) = const \tag{1.18}$$

Rewriting Eq. 1.18 taking into account that $\theta = dx/dz$ one obtain

$$E_T = \frac{p\beta}{2}\left(\frac{dx}{dz}\right)^2 + U(x) = const \tag{1.19}$$

Differentiating with respect to z and dividing all terms by θ, the result for the one-dimensional transverse motion in the potential $U(x)$ is:

$$p\beta\frac{d^2x}{dz^2} + \frac{d}{dx}U(x) = 0 \tag{1.20}$$

Eq. 1.20 describes the particle transverse oscillation of the motion in the potential well under channeling condition. The particle trajectory for an arbitrary $U(x)$ may be obtained by integration of the expression

$$dz = \frac{dx}{\sqrt{\frac{2}{p\beta}[E_T - U(x)]}} \tag{1.21}$$

Differentiating the equation of the conservation of transverse energy with respect to z we obtain the equation which describes the particle motion in the potential well:

$$p\beta\frac{d^2x}{dz} + U'(x) = 0 \tag{1.22}$$

By adopting the harmonic potential approximation $U(x) \simeq U_0(2x/d_p)^2$, the solution of Eq. 1.20 is a sinusoidal oscillation:

$$x = \frac{d_p}{2}\sqrt{\frac{E_T}{U_0}}\sin\left(\frac{2\pi z}{\lambda} + \phi\right) \tag{1.23}$$

with $\lambda = \pi d_p\sqrt{p\beta/2U_0}$ being the oscillation length.

The particle remains trapped within the channel if its transverse energy E_T is less than the potential-well depth U_0:

$$E_T = \frac{p\beta}{2}\theta^2 + U(x) \leq U_0 \tag{1.24}$$

where U_0 is the maximum value of the potential barrier at the distance $d_p/2$ from the center of the potential well, where the plane is located.

Suppose a particle moves along the center line of a channel ($x = 0$), with oscillations about the center of the channel, from eq. 1.24 the limiting angle of capture is obtained:

$$\theta_L = \sqrt{\frac{2U_0}{p\beta}} \tag{1.25}$$

where θ_L is the critical angle introduced by Lindhard, both for planar and axial channeling. When the incident angle of a particle with the channel direction is less than θ_L but close to the nuclei (as close as $\sim a_{TF}$), the scattering from the nuclei itself rapidly removes the particle from the channeling mode (sec. 1.1.5). For this reason it can be introduced the critical transverse coordinate for planar channeling of long crystals

$$x_c = \frac{d_p}{2} - a_{TF} \tag{1.26}$$

and an other common definition of the critical angle of channeling

$$\theta_c = \sqrt{\frac{2E_c}{p\beta}} \tag{1.27}$$

where $E_c = U(x_c)$ is the critical transverse energy. If a particle moves along the center line of a channel and has an incident angle with the channel direction less then θ_c we can

neglect its escape from the channel and hence proper channeling takes place.

The calculations seen above with the harmonic approximation are valid in the case of motion of positively charged particles channeled between two crystallographic planes. For negative particles the planar potential is attractive and then, in the case of motion in channeling condition, the particles oscillate around the atomic planes (or axis) and not between them, crossing the dense layers of atomic nuclei. Therefore the probability of scattering with nuclei increase, hence increasing the probability that the particle escapes from the channel. For this reason the dechanneling lengths (see section 1.1.5) for negative particles are much shorter than for positive ones. Fig. 1.4 shows the continuous planar potential for negative particles in the case of a silicon crystal oriented along the (110) planes; we can notice that U_{pl} is opposite to the one for positive particles. Nevertheless the depth U_0 does not change so $\theta_L = \sqrt{\frac{2U_0}{pv}}$ is the same for both positive and negative particles (see Section 1.1.5).

1.1.4 Dechanneling in long crystals

The motion of channeled particles is affected by incoherent scattering processes with electrons and nuclei (as well as from the crystal lattice defects), that cause the non-conservation of the transverse energy E_T due to the contribution of the random angle in a single event of scattering. As a result E_T may be higher than the potential barrier and in this case the particle comes out from the channel, i.e.,dechanneling process). In the depth of a crystal, as well as the particles leaving the channeling mode, there may be particles entering the channeling mode, i.e., feeding in. The mechanisms responsible for these two opposite processes are essentially the same.

There are two main sources of dechanneling in crystals: the multiple quasi-elastic scattering with nuclei and the multiple inelastic scattering with electrons. For positive particles interacting with long crystals, the fraction of particles impinging on nuclei are rapidly dechanneled. In fact, Particles captured in the potential-well with $E_T > E_c$ leave quickly the channeling mode owing to the multiple Coulomb scattering with nuclei. Thus, the most frequent collisions of the remained channeled particles are soft. Therefore, one can treat the scattering during motion in channeling with the formalism of a diffusion theory.

In the depth z of a long crystal the fraction of channeled particles decrease exponentially

$$N_{ch}(z) \approx N_s e^{-z/L_e} \tag{1.28}$$

where N_s is the number of particles in stable channeling state at the crystal entry face

($z = 0$), N_{ch} is the number of channeled particle, L_e is the electronic dechanneling length, which scales with the particle momentum [65]. If a channeled particle has a transverse energy $E_T \leq E_c$ (far from nuclei), it is affected by multiple scattering with electrons. Because the electronic density is rather uniform in the channel, being due to valence electrons, the process is independent from the transverse position x of the particle but only depends on E_T. This process is slower than the one due to the strong nuclear collisions and using the Fokker-Plank equation [57]. The electronic dechanneling length for positive particles has been extensively measured in experiments [14, 66, 67].

The non-conservation of transverse energy E_T for soft interactions in long crystals can be treated though the diffusion theory. The E_T evolution can be considered as a random-walk process with a positive or negative variation of ΔE_T at each single event

$$\Delta E_T = p\beta\theta\theta_s + \frac{p\beta}{2}\theta_s^2 \tag{1.29}$$

where θ_s is the single scattering in the event.

Experiments have proved that the oscillation period for a channeled particle is typically small compared to the length crossed before dechanneling takes place [14, 66, 67]. Thus, all the functions can be averaged over one oscillation period. By denoting $w(E_T.q)dz$ the probability that the E_T changes of a fraction q over a length dz, the variation of the distribution function of particles $f(E_T)$ holds

$$\frac{\partial f(E_T)}{\partial z} = \int [f(E_T - q)w(E_T - q, q) - f(E_T)w(E_T, q)]dq \tag{1.30}$$

By assuming that the variation at each event is small and by expanding the above terms in series, Eq. 1.30 becomes a Fokker-Planck equation

$$\begin{aligned} \frac{\partial f(E_T)}{\partial z} &= -\frac{\partial}{\partial E_T}\left[f(E_T)\int qw(E_T, q)dq\right] + \frac{1}{2}\frac{\partial^2}{\partial E_T^2}\left[f(E_T)\int q^2 w(E_T, q)dq\right] & (1.31)\\ &= -\frac{\partial}{\partial E_T}[f(E_T)A] + \frac{1}{2}\frac{\partial^2}{\partial E_T^2}[f(E_T)D] & (1.32) \end{aligned}$$

where A is the friction factor and D the diffusion coefficient. The friction factor and the diffusion coefficient are connected through [68]

$$A(E_T) = \frac{1}{2}\frac{\partial}{\partial E_T}D(E_T) \tag{1.33}$$

Thus, the Fokker-Planck equation (Eq. 1.32) becomes

$$\frac{\partial f(E_T)}{\partial z} = \frac{1}{2}\frac{\partial}{\partial E_T}\left[D(E_T)\frac{\partial f}{\partial E_T}\right] \tag{1.34}$$

Calculations of $D(E_T)$ for semiconductors have shown that a linear approximation $D(E_T) \sim D_0 E_T$ is still valid until the distance from nuclei is $> a_{TF}$. By solving Eq. 1.34 as a series of Bessel functions and by approximating the solution at the first order [57], in the depth of a crystal the fraction of channeled particles decreases exponentially with the electronic dechanneling length L_e.

$$\frac{N_{ch}}{N_0} \sim \exp^{-z/L_e} \tag{1.35}$$

By applying several approximation and by comparing with experimental data L_e holds [57]

$$L_e = \frac{256}{9\pi^2}\frac{p\beta}{\ln(2m_e\gamma/I) - 1}\frac{a_{TF}d_p}{Z_2 r_e m_e} \tag{1.36}$$

where m_e and r_e are the mass and the classical radius of an electron, I is the mean ionization energy and γ is the Lorentz factor.

1.1.5 Dechanneling in short crystals

Channeling of positively charged particle has been extensively studied over a wide energy range and finds many applications at both low [69] and high energies [57]. Conversely, experimental knowledge about channeling of negative particles had been limited due to the lack of high-energy non-radiating beams of negatively charged particles and experimental difficulties to fabricate suitable crystals.

Pioneering experiments at CERN have failed to detect channeling of high-energy negative particles, while under the same conditions it was clearly observed channeling of their positive counterparts [66, 70, 71]. Only recent experiments demonstrated the possibility to steer also negatively charged particle beams through bent crystals at the full bending angle [44, 45, 47]. In fact, due to incoherent interaction with the atoms, negative channeled particles suffer much stronger dechanneling [43, 57] with respect to their positive counterpart, i.e., the number of particles leaving the channeling state per unit length is higher for negative particles than for the positive ones.

Nevertheless, channeling of negative particle may be a useful tool for beam manipulation [18, 46, 72], for production of high-energy radiation in both unbent [63] and bent [42, 48] crystals, in crystalline undulators [73–75], and as a positron source [76, 77]. Further

development of such applications does require a deeper knowledge of incoherent interactions between channeled particles and crystals [78], which would lead to design crystals with optimized geometrical parameters.

In order to clarify the difference between the motion of planar-channeled positive and negative particles and their dechanneling mechanisms, we show in Fig. 1.4 the averaged potential (calculated as in Ref. [79]) experienced by the particles channeled between (110) silicon planes. Averaged potential is characterized by a well, whose minimum is located in the middle of neighboring atomic planes for positive particles and on the atomic planes for negative ones.

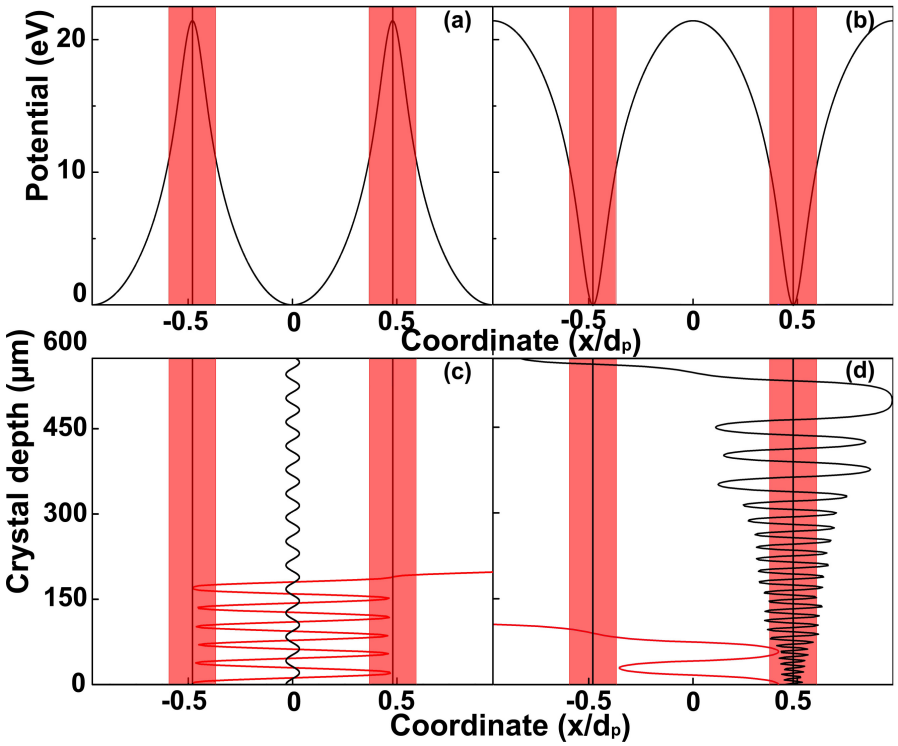

Figure 1.4: (a-b) planar potentials experienced by π^+ and π^- channeled between (110) silicon planes. Shaded regions highlight the regions of high nuclear density (nuclear corridors), vertical lines inside those regions show the positions of atomic planes. (c) Trajectories of two 150 GeV/c π^+: the trajectory of the particle with larger oscillation amplitude is for a particle whose impact parameter lays inside the region of high nuclear density (i.e. the particle is in unstable channeling state). Such a particle is dechanneled after traversing a short distance in the crystal. The other trajectory refers to a particle impinging far from atomic planes (such particle is in stable channeling states). (d) trajectories of two 150 GeV/c π^-: all negative particles pass through the high-atomic density regions and are subject to nuclear dechanneling.

For positively charged particles, the mechanism of dechanneling is well established [30, 43, 57, 80]. It occurs because of multiple scattering experienced by particles inside the channels with nuclei and electrons [33, 81–83]. Two mechanisms have been identified, i.e., nuclear and electronic dechannelings. Particles impinging close to the atomic planes (see Fig. 1.4) are found in unstable channeling states and are dechanneled by nuclei traversing a short distance in the crystal (nuclear dechanneling). On the other hand, particles impinging onto the crystal far from the atomic planes (see Fig. 1.4) are found in stable channeling states. If no interaction with electrons would occur, such particles will never be dechanneled. Indeed, particles slowly increase their transverse energy via interaction with the electrons until they reach the region with high-atomic density and then experience interaction with the nuclei (electronic dechanneling). With the aim to estimate the fraction of positive particles suffering nuclear dechanneling, we approximate the atomic density as a Gaussian distribution with standard deviation equal to the atomic thermal vibration amplitude, u_t, which is 0.075 Å for Si at 273 K [57]. By assuming that the atomic density region interested by intense multiple scattering extends over 2.5σ [43] - the so-called nuclear corridor - (see Fig. 1.4) and bearing in mind that (110) interplanar distance is $d_p = 1.92$ Å, about 19.5% of particles ($5u_t/d_p \approx 0.195$) of a perfectly parallel beam are under unstable channeling state. The strengths of dechanneling by electrons and nuclei are quite different. As an example, for 400 GeV/c protons interacting with Si (111) planes, $L_e \sim 220$ mm [63], while $L_n \sim 1.5$ mm [43], L_e and L_n being the electronic and nuclear dechanneling lengths, respectively. Dechanneled particles are found in over-barrier states and the probability to be rechanneled is negligible for a bent crystal. Dechanneling processes lead to a decay in the number of channeled particles, which can be approximated by exponential functions (e.g. [43]). The number of channeled particles at coordinate z, $N_{ch}(z)$, over the total number of particles, N_0, holds [43]

$$N_{ch}(z) \approx N_u e^{-z/L_n} + N_s e^{-z/L_e} \tag{1.37}$$

where N_u and N_s are the number of particles in unstable and stable channeling states at the crystal entry face ($z = 0$), respectively. For Si (110) at 273 K, $N_u \sim 19.5\% N_0$ and $N_s \sim 80.5\% N_0$.

For negatively charged particles, since the minimum of the potential well is located on the atomic planes, all the particles are readily directed toward the nuclear corridor. As a consequence, all negatively charged particles lie in unstable channeling states ($N_s = 0$, $N_u = N_0$) and the mechanism of dechanneling via interaction with valence electrons negligibly contributes to dechanneling with respect to nuclear dechanneling. Therefore,

the number of channeled particles holds

$$N_{ch}(z) \approx N_0 e^{-z/L_n} \tag{1.38}$$

1.2 Models for deflection efficiency of planar channeling

Two models have been worked out to describe channeling efficiency in thin bent crystals in this thesis. The first model is based on statistical and geometrical considerations (analytical), the second on the solution of the equation of motion with simplified surrounding conditions (semi-analytical). If we compare to DYNECHARM++, the computational time changes by orders of magnitudes between such models and the Monte Carlo simulations. Therefore, they can be useful depending on the purpose for which an evaluation of channeling efficiency is made.

1.2.1 Analytical

The first model has been developed extending the approach developed for thick crystals in Refs. [57, 84]. By considering a parallel beam of protons interacting with a thick straight crystal, particles undergoing nuclear dechanneling (N_n) are immediately dechanneled and efficiency falls off. The remaining fraction of the channeled particles are subject to electronic dechanneling, which can be described by diffusion theory [57] and approximated through an exponential decay function with decay length equal to L_e. For slightly bent crystals the harmonic approximation well describes the interplanar potential far from atomic planes. The width of the potential well is reduced by a quantity proportional to the decrease in the width of the well. In addition, the electronic dechanneling length scales as a function of R, because particle trajectories closely approach atomic nuclei in a bent crystal (see Fig. 1.5). Under harmonic approximation the scaling factor is $(1-R_c/R)^2$ [57], which is equal to the lowering of the potential well depth. From previous considerations, channeling efficiency in thick bent crystals ϵ_L holds

$$\epsilon_l(R, L) = \frac{N_{tot} - N_n}{N_{tot}} (1 - R_c/R)^2 e^{-\frac{L}{(1-R_c/R)^2 L_e}} \tag{1.39}$$

where L is the crystal length along the beam direction, N_n is the number of particles which can be subject to nuclear dechanneling and N_{tot} is the total number of particles interacting with the crystal.

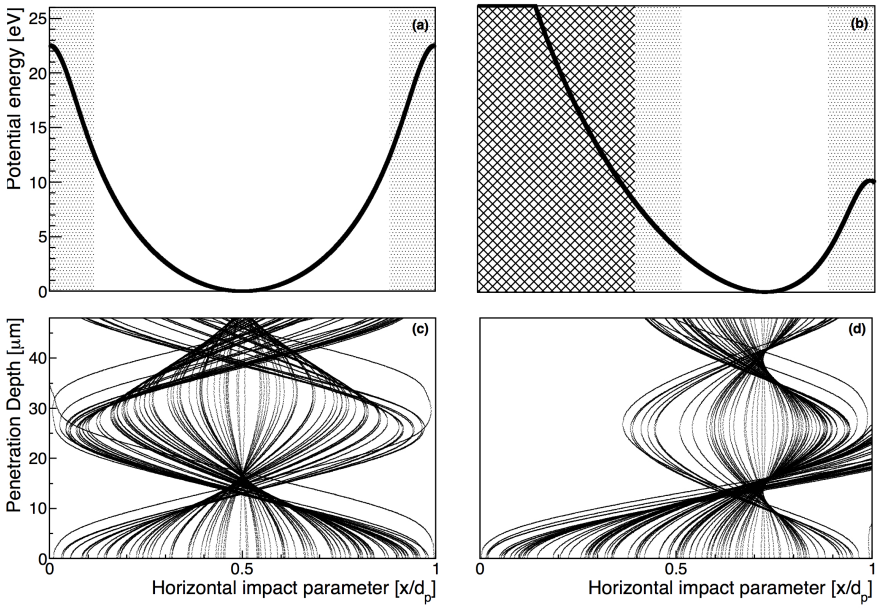

Figure 1.5: (a)-(b) Potential energy in the reference frame integral to crystal planes for $R = \infty$ (a) and $R = 3R_c$ evaluated through the ECHARM software [79]. (b). Gray boxes highlight impact region which will cause particle to dechannel due to multiple scattering on nuclei and core electrons. Crossed box region is the impact region of particle with do not channel because of the presence of the crystal curvature. (c)-(d) Trajectories of 400 GeV/c proton interacting with a Si crystal with bending radius $R = \infty$ (c) and $R = 3R_c$ (d).

For a thin bent crystal, the same approximation can be adopted through mild modifications. Since the crystal thickness is so thin to be comparable to nuclear dechanneling length, not all the N_n particles have abandoned the channeling state at the crystal exit. Therefore, Eq. 1.39 for deflection efficiency has to be modified to include the possible contribution of the fraction of particles that close-encounter nuclei at the entrance of the crystal. As a result, the channeling efficiency for thin bent crystal $\epsilon_s(R, L)$ holds [51]

$$\epsilon_s(R, L) = \frac{N_n}{N_{tot}} e^{-\frac{L}{L_n}} + \epsilon_l(R, L) \tag{1.40}$$

1.2.2 Semi-analytical

Instead of a simple geometric model, a more detailed description of the dechanneling process can be achieved by studying the dechanneling probability as a function of the intensity of interaction for particle at given impact parameter. Scatterings with electrons and nuclei

does not significantly alter the trajectory of a channeled ultra-relativistic particle. Such approximation can be adopted to treat the crystals with length considerably longer than one oscillation period λ, i.e., for the overwhelming majority of practical cases. In the model, the transverse energy variation is computed only after one oscillation period. Such energy variation depends on the intensity of interaction of channeled particles with nuclei and electrons, which is in turn a function of the average quantity of matter $\overline{\rho}$ encountered by a channeled particle during its motion. Since no interaction is considered during particle motion within one oscillation, the particle trajectory is a function only of the initial transverse energy $E_{T,0}$, which is related to the impact parameter x_0 and the incoming angle θ_0.

$$E_{T,0} = \frac{pv}{2}\theta_0^2 + U(x_0) \tag{1.41}$$

and is evaluated through the integration of the relativistic equation of motion

$$x(z) = \frac{1}{\lambda}\int_{\lambda}\sqrt{\frac{2}{pv}\left[E_{T,0} - U(x)\right]}\mathrm{d}z \tag{1.42}$$

x being the particle position in the coordinate orthogonal to crystal planes, z the direction along the particle motion, p and v the particle momentum and velocity, $U(x)$ the interplanar potential. Examples of integration are shown in Fig. 1.5 (c). The nuclear density averaged over one period $\overline{\rho}(x_0)$ holds

$$\overline{\rho}_n(x_0) = \frac{1}{\lambda}\int_{\lambda}\rho_n(x(z))\mathrm{d}z \tag{1.43}$$

where $\rho_n(x)$ is the distribution of nuclear density averaged over planes or axes. Considering the electronic density $\rho_e(x)$, the same equation keeps true for the electron density averaged over planes or axes, $\overline{\rho}_e(x_0)$. The probability of dechanneling is equivalent to the probability to receive enough transverse energy to be kicked out of the potential well. Transverse energy can be acquired through multiple scattering with nuclei or loss of energy by collisions with electrons. Indeed any variation of the total energy modifies particle direction with respect to the orientation of crystal plane. Consequently, the kinetic transverse energy may vary. Therefore, the probability to be dechanneled holds

$$\frac{\mathrm{d}P(x_0)}{\mathrm{d}x_0} = \frac{1}{d_p}\int_{\Delta E_x(x_0)}^{+\infty}\frac{\mathrm{d}P_{E_x}(\overline{\rho})}{\mathrm{d}E_x}\mathrm{d}E_x \tag{1.44}$$

where $\mathrm{d}P_{E_x}(\overline{\rho})/\mathrm{d}E_x$ is the distribution function of energy acquired by the particle after one oscillation and $\Delta E_x(x_0)$ is the energy to overcome the potential well, i.e., for

dechanneling. As the crystal is bent, the equations for the particle's trajectory and for the transverse energy variation needed for dechanneling have to be changed to take into account the lowering of the potential barrier. In particular, Eq. 1.41 changes to

$$E_{T,0} = \frac{pv}{2}\theta_0^2 + U(x_0) + \frac{pvx_0}{R} \tag{1.45}$$

As a result, Eq. 1.42 becomes

$$x(z) = \frac{1}{\lambda}\int_{\lambda}\sqrt{\frac{2}{pv}\left[E_{T,0} - U(x) - \frac{pvx}{R}\right]}\mathrm{d}z \tag{1.46}$$

Eq. 1.46 is quite general being valid for any shape of the potential $U(x)$. Then, Eqs. 1.43 and 1.44 can be repeated for calculation of dechanneling probability. Examples of integration with Molière potential are shown in Fig. 1.5.d. The calculation of the averaged potential, electron density and nuclear densities of the crystal have been worked out though the ECHARM software [79], which allows to evaluating the averaged electrical characteristics of a complex atomic structure and to choose between various models for the form factor of the electron density. Then, the trajectory's equation is numerically solved. The efficiency is computed as the fraction of particles which reach the crystal end without dechanneling.

1.3 Coherent Interactions in Bent Crystals

1.3.1 Particle Motion in Bent Crystals

The possibility of steering beam with a slightly bent monocrystal was proposed by Tsyganov in 1976 [1, 2]. He expected that the channeled particles would follow the direction of the bent atomic planes (or axes), thus deviating from the initial direction by an angle equal to the one of the crystal bend.

Now we introduce a brief description of the motion of a positive particle within a bent planar channel. If the crystal has a macroscopic curvature radius (of the order of several meters), it has no effect on the potential of the crystal lattice in the range of angstroms in the laboratory inertial frame. Instead, from the point of view of non-inertial reference frame (comoving with a particle channeled with zero transverse momentum along the bent planar channel) a centrifugal fictitious force appears due to the bending of the crystal. In Fig. 1.6 is shown a scheme for this two reference frame: Fig. 1.6.a) represents the motion of a channeled particle in the laboratory; Fig. 1.6.b) describes the motion in the

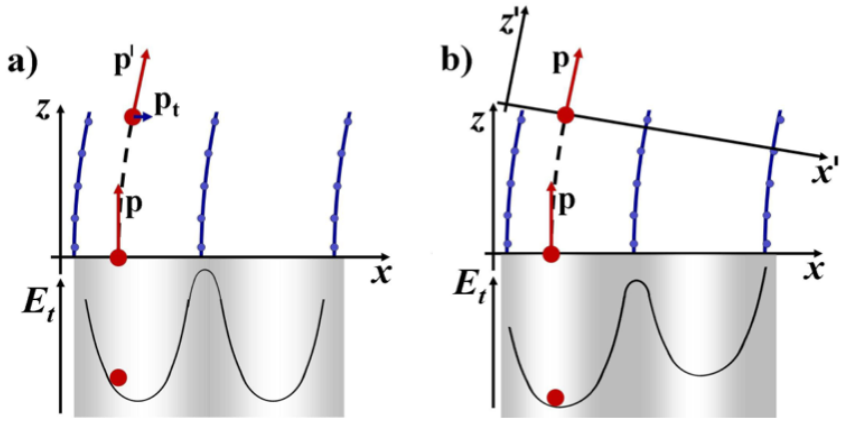

Figure 1.6: Scheme of the channeling motion of a positive particle particle that enter in the channel aligned with respect to the crystal planes: a) in the laboratory inertial frame; b) in the non inertial comoving reference system which rotates with the particle; the centrifugal force appear

non-inertial comoving reference frame.

In case a) the particle enters in the channel aligned with respect to the crystal planes, with $p_t = 0$, but in order to follow the channel bending in the evolution of motion, the particle acquires a non-zero transverse momentum; so the interplanar continuous potential exerts a force on it which modifies the particle momentum. Instead in case b) the particle momentum direction does not change, but a centrifugal force directed towards the external side of the channel appears.

In this comoving frame, the equation of motion 1.20 for a channeled particle becomes:

$$p\beta\frac{d^2x}{dz^2} + U'(x) + \frac{p\beta}{R(z)} = 0 \tag{1.47}$$

where x, z are the particles coordinates in this frame and $1/R(z)$ is the local curvature of the channel. If the bending radius R is independent of z, the particle moves as if it was in an effective interplanar potential of the form:

$$U_{eff}(x) = U(x) + \frac{p\beta}{R}x \tag{1.48}$$

with a transverse energy $E_T = \frac{p\beta}{2}\theta^2 + U_{eff}(x)$.

In Fig. 1.7 there are some examples of the potential $U_{eff}(x)$ for different ratios $p\beta/R$ in comparison with the undisturbed potential $U(x)$ for the Si planes (110).

We can notice that as the ratio pv/R increases, the depth of the effective potential well

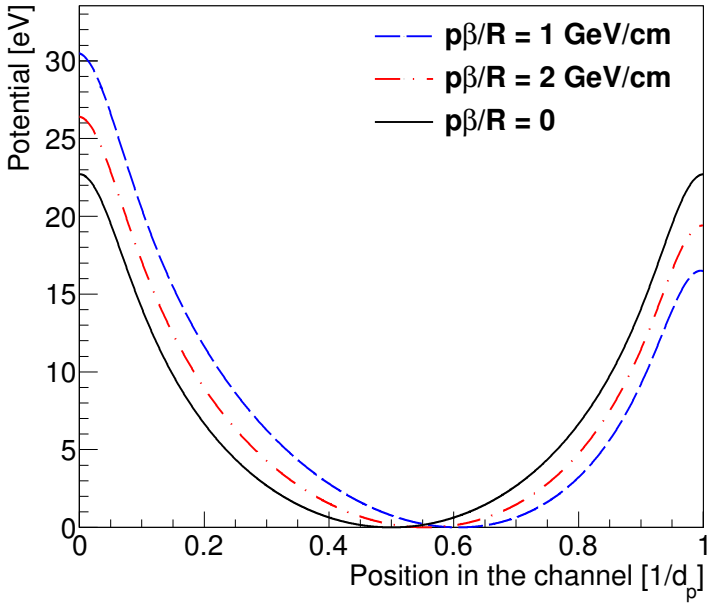

Figure 1.7: The interplanar potential in Moliére approximation for Si (110) (solid line) and the effective potential for pv/R of 1 GeV/cm (dashed line) and 2 GeV/cm (dot-dashed line).

decreases and its minimum value is shifted towards the atomic plane; thus at some critical $(pv/R)_c$ the well disappears and channeling is no longer possible. The critical bending curvature is defined by the maximal interplanar electric field ε_{max} near the atomic plane.It is possible to define a critical radius R_c:

$$R_c = \frac{p\beta}{e\varepsilon_{max}} \tag{1.49}$$

According to Biryukov we should use $U'(x_c)$ instead of $e\varepsilon_{max}$ and so redefine R_c

$$R_c = \frac{p\beta}{U'(x_c)} \tag{1.50}$$

Moreover the critical energy in the case of bent crystal is $E_c(R_c/R) = E_{c,0}(1 - R_c/R)^2$, where E_c is the critical transverse energy in the straight crystal. In this way, it is possible to define a new critical angle $\theta_c(R_c/R)$ for bent crystals:

$$\theta_c(R_c/R) = \theta_{c,0}\,(1 - R_c/R) \tag{1.51}$$

where $\theta_{c,0} = \sqrt{2U_c/(p\beta)}$ is the critical angle of channeling for a straight crystal. From Eq. 1.51 we can notice that θ_c is reduced from a factor $(1 - R_c/R)$ with respect to straight crystals.

1.3.2 Quasichanneling

If a particle moves in the crystal volume with a transverse energy grater than the critical one but at small angle (nearly aligned) to the atomic planes ($\theta > \theta_c$), it is influenced by the continuous potential and has special features in a bent crystal: this type of particles are called quasichanneled particles or above-barrier particles [85–87].

For quasichanneled particles two different effects have been discovered, the volume capture (VC) [88] and the volume reflection (VR) [3]. In Fig. 1.8 the different effects due to influence of the continuous planar potential, in case of straight and bent crystal, are schematically shown. Fig. 1.8(a)-(c) represents a schematic depiction of motion for an unchanneled particle and a channeled one in a straight crystal in the plane (x, E_T) (a) and in the plane (x, z), (c); instead in Fig. 1.8(b)-(d) the motion of positive particles in channeling, VR and VC conditions is shown in the planes (x, E_T) and (x, z). In next paragraphs this two effects will be described in more detail.

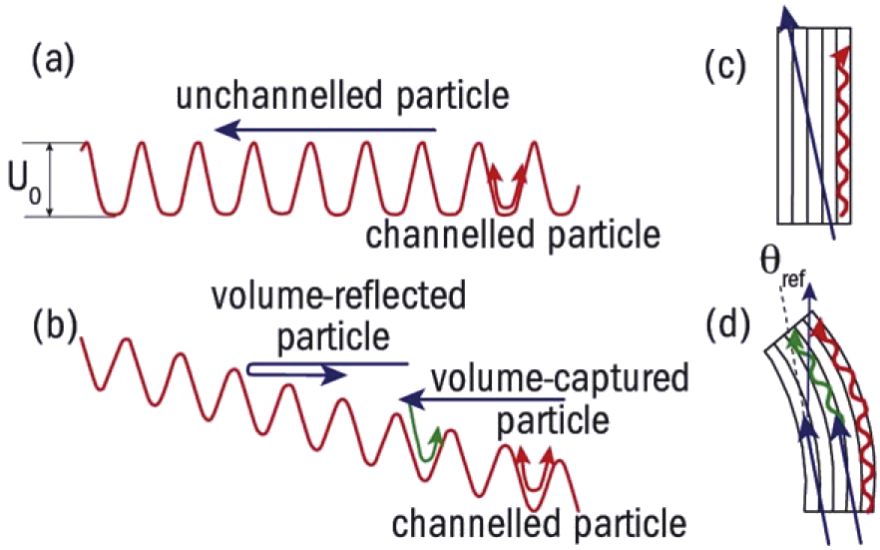

Figure 1.8: (a)-(c) Channeled and unchanneled particle in a straight crystal; (b)-(d) particle in channeling, VR and VC conditions in a bent crystal [37].

Volume Capture

In sections 1.1.4 and 1.1.5 the dechanneling mechanism was described and it was anticipated that as the particles leaves the channel, there may be particles entering in the channeling mode: this process, called feeding in, is due to the well-known fact that for any trajectory of a particle in a crystal a time-reversed trajectory is possible. In straight

crystals all these two effects are due to scattering processes: the first one is the transition of a particle from the channeled beam to the random one ('over barrier'), instead the second describes the opposite transition where a random particle could be captured into a channeled state. According to Lindhard's reversibility rule [30], the probability of this two opposite transitions is the same.

Volume capture is the feed-in process of channeling in bent crystal [59, 89]. The above paragraph pointed out that when a beam passes through a bent crystal, a large part of the beam is reflected in the region of tangency with the bent planes. This is not the only one type of motion possible for quasichanneled particles; some particles of the beam may be captured in planar channeling conditions because in this region VC becomes possible for any unchanneled particle. As a result VC in bent crystals is more efficient than the feeding-in mechanism in straight ones, so we expect that the feed-out mechanism increases according to the reversibility rule. In fact the dechanneling probability increases because the potential well E_c and so the critical angle θ_c are decreased. Moreover we can notice that the probability for dechanneling (volume capture) depends strongly on the bending radius: it grows (decrease) when R decreases. Such effect takes place even without an account of incoherent scattering (without volume capture to planar channel). In addition with the increase of particle energy, this effect becomes more noticeable for both positive and negative particles (see Ref. [90]).

Volume Reflection

When a quasichanneled particle moves through a bent crystal in approximation of continuous planar potential is deflected on average in a direction opposite to the one of the crystal bending by an angle of order $\sim \theta_L = \sqrt{2U_0/pv}$ with a small spread. This means that in a bent crystal the mean exit angle of unchanneled particle is not equal to the mean incident angle.

In a bent crystal it can happen that, even if a particle is incident on crystal with an angle exceeding the critical one, its trajectory during the motion in the crystal's depth becomes tangential to the crystallographic planes (and so tangential to the planar potential), because of the curvature of the latter (see Fig. 1.9.b)). This condition it is possible for many trajectories in a broad angular range in the volume of the crystal and hence VR becomes possible (in the region of tangency) for any particle of the random beam. The angular acceptance is equal to the bending angle of the crystal (l/R, where l is the crystal length) because an incident particle will be able to be tangent to the curvature of the crystal in all this interval.

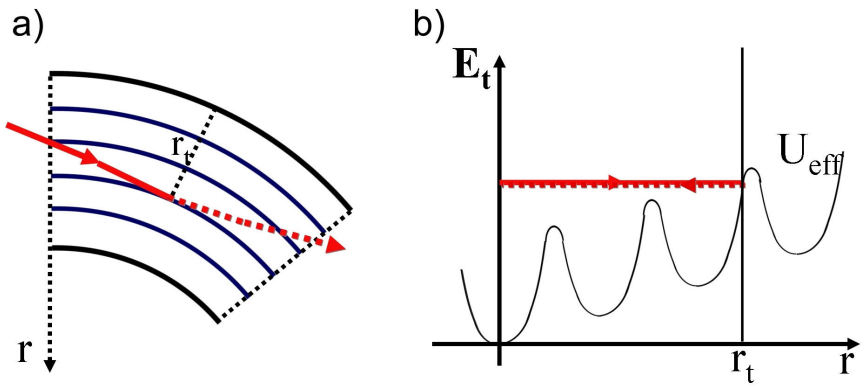

Figure 1.9: Reflection of a charged particle in the crystal volume at the rotating radial coordinate r_t: a) schematic depiction of volume reflection; b) phase space of the particle transversal energy as a function of the radial coordinate [42].

For a bend radius $R \gg R_c$, the volume reflection angle for positive particles is $\theta_{VR} \approx 2\theta_c$, while for negative particles is smaller, because of the shape of the effective interplanar potential [91]. The reflecting points for a negative particle (between the planes) are more flat and they accomplish a longer path near turning points than positive particles (see Fig. 1.4).

For smaller R, i.e., $R \gg R_c$ is no more valid, the deflection angle θ_{VR} is just below $2\theta_c$, because the increase of the crystal curvature allows the reflection to occur in points in which the interplanar potential is less intense (see Fig. 4.2). In this case the efficiency grows due to the increase of the reflective area.

VR has a greater angular acceptance with respect to planar channeling, but it has a smaller angular deflection ($\theta_{VR} \sim \theta_L$). In addition, VR efficiency increases with the decreasing of the bending angle, because the mechanism that generates the inefficiency is VC, whose probability increases when R grows. Moreover, since the volume capture probability scales as $E^{-2/3}$, VR efficiency increase with E. For all this reason volume reflection mechanism is of great interest in high energy physics applications, especially in steering beam.

1.3.3 Multi Volume Reflection in Multi-Crystals

Let us consider the process of volume reflection of particles in a bent crystal. The crystal orientation angle θ_0 and the deflection angles of particles θ_x are counted from the direction of the incident beam axis and the initial direction of the particle momentum, respectively. The direction to the crystal bend side is defined as a positive one. When the crystal

orientation angles $|\theta(r)| < \theta_c$ the beam particles can be captured into the channeling regime at the crystal entrance, where θ_c is the critical angle for channeling. VR of particles is realized when the orientation angles are in the interval $-\alpha < \theta_0 < -\theta_c$. The particles volume captured into the channeling regime near the tangency point can follow by the bent channels and be deflected by the angles up to $\alpha - |\theta_0|$.

By considering a positive particle beam interacting with a bent crystal, a VR deflection angle $\theta_{vr} = 1.4\theta_c$ μrad is obtained. The distribution has tail stretched to the bend side, which is produced by particles captured into the channeling regime in the tangency area. Some part of volume captured particles quickly leaves the channeling regime due to the same multiple scattering but others pass by the bent channels up to the crystal exit. The VR efficiency P_{vr} is the beam part shifting as a whole with the deflection angles $\theta_x < \theta_b = \theta_{vr} + 3\sigma_{vr}$, where θ_b is the boundary between the reflected beam and particles volume captured into the channeling states. The value of the volume captured beam part determines the VR inefficiency $\epsilon_{in,vr} = 1 - P_{vr}$.

The deflection angles of particles due to volume reflection are small. A possibility to increase the particle deflection angles using the sequence of a few short bent crystals working in the regime of VR has been studied recently [40, 46, 50]. The sequences of two and five quasi-mosaic crystals and the multi-strips joint by a single frame were used in these studies, respectively. It was shown that the beam deflection angles increase proportionally to the number of the sequence crystals.

The beam deflection efficiency by the crystal sequence should decrease with increasing the number of reflections because of the beam fractions volume captured into the channeling states in each of the crystals. The beam deflection efficiency due to multiple volume reflections (MVR) in N crystals can be estimated in the first order approximation of independent events as

$$P_{mr}(N) = P_{vr}^N = (1 - \epsilon_{vr,in})^N \approx 1 - N\epsilon_{vr,in} \tag{1.52}$$

However, the measured deflection efficiency is higher. Fig. 1.10 helps to understand the situation. The beam part marked 1, which was only considered for the estimate (1), makes two subsequent reflections with the mean angle θ_{vr} passing two bent crystals and obtains the mean deflection angle $2\theta_{vr}$. A smaller beam part 2 is volume captured in the first crystal but has a tangency point with the bent planes in the second crystal. Here many of the particles 2 are reflected obtaining the mean deflection angle θ_{vr}. So, particles volume captured in one of the sequence crystals also participate in the multiple volume reflection but they obtain a smaller deflection.

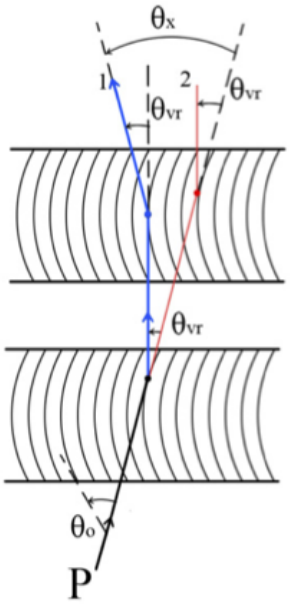

Figure 1.10: Schematic picture of the sequence of two bent crystals with the particle trajectories. 1 - a particle having volume reflections in both crystals near the tangency points with bent planes. 2 - a particle volume captured in the first crystal and then volume reflected in the second one (for a simplicity the trajectory part after VC is shown by red as a prolongation of the trajectory before VC). θ_0 is the crystal orientation angle, θ_x is the deflection angle of the particle 1, θ_{vr} is the VR deflection angle.

1.3.4 Multiple Volume Reflection in One Crystal

In this section it will be explain that it is possible to increase the VR deflection angle through a (MVROC). Experimental data has shown five-time increase in particle deflection versus the single VR one [92, 93].

Multiple reflection inside one crystal (MVROC) may occur under near-axis alignment of the crystal with the particle beam. When a particle trajectory becomes tangential to a bent crystalline plane, VR occurs. Such effect was mainly studied as reflection from individual lying of crystalline planes normal to the bending plane. It is possible to see a crystalline axis as the intersection of various crystal planes (see Fig. 1.11), thus single volume reflection from most of them may arise as a particle moves at a small angle with respect to such an axis. As a result, the deflection of each reflection sums up leading to significant increase in the total deflection angle with respect the standard VR.

In order to clarify the importance of VR by skew planes, the reference frame rYz can be used (see Fig. 1.12.a)). Such reference frame is comoving with a particle channeled with zero transverse momentum along bent crystal axes,

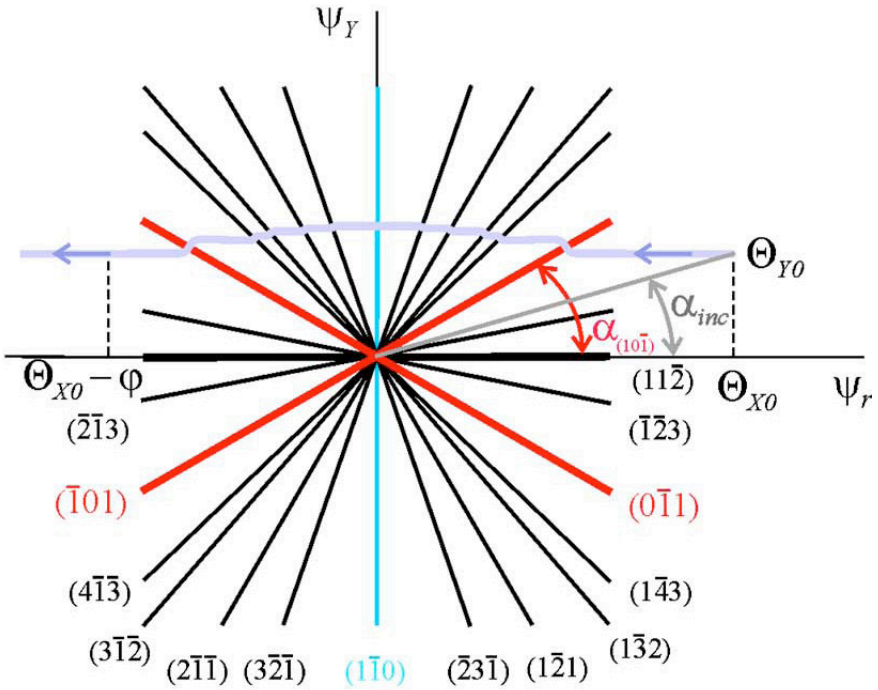

Figure 1.11: Projections of the plane in the plane (rY) or (ψ_r, ψ_Y) in the rotating reference frame. $\alpha_{(10-1)}$ is angle of inclination for the strong plane (10-1) and α_{inc} is the incident angle of the particle in this plane.

Initial values of the angles ψ_r and ψ_Y are equal to the particle incidence horizontal (Θ_{X_0}) and vertical (Θ_{Y_0}) angles, with respect to the crystal axis at the entry face of the crystal. In this comoving frame it is possible to see that ψ_r decreases with z because of the crystal bending. Therefore, the particle during its motion becomes subsequently parallel to the different planes intersecting along the axis (see Fig. 1.13). All interactions of the particle with one plane is accompanied by VR to the direction perpendicular to the plane at the tangency point and opposite to the crystal bending axis. The reflection from skew planes gives deflection in both horizontal and vertical directions, unlike the vertical plane which gives deflection in vertical direction only.

If a skew plane has an inclination angle α_{pl} with respect to the the horizontal plane (see Fig. 1.13), the deflection angles are $\theta_X = -\theta_{VR}\sin\alpha_{pl}$ and $\theta_Y = \theta_{VR}\cos\alpha_{pl}$, where θ_{VR} is the deflection angle for a single VR from a plane with with bending radius $R/\sin\alpha_{pl}$. Since $\sin\alpha_{pl} > 0$ for any $0 < \alpha < \pi$ meanwhile $\cos(\pi - \alpha) = -\cos\alpha$ we expect that the horizontal deflection angles θ_X sum up providing a deflection to the same direction and the vertical deflections angles θ_Y mutually compensate each other if the particle crosses all

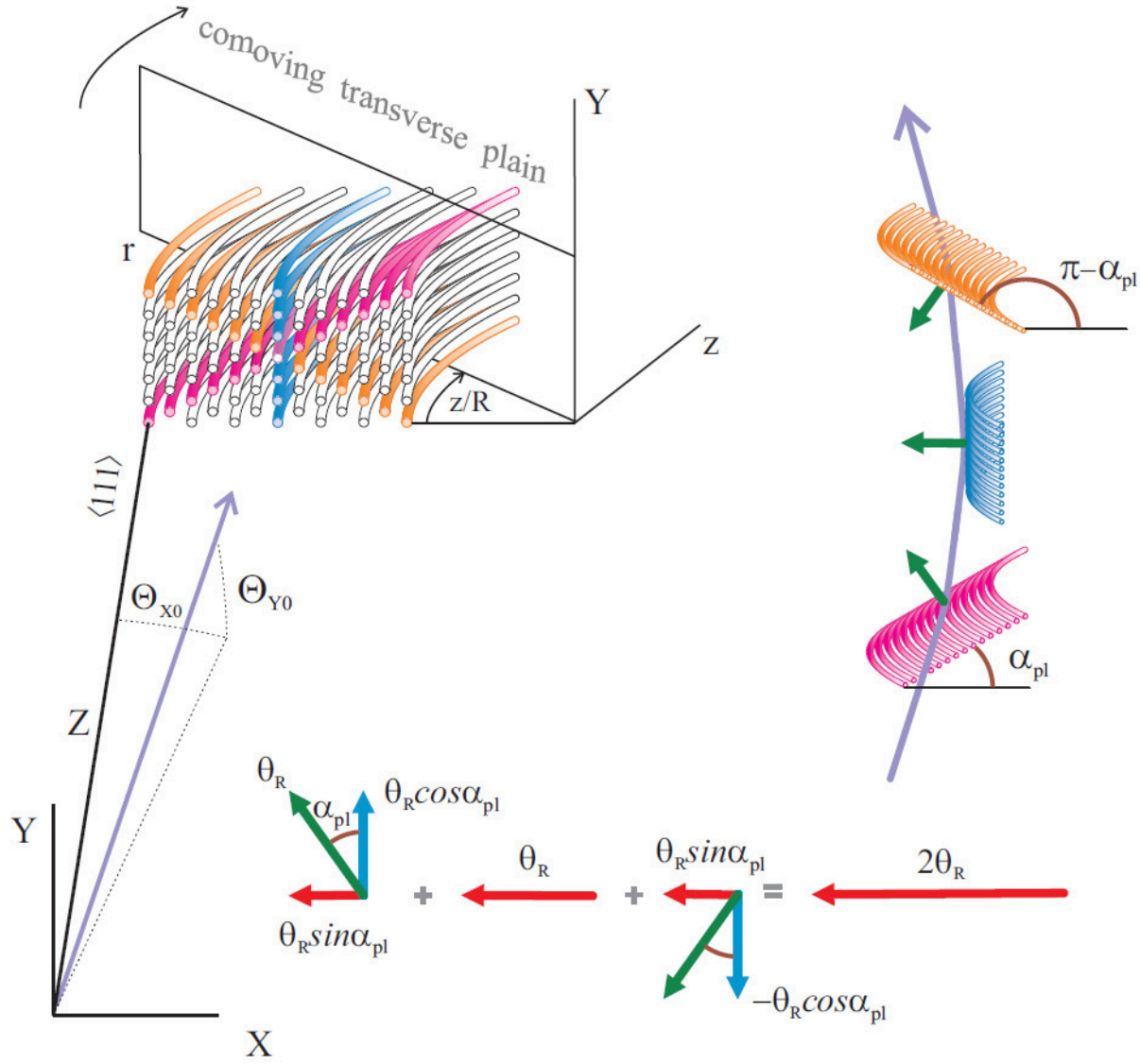

Figure 1.12: Particles which hit a crystal at small angles Θ_{X_0},Θ_{Y_0} with respect to crystal <111> axes experience VR from both the vertical plane, (1-10) and skew planes. Comoving reference frame rYz turns with the bent axis direction when a particle moves through the crystal.

symmetric skew planes during its motion. Thus if the horizontal incidence angle and the crystal bending angle $\phi = l/R$ satisfy the condition

$$\Theta_{X_0} = \frac{\phi}{2} \tag{1.53}$$

all skew planes will be involved in the VR process by symmetrical pairs, resulting in a

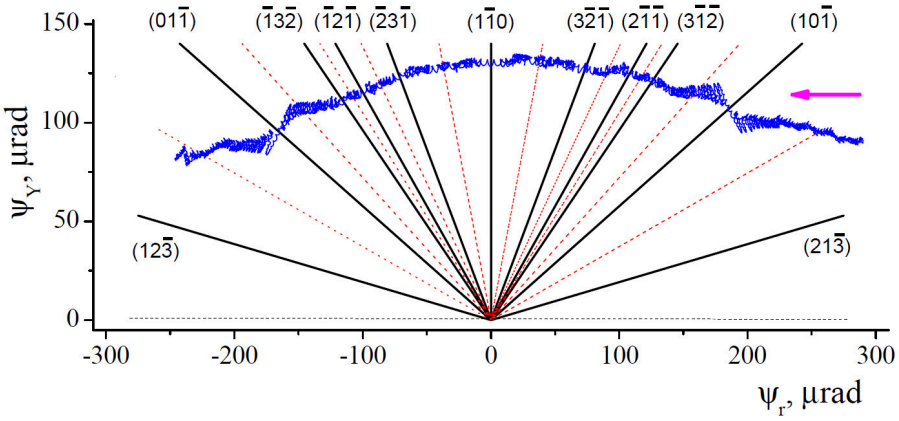

Figure 1.13: Particle trajectory in the plane (ψ_r, ψ_Y). Solid lines are the planes projections and dotted lines are the regions of influence of the planes.

complete compensation in the vertical deflection ($\psi_Y \approx \Theta_{Y_0}$).

In order to increase as much as possible the deflection angle with respect to the case of single VR, it is important to involved the strongest (110) skew planes. From Fig. 1.11 it is simple to notice that if the inclination of the strong skew plane (10-1) is α_{pl}, the entry angles (Θ_{X_0}, Θ_{Y_0}) at the crystal with respect to the axis <111> have to respect:

$$\arctan \frac{\Theta_{Y_0}}{\Theta_{X_0}} < \alpha_{pl} \tag{1.54}$$

and so Eq. 1.53 allows to write this condition in the form

$$\phi > 2\Theta_{Y_0} \cot \alpha_{pl} \tag{1.55}$$

According to Eq.1.55, if the bending angle ϕ is larger than $3.46\Theta_{Y_0}$, the strongest inclined planes (-101) and (0-11) intersecting along the <111> axis are involved. Since in conditions of good alignment with the axis it is possible that the particles are channeled by the skew planes, the ideal condition for MVROC is obtained when the vertical angle of incidence (Θ_{Y_0}) exceeds the axial critical angle at least two or three times.

Chapter 2

ECHARM

The motion of relativistic charged particles under channeling condition is well approximated with classical physics equations and, as a consequence, also the potential and its related quantities [30]. A traditional approach for its calculation relies on the analytical representation of the screened Coulomb potential [80, 94–96], for which its average is made for planar and axial cases by taking into consideration the potential of the atoms lying in neighboring planes or axes.

Another possible approach is based on the expansion in Fourier series of the physical quantities of interest. Although this approach has been widely used in many research areas, for the case of channeling it has been developed to date only for particular monoatomic cubic crystals along major orientation [97–100]. The method based on Fourier expansion is more flexible than the former, inasmuch as it can be applied to any realistic model of the atomic potential. Moreover, it allows one to determine averaged one- and two-dimensional physical quantities for any axis and planes of the crystal.

A complete treatment and generalization of the method based on the expansion of the electric potential as a Fourier series, is presented. It allows one to calculate the physical quantities of interest even in complex atomic structures. The method allows to determining the physical quantities with good approximations and with reasonable calculation time. Moreover, x-ray measurements of electron density can be directly used for more precise calculations of the potential. Based on this method, we have developed the "ECHARM" program, which calculates one- and two- dimensional averaged physical quantities of interest along the main planes and axes of any orthorhombic and tetragonal structure and main planes of any structures. For the case of cubic symmetry, the calculation holds for any orientation. Complex structures like zeolites have been worked out to show the capability of the program.

2.1 Potential and related quantities in a periodic structure

In the following paragraphs we will find the expression for the potential with the method of the Fourier expansion, as described in Refs. [97–100]

2.1.1 General Background

A primitive cell and its basis determine a three dimensional periodic atomic structure. The whole structure is built through the translation vectors $\mathbf{a}_1$, $\mathbf{a}_2$, $\mathbf{a}_3$:

$$\mathbf{r_k} = k_1\mathbf{a}_1 + k_2\mathbf{a}_2 + k_3\mathbf{a}_3 \tag{2.1}$$

where $\mathbf{k} = (k_1, k_2, k_3)$ is a set of integer numbers. Let us consider for simplicity a perfect monatomic structure without thermal vibrations. $u(\mathbf{r})$ is a scalar function determined in the space and its integral on the volume is convergent over the whole space. Thus, $\mathcal{U}(\mathbf{r}) = \sum_{\mathbf{k}} \sum_{j=1}^{N_0} u(\mathbf{r} - \mathbf{r_k} - \mathbf{r}_j)$ can be represented by its Fourier transform $\mathcal{U}(\mathbf{q})$, $\mathbf{r}_j$ being the coordinates of the j-th atom in the primitive cell and N_0 the number of atoms in it. $\mathcal{U}(\mathbf{q})$ holds

$$\mathcal{U}(\mathbf{q}) = \int_V \mathcal{U}(\mathbf{r}) e^{i\mathbf{qr}} d\mathbf{r} = \sum_{\mathbf{k}} \sum_{j=1}^{N_0} u(\mathbf{q}) e^{i\mathbf{q}(\mathbf{r}_k + \mathbf{r}_j)} \tag{2.2}$$

where integration is made over the whole space V and where $u(\mathbf{q}) = \int_V u(\mathbf{r}) e^{i\mathbf{qr}} d\mathbf{r}$. Using the δ-function properties and by performing the reverse Fourier transform we get

$$\mathcal{U}(\mathbf{r}) = \frac{1}{\Delta} \sum_{\mathbf{g}} u(\mathbf{g}) S(\mathbf{g}) e^{-i\mathbf{gr}} \tag{2.3}$$

where Δ is the volume of the primitive cell and $S(\mathbf{g}) = \sum_{j=1}^{N_0} e^{i\mathbf{g}\mathbf{r}_j}$ is the structure factor. The term with $\mathbf{g} = 0$ in this sum is defined as:

$$\frac{1}{\Delta} u(\mathbf{g} = 0) S(\mathbf{g} = 0) = \frac{N_0}{\Delta} \int u(\mathbf{r}) d\mathbf{r} \tag{2.4}$$

2.1.2 The case of an ideal structure

Let us approximate the potential of a complex periodic atomic structure as a sum of single-atom potential:

$$\varphi(\mathbf{r}) \approx \sum_{\mathbf{k}} \sum_{j=1}^{N_0} u(\mathbf{r} - \mathbf{r_k} - \mathbf{r}_j) \tag{2.5}$$

where $u(\mathbf{r})$ is the potential of an isolated atom. The formula does not allow considering the delocalization of electrons among neighboring atoms. By expanding in Fourier series, it holds

$$\varphi(\mathbf{r}) = \frac{1}{\Delta} \sum_{\mathbf{g}} u(\mathbf{g}) S(\mathbf{g}) e^{-i\mathbf{gr}} \tag{2.6}$$

By performing the Fourier transform of the Poisson equation to express $u(\mathbf{g})$, one obtains:

$$\varphi(\mathbf{r}) = \frac{4\pi e Z}{\Delta} \sum_{\mathbf{g}\neq 0} S(\mathbf{g}) \frac{(1 - F(g))}{g^2} e^{-i\mathbf{gr}} \tag{2.7}$$

where e is the elementary charge, Z is the atomic number and $F(g)$ is the atomic form factor. Since the potential is defined except for an additive constant, the term with $\mathbf{g} = 0$ is subtracted.

The same procedure con be adopted to study the case of a polyatomic structure. In fact, the structure is defined as a superposition of N independent monoatomic structures with the same primitive cell and the same main period, $\varphi(\mathbf{r}) = \sum_{l=1}^{N} \varphi_l(\mathbf{r})$, where l runs over the N atomic species. As a result, for the periodic polyatomic structures, it holds:

$$\varphi(\mathbf{r}) = \frac{4\pi e}{\Delta} \sum_{\mathbf{g}\neq 0} \frac{1}{g^2} \sum_{l=1}^{N} Z_l S(Z_l, \mathbf{g})(1 - F(Z_l, g)) e^{-i\mathbf{gr}} \tag{2.8}$$

where $S(l, \mathbf{g}) = \sum_{j=1}^{N_l} e^{i\mathbf{g}\mathbf{r}_{\mathbf{j,l}}}$, $Z_l, F(Z_l, g)$ are the corresponding structure factors, atomic numbers and atomic form factors; $\mathbf{r_{j,l}}$ and N_l are the corresponding coordinates and number of atoms of l-species.

By starting from equation (2.8) physical quantities for an ideal periodic structure, such as the components of the electric field, the electron and atomic densities can be found.

2.1.3 The case of an ideal structure averaged over thermal vibration

Thermal vibrations influence the electric characteristics because of the change in the location of the atoms in the structure [9, 97]. As a consequence, we have to approximate the

potential by averaging over time and spatial fluctuations. As suggested in the literature [97], normalized probability density functions can be used to describe the space distribution of atom centers in the primitive cell. In principle, the method allows one to calculate averaged potential for any arbitrary real complex atomic structures. However, in this thesis we will work out only the case of isotropic independent thermal oscillations under the assumption that the amplitudes are the same for each atom of a given species. Under this assumption we obtain the three-dimensional potential averaged over thermal fluctuations

$$\varphi(\mathbf{r}) = \frac{4\pi e}{\Delta} \sum_{\mathbf{g}\neq 0} \frac{< Y(\mathbf{g}) >}{g^2} e^{-i\mathbf{gr}} \tag{2.9}$$

where

$$< Y(\mathbf{g}) >= \sum_{l=1}^{N} Z_l S(Z_l, \mathbf{g})(1 - F(Z_l, g)) e^{\frac{-A_l g^2}{2}} \tag{2.10}$$

where A_l is the mean square amplitude of the thermal vibration of l-th species. By starting from equation (2.10) physical quantities for an ideal periodic structure, such as the components of the electric field, the electron and atomic densities can be found.

2.1.4 Atomic Form Factors

Three types of approximations are used for atomic form factors, i.e. simple form factor, Moliére form factor and experimentally determined form factor. In the simple form factor approximation, the electrons are distributed in the neighborhood of the nuclei according, in reciprocal space, to the equation:

$$F(g) = \frac{1}{1 + g^2 R^2} \tag{2.11}$$

where $R = CZ^{1/3}\lambda_c$ (λ_c is Compton length of electron). The constant C is assumed to be 111 in default by the program, though it is possible to modify it.

The Moliére approximation is widely adopted in the literature to study channeling, and furnishes a result with comparable accuracy as for analytic calculations [80, 95]: the electron density is described, in reciprocal space, by the equation:

$$F(g) = 1 - g^2 \sum_{j=1}^{3} \frac{a_j}{b_j^2 + g^2} \tag{2.12}$$

where $a_1 = 0.1$, $a_2 = 0.55$, $a_3 = 0.35$, $b_j = Z^{1/3} c_j/(121\lambda_c)$, $c_1 = 6$, $c_2 = 12$, $c_2 = 0.3$.

The experimental form factor represents a precise approximation, which takes into account available data from x-ray measurements, from which one can fit the μ_j, β_j coefficients in the equation:

$$F(g) = \mu_0 + \sum_{j=1}^{4} \mu_j e^{-\beta_j g^2} \tag{2.13}$$

2.2 Planar and axial potentials under continuous approximation

2.2.1 Orthorhombic and tetragonal lattices

Previously obtained Eq.(2.9) can be used to describe potential of any perfect crystallographic structure. In this section, a focus on the orthorhombic and tetragonal lattice is proposed. A Cartesian coordinate system (x y z) with the axes directed along [100], [010], and [001] directions of the crystal is chosen. In this coordinate system, the vector $\mathbf{g}$ becomes:

$$\mathbf{g} = 2\pi(\frac{n_1}{a_1}\mathbf{e}_1 + \frac{n_2}{a_2}\mathbf{e}_2 + \frac{n_3}{a_3}\mathbf{e}_3) \tag{2.14}$$

where n_1, n_2, n_3 are integer numbers, a_1, a_2, a_3 are the periods of the lattice, $\mathbf{e_1}, \mathbf{e_2}, \mathbf{e_3}$ are the unit vectors along axes of the Cartesian coordinate system.

By using such coordinate system the planar and axial potential hold:

$$\varphi_p(x) = \frac{1}{S_p}\int\int_{S_p} \varphi(x,y,z)dydz \tag{2.15}$$

$$\varphi_a(x,y) = \frac{1}{L}\int_0^L \varphi(x,y,z)dz, \tag{2.16}$$

where S_p is the area of the projection of the primitive cell onto the (100) plane and $L = a_3$ is the period along the z-direction. By taking into account of Eq.(2.15), the reciprocal vectors sum runs only on n_3 index for the planar case, and runs only on n_2 and n_3 indexes for the axial case. The other physical quantities could be either obtained by a similar average.

2.2.2 Cubic lattice

For cubic lattice, Eq.(2.9) can be rewritten in a coordinate system with the axes defined by $[k_1k_2k_3]$, $[l_1l_2l_3]$ and $[m_1m_2m_3]$ Miller indexes.

$$\varphi(\mathbf{r}') = \frac{4\pi e}{\Delta} \sum_{\mathbf{g}\neq 0} \frac{< Y(\mathbf{g}) >}{g^2} e^{-iG\xi(x',y',z')} \tag{2.17}$$

where $G = 2\pi/a$, $\mathbf{g} = G(n_1\mathbf{e}_1 + n_2\mathbf{e}_2 + n_3\mathbf{e}_3)$, a is the side of the cube and with:

$$\xi(x', y', z') = \sum_{i=1}^{3} (n_i k_i x'/k_s + n_i l_i y'/l_s + n_i m_i z'/m_s) \tag{2.18}$$

where $k_s = \sqrt{k_1^2 + k_2^2 + k_3^2}$, $l_s = \sqrt{l_1^2 + l_2^2 + l_3^2}$, $m_s = \sqrt{m_1^2 + m_2^2 + m_3^2}$, and n_i runs from $-\infty$ to $+\infty$.

By introducing other integer numbers $N_1,\ N_2,\ N_3$, connected with previous numbers $n_1,\ n_2,\ n_3$ by the relations:

$$n_1k_1 + n_2k_2 + n_3k_3 = N_1 \tag{2.19}$$

$$n_1l_1 + n_2l_2 + n_3l_3 = N_2 \tag{2.20}$$

$$n_1m_1 + n_2m_2 + n_3m_3 = N_3 \tag{2.21}$$

the potential can be rewritten as:

$$\varphi(\mathbf{r}') = \frac{4\pi e}{\Delta} \sum_{\mathbf{g}\neq 0} \frac{< Y(\mathbf{g}) >}{g^2} e^{-iG(N_1x'/k_s + N_2y'/l_s + N_3z'/m_s)} \tag{2.22}$$

The axis along the $[m_1m_2m_3]$ direction is defined by simultaneously satisfying Eq.(2.19) and (2.20) with fixed $N_1,\ N_2$. The averaged potential along the $[m_1m_2m_3]$ axis holds:

$$\varphi_a(x', y') = \frac{1}{L} \int_0^L \varphi(x', y', z')dz', \tag{2.23}$$

where L is the period of potential variation along this axis. By integrating Eq.(2.22) and selecting the terms with $N_3 = 0$ in the Fourier series we obtain the axial potential along $[m_1,\ m_2,\ m_3]$ axis holds

$$\varphi_a(x',y') = \frac{4\pi e}{\Delta} \sum_{n_1,n_2=-\infty}^{+\infty} \frac{< Y(n_1,n_2,n_3) >}{g^2} e^{-iG(N_1x'/k_s + N_2y'/l_s)} \tag{2.24}$$

In a similar manner, the planar potential for an arbitrary plane of the cubic lattice is:

$$\varphi_p(x') = \frac{4\pi e}{\Delta} \sum_{N=-\infty}^{+\infty} \frac{< Y(n_1,n_2,n_3) >}{g^2} e^{-iGNk_sx'} \tag{2.25}$$

where $n_i = Nk_i$.

2.3 Planar characteristics for main planes

Under the continuous potential approximation, the analytic potential by a potential averaged over a direction parallel to the crystal planes holds

$$\varphi_p(x) = \frac{1}{S_p} \int \int_0^{S_p} \varphi(x,y,z) dydz \tag{2.26}$$

Substituting Eq. 2.9 into Eq. 2.26 and using the crystal system coordinates we obtain for the (100) plane:

$$\varphi_p(x) = \frac{1}{S_p} \int \int_0^{S_p} \frac{4\pi e}{\Delta} \sum_{\mathbf{g}\neq\mathbf{0}} \frac{< Y(\mathbf{g}) >}{g^2} e^{-i\mathbf{g}(\mathbf{xe_1}+\mathbf{ye_2}+\mathbf{ze_3})} dy'dz' \tag{2.27}$$

Where $\mathbf{e_i}$ are the base vectors. As a result we reach the equation for the potential averaged over the (100) plane, in which $\mathbf{r'} = \mathbf{r}$:

$$\varphi_p(x) = \frac{4\pi e}{\Delta} \sum_{n_1} \frac{< Y(\mathbf{g}) >}{g^2} e^{-i\frac{2\pi}{a_1}n_1} \tag{2.28}$$

It is easy to reproduce this result for the (010) and the (001) planes.

2.4 Program for calculations of the potential

Aside from the theoretical study in previous section and before we provide examples of calculation of the potential, we describe a program we developed, called ECHARM (Electrical CHARacteristics of Monocrystals) to enable a non-expert user for the calculation of the averaged potential of complex atomic structures.

2.5 Examples of calculations

2.5.1 Simple Structures

As a first test bench, the potential in silicon through Moliére approximation and with the usage of x-ray data is compared with the results in the literature.

Fig.2.1 shows the (111) and (110) Si planar potential. One observes the typical two-well shape for (111) orientation with a large (l) and a small (s) wells, whose maximum depth is $U_0 = 25.68$eV (l), and a single well for (110) orientation ($U_0 = 23.39$eV). The same quantities were calculated for germanium, $U_0 = 41.82$eV and $U_0 = 40.67$eV for (111) and (110) orientations, respectively.

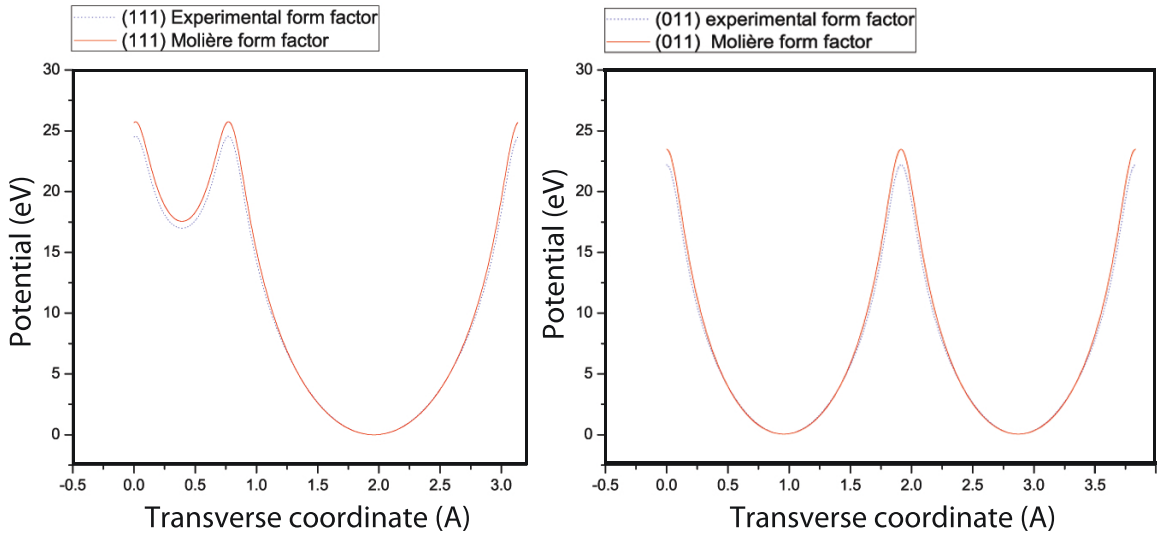

Figure 2.1: Calculation of potential between (111) planes and (110) planes in Si with Moliére atomic form factor and the form factor achieved by x-ray experiments. The potential calculated with the latter method is lower than for the former method, especially in proximity of the atomic planes.

By replacing the Moliére approximation with the experimentally achieved form factor by x-ray diffraction [101, 102], a decrease in the potential barrier height by less than 10% is observed (Fig.2.1).

Computed axial potential depths for [111] ($U_0 = 117$eV) and [011] ($U_0 = 152$eV) directions in a silicon crystal are in good agreement with Ref.[9] ($U_0 = 106$eV and $U_0 = 140$eV, respectively) and in fair agreement with Ref.[57] ($U_0 = 105$eV and $U_0 = 114$eV, respectively). This discrepancy owes to the contribution of all axes to the potential as is in our case while other methods accounts for only neighboring axes.

Lastly, the detailed comparison of the method with the method based on the analytical expression of the Moliére potential is carried out (see [57, 80, 95, 96]). Usually, in this method the potential is calculated in approximation of the two neighboring crystallographic planes ($\varphi_{2p}(x)$). Tab. 2.5.1 shows calculations taking into account different number of planes. $\varphi_X(x)$ denotes potential calculated with the usage of x-ray measurements and for zero thermal vibration amplitude ($\varphi_{2pS}(x)$ and $\varphi_{MS}(x)$).

$\nu = 2x/d$	$\varphi_{2p}(\nu)$	$\varphi_{4p}(\nu)$	$\varphi_{6p}(\nu)$	$\varphi_M(\nu)$	$\varphi_X(\nu)$	$\varphi_{2pS}(\nu)$	$\varphi_{MS}(\nu)$
0	0	0	0	0	0		
0.2	0.605	0.633	0.635	0.635	0.623	0.598	0.628
0.4	2.545	2.662	2.668	2.669	2.550	2.513	2.635
0.6	6.329	6.601	6.615	6.617	6.043	6.224	6.510
0.8	13.421	13.930	13.956	13.959	12.469	13.104	13.639
1.0	22.465	23.313	23.356	23.360	21.383	27.577	28.466

Table 2.1: Different calculations of potential of the (110) silicon plane as a function of relative coordinate $\nu = 2x/d$, where d is the interplanar distance. The point $x = 0$ corresponds to a mimimum of the potential.

2.5.2 Complex Structures: Zeolites

Zeolites are largely studied materials because of their widespread applications, spanning from heterogeneous catalysis to gas purification [103]. A natural zeolite is an aluminosilicate framework, whose structure contains cavities filled with water and exchangeable cations. The primary buildings units of the structures of silicates are the TO4 tetrahedra, where T is mainly Si. The extraframework cations in the structure (usually K, Na, Ca, less frequently Li, Mg, Sr, Ba) often result in significant change of both physical and chemical properties. Under some circumstances, neighboring cavities merge to form long channels, which are periodically repeated over the whole structure and may form a bundle of parallel nanotubes. These crystals are ideal cases for particle capture via axial channeling. Moreover, the knowledge of precise data about the potential in zeolites allows to design experiments about Coulomb explosions of charged molecules in crystals. Pioneering experiment in this sense have been carried out in silicon crystal [104], though the wide channels offered by a zeolite should increase the efficiency of the method. Among the immensely wide variety of zeolites, we selected the species that possess broad channels, good thermal stability and, ultimately, that exist as relatively large crystals to be used for experiments.

The simulated sample is mordenite [103, 105, 106], whose potential, electric field, atomic

density and density of electrons along the [001] axis are illustrated in Fig.2.2. The crystal lattice is orthorhombic ($a_1 = 18.007$Å, $a_2 = 20.269$Å, $a_3 = 7.465$Å) and Si, Al and O atoms form its base. Ca cations have been added to the framework in the locations at which such ions are bound to the framework. The profile of the potential exhibits nearly a field-free 14eV deep channel, extending roughly 9 in diameter. The depth of the potential well is comparable to that of silicon.

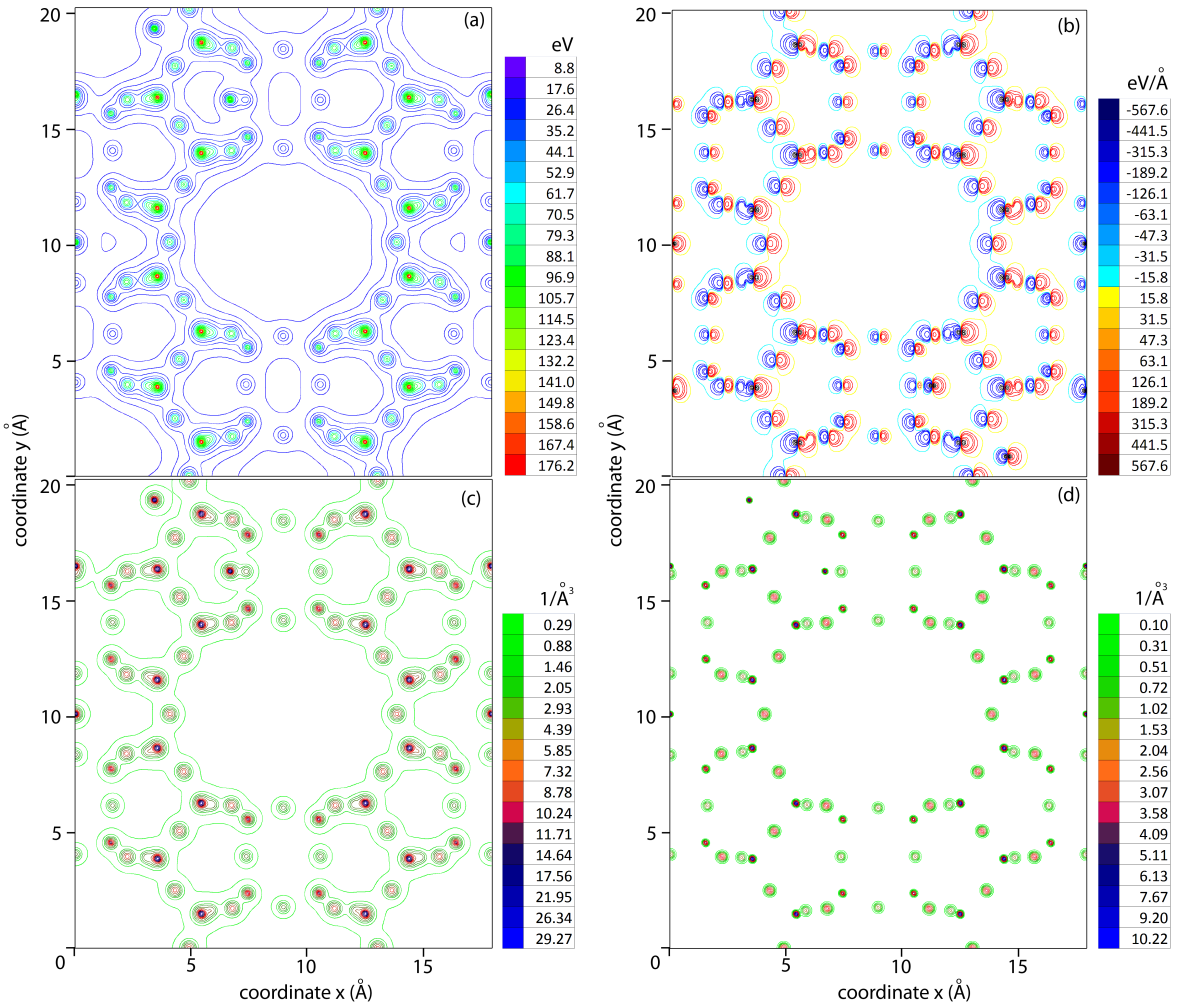

Figure 2.2: Contour plot of physical quantities of interest along the [001] axis of Mordenite at $T = 300K$, as a function of coordinate x and y. (a) Potential: a wide channel with uniform potential is visible on the center of the figure. The ion breaking the symmetry of the potential are Ca^{++} cations bound to the well of the channel. (b) Electric field (x component). (c) Electron density. (d) Atomic density: this figure gives a picture of the extent of the atomic oscillations in the crystal.

2.5.3 Hexagonal structure: lithium niobate

Lithium Niobate is a synthetic crystal which exhibits extraordinary characteristics, such as piezoelectricity, ferroelectricity and pyroelectricity . Its possible usages spread out from acousto-optic filters to amplitude modulator. Lithium niobate possess hexagonal structure. Its base is composed by one lithium atom, one niobato atom and three oxygen atoms. We use the extension of the ECHARM program to evaluate its potential along the major planar orientation. In Fig. 2.3 we expose the potential, the electric field, the density of atoms and the density of electrons felt by a particle hitting the crystal parallel to the (010) plane. It is necessary to underline that, instead the depth of the potential well ($U_0 = 25.49$ eV), the channeling efficiency in this peculiar crystal is affected by the multiple scattering. As a result this crystal appears a perfect aspirant to apply the volume reflection effect for charged particle beam deflection.

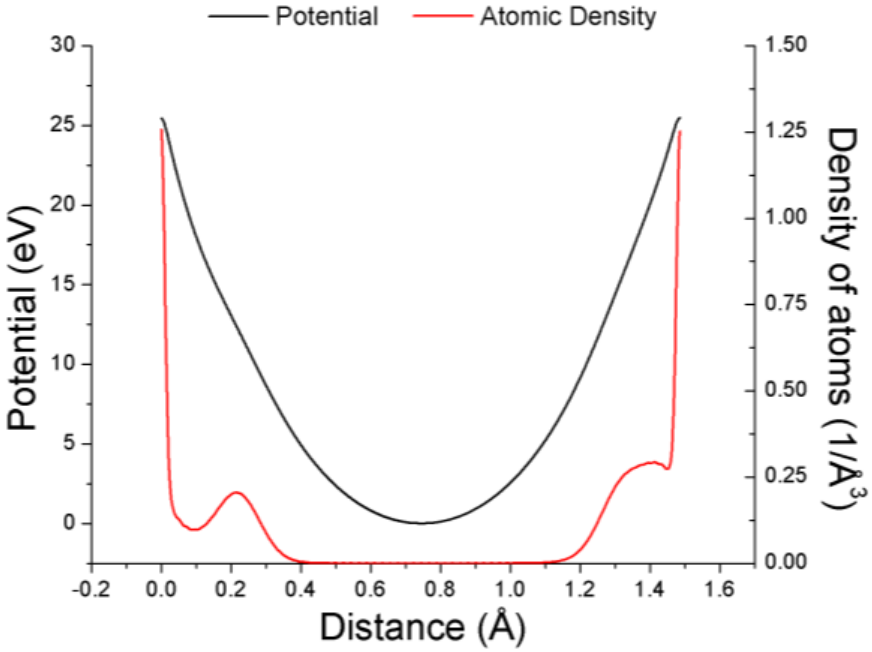

Figure 2.3: Calculation of potential and density of atoms between (010) planes in lithium niobate crystal at the room temperature (T= 300 K). The form factor used was the Moliére form factor.

Chapter 3

DYNECHARM++

The DYNECHARM++ code is a a toolkit to simulate coherent interactions of high-energy charged particles in complex straight and bent structures. The toolkit has been designed to be easily updatable and integrable in third-party softwares. Only C++ standard libraries have been used. Because of the object-oriented programming mode, each class can be singularly added to other codes. The toolkit allows to work out the simulations through by starting from the parameters of a strip and a particle. The electrical characteristics of a crystal can be calculated numerically with different methods, such as the usage of expansion in Fourier series or the harmonic approximation of the potential energy. Particle trajectory in the interaction with a strip is evaluated by integrating numerically the equation of motion of the particle.

The main advantage of the code with respect to others is the capability to simulate not only orientational phenomena in common structure as Si and Ge, but also in complex structures as Zeolite, graded crystal, crystals with lattice defects, etc... with very little work thanks to the object-oriented programming and the integrated computation of the electric characteristics of the crystals. Indeed, the flexibility given by the C++ language allows to easily add to the code new classes to describe such phenomena. In fact, the toolkit has already been used for the simulation of two experiments concerning the coherent phenomena in graded $Si_{1-x}Ge_x$ self-bent crystals [52] and the dechanneling length for negative pions [51].

3.1 Main classes

The `DYNECHARM++` toolkit has been fully written in C++ programming language. Members of the classes are all protected and can be accessed only by specific reading and writing

methods. Classes are linked by pointers with small-abuse of physical memory copies of objects. The code can be expanded and updated by overloading specific virtual functions of base classes. No external libraries have been adopted in standard configuration. If specific environmental variables are defined, results can be automatically written in ROOT files [107] and some code pieces can take advantage of multi-core systems [108]. The main class-hierarchy is shown in Fig. 3.1. The `ECHARM_simulation` class is responsible for calculation of the results of coherent interactions between a beam and a strip, described by the `ECHARM_particle` and `ECHARM_strip` classes, respectively.

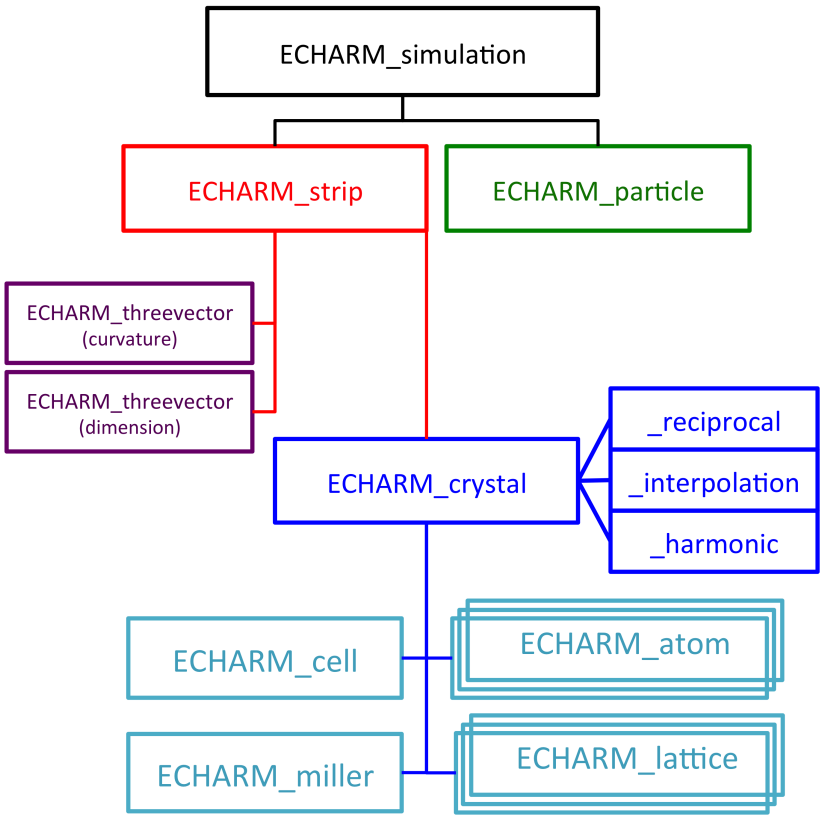

Figure 3.1: Classes up-to-down hierarchy and dependences in `DYNECHARM++`. `ECHARM_crystal` and `ECHARM_simulation` derived classes have been added to the right of the `ECHARM_crystal` and `ECHARM_simulation` base classes, respectively.

3.1.1 ECHARM_beam

ECHARM_particle is a stand-alone base class in which the fundamental properties of a single particle are collected. The class contains the fundamental properties of a particle and the methods to access them. To construct an object the minimum elements are the atomic number Z, the mass in the particle reference frame, the three-vector for the momentum and the three-vector for the position of the particle in the space. Several methods have been added for the calculation of properties such as velocity in c unit, the total energy, Lorentz factor. A collection of ECHARM_particle objects can be stored in a ECHARM_beam object. A percentage is associated to each particle kind. Such object contains also a distribution function for initial three-vector position and momentum. The ECHARM_beam class is used to create an object which produces the particles at the entrance of a strip in a three-dimensional space.

3.1.2 ECHARM_strip

A strip can be schematized by a three-dimensional object to which a periodical structure is applied. Thus, the ECHARM_strip class is mainly composed by a pointer to the class for a crystal, ECHARM_crystal class and two three-vector pointers containing the geometric dimension and the curvature radiuses of the strip. Due to the usage of pointers instead of physical copy of objects the ECHARM_strip class can be easily updated operating over its constituents also during the run-time. Thereby, variable curvature radiuses can be applied to the strip to treat not homogeneous samples, e.g. a crystalline undulator [109] through the usage of user-defined functions with no update of the toolkit framework. A specific class to describe a crystalline undulator has been developed and is treated in the next section.

A crystal is the sum of many bases within a unit cell. Each base is the union of a lattice and an atom. An ECHARM_crystal object is created by inputing an ECHARM_cell object, a pair of ECHARM_atom and ECHARM_lattice objects and a ECHARM_miller object. The ECHARM_miller class contains Miller indexes of main plane and main axis along particle trajectory. The ECHARM_crystal class is a child class of the ECHARM_atom class and contains all the material properties. averaged over the constituent atomic species.

The ECHARM_atom contains the fundamental properties of a single atomic element of a crystal. An ECHARM_atom object is created by inputing the atomic number Z, the mass number, the Debye temperature, the temperature, the average ionization constant and the kind of form factor to be used in computation. In addition to retrieval and set methods, the

class allows to compute the form factor with several approximations. In fact, the available models are the single exponential, the Moliére model, the Lindhard model, the usage of experimental data from x-ray analysis.

The geometric properties of the crystal cell are defined by a pointer to a single `ECHARM_cell` object. Thus, the three-vector of the size and the angle of the unit cell are stored in the class. With the class a user is able to compute the volume of the unit cell, the direct and reciprocal period and reciprocal vector squared for particular Miller indexes.

The `ECHARM_atom` contains the fundamental properties of a single atomic element of a crystal. An `ECHARM_atom` object is created by inputing the atomic number Z, the mass number, the Debye temperature, the temperature, the average ionization constant and the kind of form factor to be used in computation. In addition to retrieval and set methods, the class allows to compute the form factor with several approximations. In fact, the available models are the single exponential, the Moliére model, the Lindhard model, the usage of experimental data from x-ray analysis.

In the `ECHARM_lattice` the placement of a specific atom kind within a base cell are stored. The class contains vector of three-vectors which determines the position of the atom in the unit cell. The computation of structure factor is performed through a specific method of the class. Several common lattices are already present, such as simple cubic, face-centered cubic and diamond.

The `ECHARM_crystal` has several virtual methods to retrieve electrical characteristics of the crystal. Usage of virtual functions allow to create derived classes within which various calculation methods can be defined. Thereby, user-classes can be simply added to the standard `DYNECHARM++` classes through the definition of a derived `ECHARM_crystal` class in which the retrieval methods are explicated. Because of the usage of continuum potential approximation [30] within many kinds of coherent-effects simulation, retrieval functions for electrical characteristics averaged along a planar or an axial directions have to be defined. Standard `DYNECHARM++` functions of `ECHARM_crystal_reciprocal`, have been inherited by the calculation methods of `ECHARM` [79, 110]. In `ECHARM` calculation method relies on the expansion in Fourier series of the electrical characteristics of crystal. Due to the intrinsic period structures of the crystal, evaluation is conducted in reciprocal space and then re-conducted in the real space. The `ECHARM` calculation method is widely reported in the specific chapter. Unfortunately, due to the necessary need of cycle over the Fourier-coefficients terms, `ECHARM_crystal_reciprocal` calculation method become very CPU-time-consuming during a simulation. As a consequence the specific `ECHARM_crystal_interpolation` class has been inserted within `DYNECHARM++`, based on the interpolation algorithms.

`ECHARM_crystal_interpolation` class provides a few methods of interpolation. The simplest is the linear algorithm

$$\varphi(x) \approx \begin{pmatrix} 1-x' & x' \end{pmatrix} \begin{pmatrix} \varphi(0) \\ \varphi(1) \end{pmatrix} \tag{3.1}$$

where x is the position along the direction orthogonal to the main plane in unit of distance between two points of the array. The two dimensional vector is used to store electric characteristics averaged along axial direction. For a two dimension vector the algorithm is called bilinear, which holds

$$\varphi(x', y') \approx \begin{pmatrix} 1-x' & x' \end{pmatrix} \begin{pmatrix} \varphi(0,0) & \varphi(0,1) \\ \varphi(1,0) & \varphi(1,1) \end{pmatrix} \begin{pmatrix} 1-y' \\ y' \end{pmatrix} \tag{3.2}$$

where x' and y' are the position along the two directions orthogonal to the main axis in unit of distance between two points of the array. Linear interpolation method requires as a mandatory task to preliminary load in memory electrical characteristics. Memory access delay time is the only computation-bottleneck of linear interpolation method because of no need of intense CPU usage. A second algorithm implemented is the cubic and bicubic interpolation, which relies on the approximation with a third order function instead of a first order one. Thus, the characteristic is evaluated in one dimensions by

$$\varphi(x', y') \approx a_0 + a_1 x + a_2 x^2 + a_3 x^3 \tag{3.3}$$

where a_0, a_1, a_2 and a_3 are

$$\begin{aligned} a_0 &= \varphi(1) && (3.4)\\ a_1 &= -0.5\varphi(0) + 0.5\varphi(2) && (3.5)\\ a_2 &= \varphi(0) - 2.5\varphi(1) + 2.0\varphi(2) - 0.5\varphi(3) && (3.6)\\ a_3 &= -0.5\varphi(0) + 1.5\varphi(1) - 1.5\varphi(2) + 0.5\varphi(3) && (3.7)\\ & && (3.8) \end{aligned}$$

A third class based on the simple harmonic approximation of the potential [57] averaged along planar direction is also present, the `ECHARM_crystal_harmonic` class. Harmonic approximation holds only under specific conditions and is standardly used to evaluate the parameters of coherent effects for standard crystal, such as Si and Ge, along main planes,

e.g. (110) planes

$$\varphi(x) \approx \varphi_{max}(2x/d_{p,x})^2 \tag{3.9}$$

where $d_{p,x}$ is the interplanar distance along the x direction and φ_{max} is the maximum of the potential well.

3.1.3 `ECHARM_simulation`

The `ECHARM_simulation` class is a virtual class for the description of the calculation model and its application in the interaction of a particle with a strip. `ECHARM_simulation` class collects pointers to one `ECHARM_crystal` object and one `ECHARM_particle` object. Within the `ECHARM_simulation` base class only common parameters of coherent effects are defined, such as critical angle of channeling $\theta_c = (2\varphi_{max}/p\beta)^2$ and critical radius $R_c = p\beta/e\varphi'_{max}$, where $p\beta$ are the particle momentum and velocity, e the electron charge and φ'_{max} the maximum electric field. Calculation methods have defined in derived classes. With the standard DYNECHARM++ code the three derived classes are included.

The `ECHARM_simulation_integration` class holds the integration of the motion of a point-like particle under planar (Eq. 3.10) and axial (Eq. 3.11) continuum potential approximation. The trajectory is evaluated through the integration of the ultra-relativistic equation of motion in the non-inertial reference frame orthogonal to the crystal plane. Thereby, the strip curvature affects particle motion causing a centrifugal force inversely proportional to the local bending radius of the strip.

$$p\beta\frac{d^2x}{dz^2} + \varphi'(x) + \frac{p\beta}{R_x(x,y,z)} = 0 \tag{3.10}$$

$$\begin{cases} p\beta\frac{d^2x}{dz^2} + \varphi'_x(x,y) + \frac{p\beta}{R_x(x,y,z)} = 0 \\ p\beta\frac{d^2y}{dz^2} + \varphi'_y(x,y) + \frac{p\beta}{R_y(x,y,z)} = 0 \end{cases} \tag{3.11}$$

The integration is carried out via the Velocity-Verlet algorithm with a variable integration step. To reach an acceptable compromise between computation-time and precision of calculation a suitable integration step range has to be chosen, typically of the order of tens of nanometers. Such algorithm guarantees a fourth-order $O(z^4)$ error over a single step with no exaggerated computation-time, i.e. it takes less than a second to evaluate the trajectory of a 400 GeV/c proton under planar channeling in a 2-mm thick Si crystal.

Because of the existence of exotic samples, e.g. multi-strips [39, 40, 46, 50], and ex-

periments which do no need other than well-known coherent effects such as collimation experiments [18, 26, 27, 111, 112], the derived class `ECHARM_simulation_blackbox` has been developed, in which the strip acts as a "black box" which modifies particle trajectory. The `ECHARM_simulation_blackbox` class collects many derived `ECHARM_coherent_effects` objects. The `ECHARM_coherent_effects` base class contains a single coherent effect to which is associated a PF (Probability Function) for determination of the angular range and probability that the interaction occurs, and ODF (Outgoing Distribution Function) for determination of the outgoing angular deflection distribution if the interaction has occurred. PF and ODF functions make use of analytical approximation and experimental data. The usage of `ECHARM_simulation_blackbox` class allows evaluating the trajectories of one million of particles on a standard personal computer in few seconds. The model is described in the specific section.

The third class included is a derived class of the `ECHARM_simulation_integration` class and is called `ECHARM_simulation_integration_averaged`. Within the class the particle trajectory is integrated for various initial energy to compute the average density of material "seen" by a particle. Thus, a vector containing the average density as a function of the initial transverse energy is stored. The channeling efficiency is computed by applying an exponential decay of efficiency depending on the initial transverse energy of a particle. The model is described in section 1.2.2.

3.1.4 `ECHARM_multiple_scattering`

Because of the object-oriented nature of `DYNECHARM++` toolkit, physics classes can be added to enhance the realism of the simulation.

The `ECHARM_multiple_scattering` class groups many multiple scattering functions for amorphous media [113] and the `ECHARM_bethe_bloch` collects functions which describe the average energy loss due to interaction with electrons. The Highland approximation is adopted for the description of multiple scattering. The approximation is based on the fit of experimental data and holds:

$$\left\langle \frac{dp_x^2}{dz} \right\rangle_{am} = 13.6\text{MeV}\frac{Z}{p\beta}\sqrt{\frac{z}{X_0}}(1.0 + 0.038\log\frac{z}{X_0}) \tag{3.12}$$

where Z is the atomic number of the material, $p\beta$ is the particle momentum-velocity, z is the crossed material length, X_0 is the radiation length of the material and dp_x^2/dz is the root-mean-square of transverse energy variation in amorphous media.

Although models perform well in simulating interaction of particles with amorphous

media [114], simulation of coherent effects can not be worked out correctly in the same manner. In fact, intensity of incoherent interactions for particles under coherent effects strongly depends on local nuclei and electronic density. Thereby, the intensity of interaction in amorphous media is weighted with respect to the nuclear and electronic density averaged transverse to the crystal planes or axes as in Ref. [81]. Such approximation still valid for interaction with both nuclei and electrons [81]. Root-mean-square of transverse energy variation in crystal turns into a function of particle position, e.g. it is valid to treat intensity of interactions under planar condition

$$\left\langle \frac{dp_x^2}{dz} \right\rangle = \left\langle \frac{dp_x^2}{dz} \right\rangle_{am} \frac{n(x)}{n_{am}} \tag{3.13}$$

where $\left\langle \frac{dp_x^2}{dz} \right\rangle$ is the root-mean-square of transverse energy variation in crystal, $n(x)$ is the atomic density along the crystal plane, n_{am} is the average crystal atomic density.

3.1.5 `ECHARM_defect`

The `ECHARM_defect` C++ class has been specifically developed for the DYNECHARM++ toolkit to simulate the influence of defects on coherent effect. Various kinds of defects may affect the displacement of the atoms in a crystal. Defects can be grouped by the number of dimensions in the lattice on which they act, i.e.,point-like (interstitial atoms and vacancies), linear (dislocations), two-dimensional (stacking-faults), and three-dimensional (amorphous clusters) defects [69]. Defects are typically described through the Burger vector, i.e.,a vector that represents the magnitude and direction of the lattice distortion of defects in the crystal [115]. According to a specific investigation about the influence of defects to channeling of high-energy particles [116], point-like and third-order defects negligibly affect channeling efficiency ($\ll 0.01\%$). On the contrary, the presence of a single stacking-fault would causes strong reduction ($\simeq 65\%$) of the channeling efficiency, practically destroying channeling at high-energy. On the other hand, first-order defect would affect the channeling efficiency by approximately $\simeq 20\%$. Thus, this kind of defect have been thoroughly considered for simulating the particle dynamics in a crystal. As depicted in Fig. 5.5.b, the first-order dislocation manifests itself as an extra-plane which causes a stress field around the edge. The displacement field for the edge defect is quantified through experimentally verified [117] analytical equations [118]. Starting by the displacement field, its derivatives and particle position and momentum vectors, the point-to-point centrifugal force acting on the particle is computed in the reference frame orthogonal to the crystal planes. The position of each dislocation is randomly generated by defining the number of dislocation per cm^2.

3.1.6 ECHARM_undulator

The ECHARM_undulator class allows to describing the main features of a perfect crystalline undulator in order integrate the trajectory of a particle. The class inherits the main functions for the computation of the first and second derivative by a more general class, the ECHARM_osculator_radius. In fact, the main purpose is to compute point by point the curvature radius in a strip and it is done by approximating it through an oscillator radius. Thus, the class contains the functions to compute first and second derivative numerically by starting from a general formula which describe in two or three dimension the radius point by point as a function of the position in absolute unit. At each step of a particle in a strip the curvature radius is computed and the value is copied on the three-vector object which describes the curvature radius of the strip. Then the particle trajectory is integrated in the reference frame orthogonal to the crystal planes. For the first order approximation of crystalline undulator the sinusoidal approximation has been used.

$$x = A_x \sin\left(\frac{2\pi}{\lambda_x} z\right) \tag{3.14}$$

$$y = A_y \sin\left(\frac{2\pi}{\lambda_y} z\right) \tag{3.15}$$

where A_x, A_y and λ_x, λ_y are the oscillation amplitude and oscillation period for the direction orthogonal and parallel to the main crystal plane.

3.2 "Black-box" model

The "black box" model is a Monte Carlo model for the simulation of coherent planar interaction of positive particles in bent silicon crystals. A specific sequential code based on the "black box" model has been implemented into DYNECHARM++. It makes use of analytical approximations [57, 119, 120] and experimental data [36, 38] to calculate the cross section of main coherent and incoherent phenomena. Coherent and incoherent phenomena taken into account include channeling (CH), dechanneling (DCH), volume reflection (VR), volume capture (VC) and multiple scattering (MS).

The model inherits its name by the particular kind of description of a crystal in the simulation, since what happens inside the crystal is not described at all. The main disadvantage of this approach relies on the possibility to consider only coherent interactions for which a cross-section has been already measured. On the other side, the main advantage

is the saving in term of computation time. In fact, a Monte Carlo simulation with one crystal takes 1.66 milliseconds per particle on a 2.2 Ghz Intel Core 2 Duo.

The model has been developed in order to simulate multiple volume reflection in a multi-crystals object (MVRMC). Two main reasons support the usage of to the model for MVRMC simulation. The first reason concerns time. The computation time for a series of crystal is directly proportional to the number of crystals. As a consequence, a fast method to simulate a single crystal is needed. The second reason is the physics involved in the MVRMC. In fact, only planar effects for positive particles in bent crystals are involved. Since theoretical knowledge of coherent planar phenomena has been largely verified through results [36, 37, 37, 38, 40, 41, 46], the simulation of the deflection distribution has no need for a full description of the particle trajectory inside a single crystal.

In the "black box" model a particle is described by four parameters, i.e. momentum vector and atomic number. A crystal by four parameters, i.e., length along beam direction, curvature radius, crystal plane of channeling and angle between beam direction and crystal plane. An interaction between a particle and a crystal is associated to a single phenomenon. Each phenomenon has been associated to two subroutines, namely, PF (Probability Function) for determination of the angular range and probability that the interaction occurs, and ODF (Outgoing Distribution Function) for determination of the outgoing angular deflection distribution if the interaction has occurred. CH, VR and VC routines are called sequentially. DCH can occur only if particle has undergone CH or VC. If no coherent interaction takes place, MS routine is called. The scheme of the order of calling for subroutines is shown in Fig. 3.2.

The PF and ODF subroutines depend on six parameters, two regarding the incoming positive particle characteristics (the particle momentum along beam direction and the atomic number), three regarding the crystal characteristics (R, L_{cr} and the crystal plane of channeling) and one regarding the reciprocal alignment of the particle trajectory with the crystal plane (θ_{in}). When particles do not interact coherently they undergo incoherent interaction, i.e., multiple scattering, as approximated by the theory of Molière [121], with angular distribution width given by [113, 122].

Probability function in PF subroutine for CH has been evaluated through harmonic approximation of the potential well and angular range through the condition $|\theta_{in}| < \theta_c$. As the condition about the angular range is met, the function that describes CH probability in PF subroutine is:

$$\epsilon_{CH}(\theta_{in}) = \epsilon_{CH,max}\left(1 - \frac{R_c}{R}\right)\left(1 - \frac{\theta_{in}^2}{\theta_c^2}\right)^{\frac{1}{2}} \tag{3.16}$$

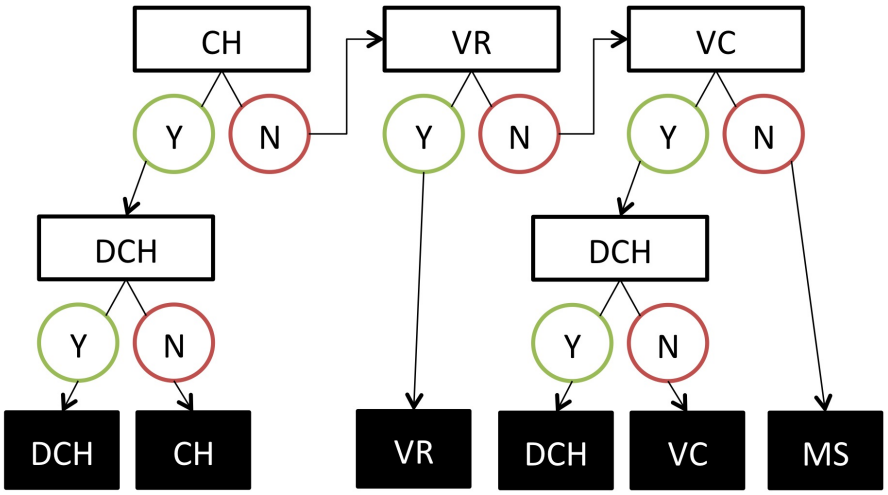

Figure 3.2: Scheme of the order of calling for the subroutines in the "black box" model. White and black boxes represent Probability Function (PF) and Outgoing Angular Distribution (ODF) subroutines, respectively.

.

where $\epsilon_{CH,max}$ is the maximum efficiency for channeling. The angular distribution of outgoing particles in ODF subroutine is a Gaussian function centered at θ_x and with standard deviation equal to θ_c.

Probability function in PF subroutine for DCH has been described by CH probability function multiplied by an exponential decay function, whose decay length L_{DCH} is calculated by solving the diffusion equation of particle in a crystal.

$$\epsilon_{DCH}(\theta_{in}) = \epsilon_{CH}(\theta_{in})e^{-z/L_{DCH}} \tag{3.17}$$

where z is the particle penetration depth in the crystal. In ODF subroutine, the distribution function is a Gaussian function with standard deviation equal to θ_c and average equal to the ratio between the coordinate z at which dechanneling occurs and R.

VR occurs as particle trajectory is tangent to a crystal plane, which represents the angular-range condition in PF subroutine, i.e., the crystal deflection angle. The dependence of PF probability and ODF on R and particle momentum has been evaluated by combining experimental data and tabulated Monte Carlo solutions of the differential equation of motion, because no solved analytic equation to describe their behavior does exist to date.

VC can be described as the time reversal of DCH. The angular-range condition in PF for VC holds the same range for which VR may occur, too. The probability function in

PF is complementary to that of VR, because VC occurs when VR does not.

$$\epsilon_{VC}(\theta_{in}) = 1 - \epsilon_{VR}(\theta_{in}) \tag{3.18}$$

Outgoing angular distribution in ODF is a Gaussian with mean value equal to the ratio between the length difference of L_{cr} and z at which VC occurs and R; its standard deviation is equal to θ_c.

The effect of repeated interaction with all the crystal in a multi-crystal has been carried out by simulating the interaction of every particle with a single strip and using the outgoing angular distribution as the initial angular distribution for next strip. Each strip possesses the parameters of a single strip and, additionally, other two parameters, i.e., the relative angular alignment α_{strip} and height H_{cr} with respect to the first strip. As a consequence, evolution of particle angular and spatial distributions after every strip can be tracked to obtain useful information on MVRMC.

3.3 Examples of calculations

Simulation of two kinds of strip has been worked out to test the `DYNECHARM++` capabilities. The code run on a linux system with kernel 3.2.0-35-generic and gcc compiler 4.6.3. The computer was a standard personal computer with 8 GB of RAM and Intel(R) Core(TM) i7-2600K CPU running at 3.40GHz. The electrical characteristics of each crystal are evaluated through the `ECHARM_crystal_reciprocal` class and stored in specific vectors of a `ECHARM_crystal_interpolation`. Then, the particle trajectories are integrated through the `ECHARM_simulation_integration` which retrieve electrical characteristics from the `ECHARM_crystal_interpolation` object. In such a way, the capability of the code to evaluate electrical characteristics is mixed with the need of reduction of computation time, which is obtained through the usage of `ECHARM_crystal_interpolation` class.

3.3.1 Bent Si strip

The first simulation deals with the reproduction of the results published in Ref. [43]. A 400 GeV/c proton beam interacts with 1.94 mm thick Si strip 38 m bent along the beam direction. Aim of the experiment was to measure nuclear dechanneling length, i.e. the decay length for the channeling process in thin crystal, which depends on the rate of incoherent interaction suffered by a channeled particle. As a side result deflection efficiency

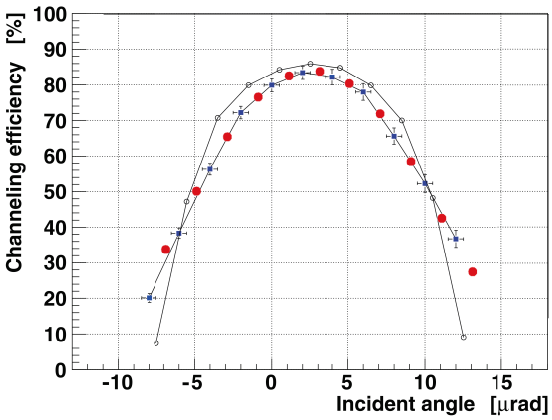

Figure 3.3: Deflection efficiency vs horizontal incoming angle for a 400 GeV/c proton beam impinging on a 38 m bent Si strip.

as a function of horizontal incoming angle was also inferred. The three 300 μm-thick Si strip detectors used to track the particle trajectories [53] have been taken into consideration in the simulation and treated as amorphous Si layers. Channeling deflection efficiency has been computed as in Ref.[41]. Fig. 3.3 shows the simulated deflection efficiency vs the horizontal incoming angle, which has to be compared to Fig. 3 of Ref. [43].

The code has been tested also to reproduce axial channeling. The same Si strip has been proved to deflect particle through axial channeling [123]. Various alignments have been simulated in Fig. 3.4. The simulations and the experimental measurements are in fair agreement. To understand the different behavior of the +40 and +15 μrad position simulations with vertical angle misaligned of 15 μrad have been simulated. The agreement with the misaligned position is better due to the asymmetric distribution measured. Thus, it seems that the alignment was not perfect for such measurements.

3.3.2 Boggsite, a complex atomic structure

In the third simulation the dynamic of a 400 GeV/c proton beam impinging on a 1x1x1 mm^3 boggsite crystal [124] is proposed. Boggsite is a zeolite exhibiting large rings which form channels within which a positively charged particle can be captured. A beam parallel to [100] axis has been considered. The integrated trajectories of ten particles are shown in Fig. 3.5.a. The potential energy of the crystal has been used as background image. In Fig. 3.5.b the integrated horizontal and vertical phase spaces of the trajectories of the ten particles are shown. Particles not impinging on boogsite axes can be trapped within

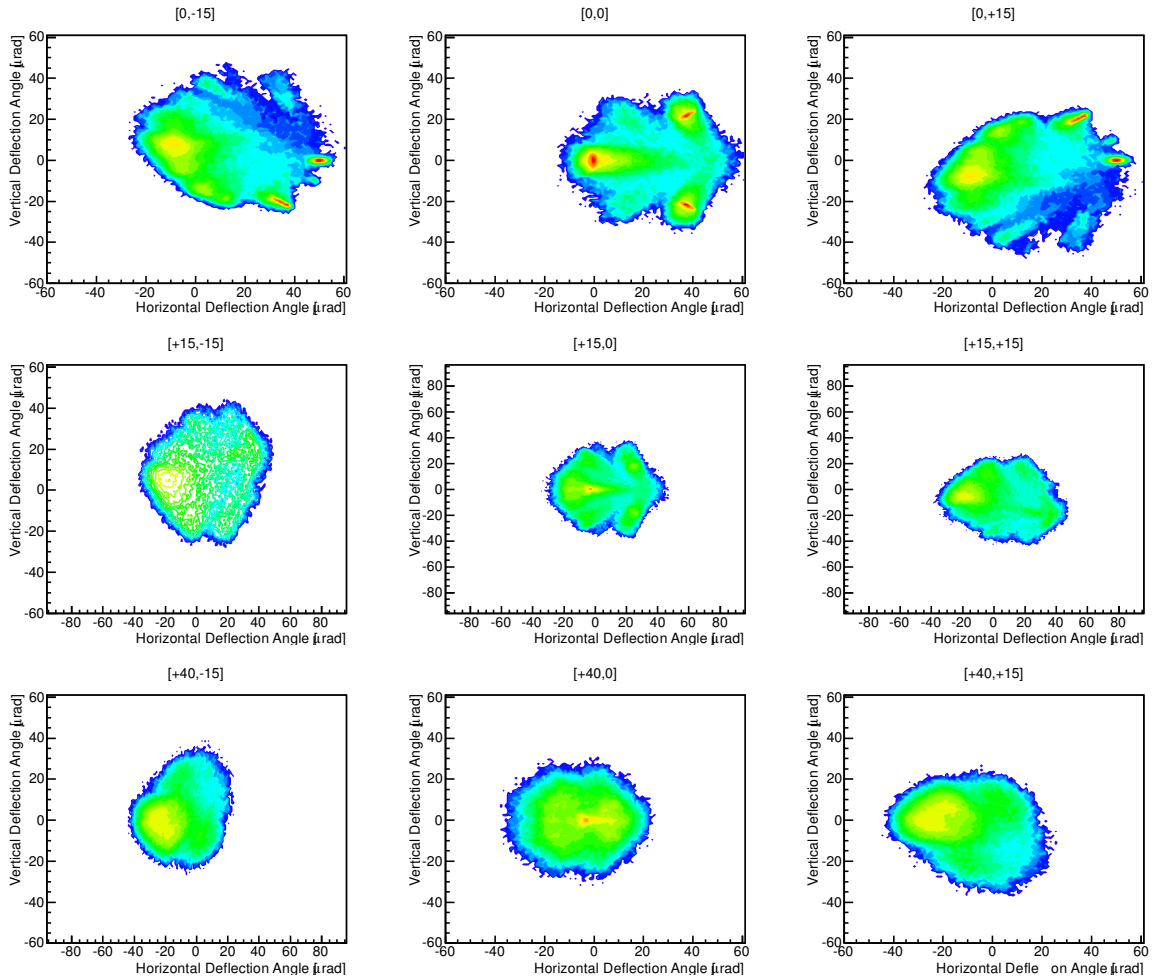

Figure 3.4: Horizontal deflection angle vs. vertical deflection angle for a 400 GeV/c proton beam impinging on a 38 m bent Si strip. The simulations have been done for various incoming angle and a fixed angular range of ± 5 μrad around the central point.

12-ring channels or in small-sized potential well with deeper potential. In fact, particles perform closed orbit with various size in horizontal and vertical phase spaces, depending on their impact parameter on the boggsite surface.

Performance of `DYNECHARM++` toolkit has been measured during simulations. RAM usage was limited to 8MB for the first and second simulations and to 48MB for the last, due to the bigger size of the stored electric characteristics for axial condition. Average computational time per particle scale as crystal length for planar case and is equal to 38 ms per particle for the first simulation. In the case of Boggsite the calculation time per particle was 430 ms per particle.

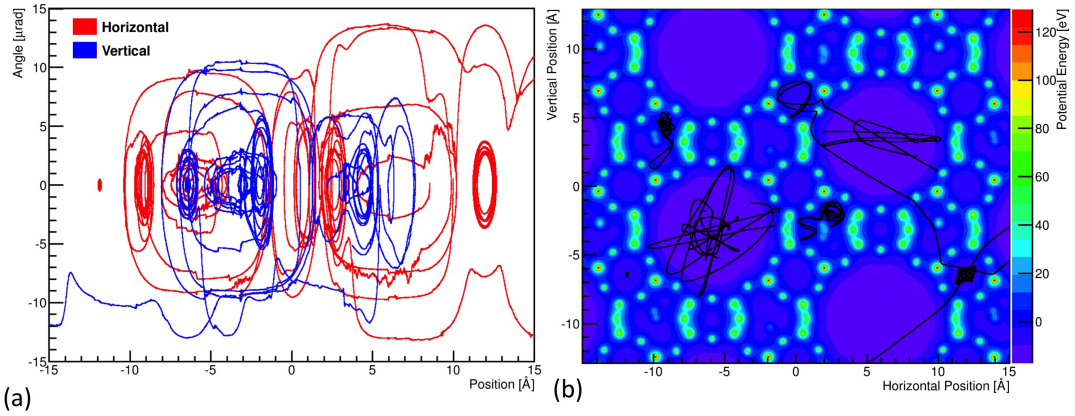

Figure 3.5: Integrated trajectories in real (a) and phase (b) spaces of ten 400 GeV/c protons interacting with a boggsite oriented along [100] axis.

3.3.3 Multiple volume reflection in a multi-crystals object

To test the "black box" code, emulation of a single strip is shown in Fig. 3.6a for comparison with experimental results (see Fig. 6 in Ref. [41]). Emulation shows very good qualitative agreement, as can be seen by comparing the two pictures, and quantitative agreement , by comparing the efficiency and deflection angle of the experiment with the results of the emulation, i.e., (99.3 $\pm$ 0.1) % (13.71 $\pm$ 0.03) μrad respectively. Channeling exhibits the same incoming angular distribution. Dechanneling and volume capture intensities are in very good agreement with experimental data, a validation of the choice of an exponential distribution.

In addition, to test the emulation of multiple crystals, the experimental results obtained with two crystals have been worked out (see Fig. 3.6b and 3.6c and Fig. 2 in Ref. [39] and [125]), obtaining for the double reflection an efficiency of (98.7 $\pm$ 0.1) % and a deflection angle of (25.70 $\pm$ 0.08) μrad. In summary, emulation can manage the reciprocal alignment of a sample composed by more than one crystal and is a suitable method to evaluate MVRMC performance.

3.4 DYNECHARM_Phi

Intel Many Integrated Core (Intel MIC) architecture combines many Intel CPU cores onto a single chip. Intel MIC architecture is targeted for highly parallel, High Performance Computing (HPC) workloads in a variety of fields such as computational physics, chemistry, biology, and financial services. Today such workloads are run as task parallel programs

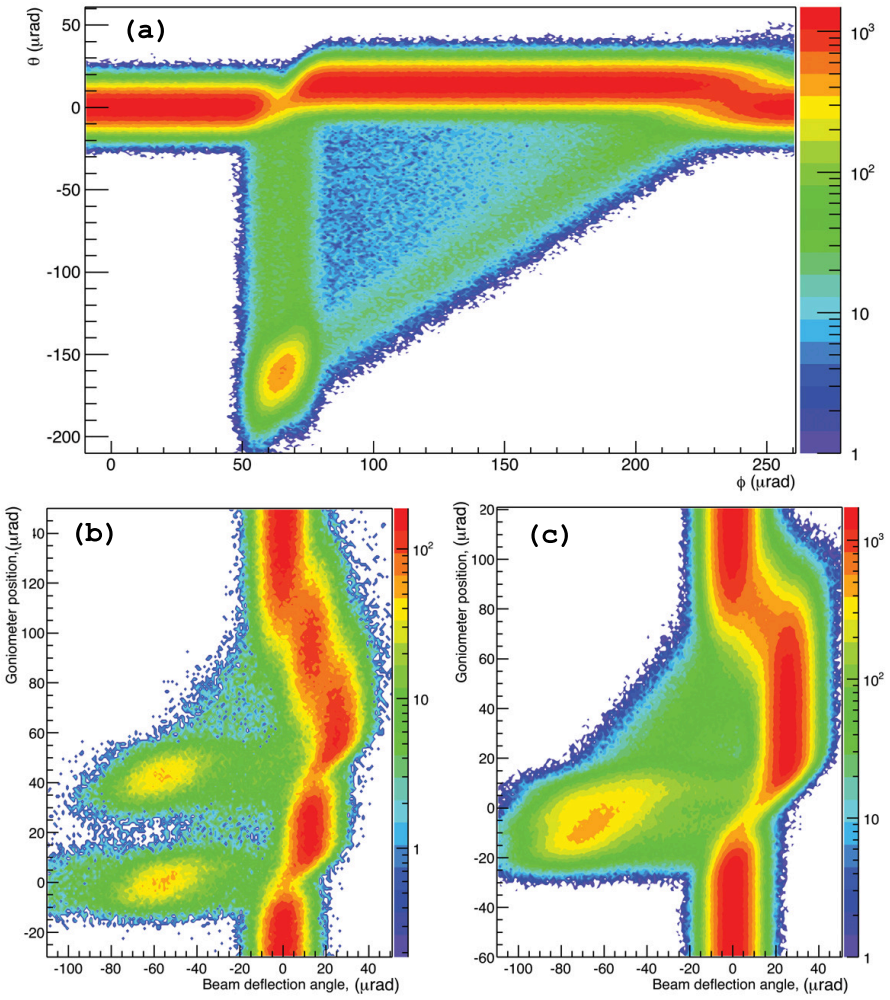

Figure 3.6: (a) Simulated distribution of particles interacting with strip crystal ST4 to be compared with experimental results of Fig. 6 in Ref. [41]. (b) and (c) Simulated distribution of particles interacting with two quasi-mosaic crystals to be compared with experimental results of Fig. 2 (a) and (b) in Ref. [39] and [125]. The case (b) is for two misaligned crystals, the case (c) is when the crystals are aligned to each other.

.

on large compute clusters. The Intel Xeon Phi coprocessor provides high performance, and performance per watt for highly parallel HPC workloads, while not requiring a new programming model, API, language or restrictive memory model. Intel MIC is built to provide a general-purpose programming environment similar to the Intel Xeon processor programming environment. The Intel Xeon Phi coprocessors based on the Intel MIC architecture run a full service Linux operating system, support x86 memory order model

and IEEE 754 floating-point arithmetic, and are capable of running applications written in industry-standard programming languages such as Fortran, C, and C++ [126].

3.4.1 Hyper-Threading and Vectorization

The basis of the Intel MIC architecture is to leverage x86 legacy by creating a x86-compatible multiprocessor architecture that can utilize existing parallelization software tools. Parallelization is extended also through the usage in each core of a short in-order pipeline capable of supporting 4 threads in hardware, i.e. Intel Hyper-Threading Technology (HT). Intel HT Technology allows one physical processor core to present two logical cores to the operating system, which allows it to support two threads at once [127]. HT cannot have performance expectations equivalent to that of multi-processing where all the processor resources are replicated. Measured performance on the Intel Xeon processor with HT shows performance gains of up to 30% on common server application benchmarks for this technology [128]. There are several dependencies reflected in the speedup demonstrated by any benchmark with Hyper-Threading Technology, and the amount of gain can vary widely. However, a gain of 30% or more within a parallel section with is considered acceptable [129].

An important component of the Intel Xeon Phi coprocessors core is its vector processing unit (VPU). The VPU features a novel 512-bit Single Instruction Multiple Data SIMD instruction set, officially known as Intel Initial Many Core Instructions (Intel IMCI). Thus, the VPU can execute 16 single-precision (SP) or 8 double-precision (DP) operations per cycle. The VPU also supports Fused Multiply-Add (FMA) instructions and hence can execute 32 SP or 16 DP floating point operations per cycle. It also provides support for integers. Vector units are very power efficient for HPC workloads. A single operation can encode a great deal of work and does not incur energy costs associated with fetching, decoding, and retiring many instructions.

Serial codes (i.e., running with a single thread), as well as instruction-parallel calculations (running with several threads) can take advantage of SIMD instructions and significantly increase the performance of some computations. Each CPU core performs SIMD operations on several numbers (integers, single or double precision floating-point numbers) simultaneously, when these variables are loaded into the processors vector registers, and a vector instruction is applied to them. SIMD instructions include common arithmetic operations (addition, subtraction, multiplication and division), as well as comparisons, reduction and bit-masked operations (see, e.g., the list of SSE 2 intrinsics). Libraries such as the Intel Math Library provide SIMD implementations of common transcendental

functions, and other libraries provide vectorized higher-level operations for linear algebra, signal analysis, statistics.

SIMD instructions can be illustrated with the following pseudocode [130]:

```
for (i=0; i<n; i++) // SCALAR LOOP
A[i] = A[i]+B[i]; // SCALAR LOOP

for (i=0; i<n; i+=4) // SIMD LOOP
A[i:(i+4)]=A[i:(i+4)]+B[i:(i+4)]; // SIMD LOOP
```

The SIMD loop above performs one quarter of the total number of iterations of the regular loop. Each addition operator acts on 4 numbers at a time. Such operations can be called by the code via the respective intrinsic function, representing a SIMD addition operator.

There are several practical ways to incorporate vector instructions into a calculation. The most straightforward way is to use highly optimized mathematical libraries with vector instruction support. However, when the algorithm cannot be made by standard mathematical operations available in libraries, the programmer has to implement vector operations in custom ways.

Most modern compilers are able to auto-vectorize regular C, C++ or Fortran code. Auto-vectorization has tremendous advantages over explicit calls to SIMD intrinsics. In fact, no vectorized code has to be written. In addition, the code remains forwards-compatible with future generations of CPUs and SIMD instruction sets, since no modification to the source code has to be made.

3.4.2 Code changes

The `DYNECHARM++` has been updated to implement vectorization and has been tested with an Intel Xeon Phi coprocessor.

In order to exploit vectorization, major changes have to be done to the core of the code. In such point, the object-oriented structure has to be broken. In fact, the array of structure (AoS), i.e., a collection of element, has to be replaced by structure of arrays (SoA), i.e., elements in array. While AoS organization is excellent for encapsulation it can be poor for use of vector processing. Selecting appropriate data structures can also make vectorization of the resulting code more effective [131]. To illustrate this point, compare the AoS arrangement for storing the coordinates set of three-dimensional points with the alternative SoA arrangement for storing this set.

```
struct Position{ //AoS
float x;
float y;
float z;
}

struct Position{ //SoA
float* x;
float* y;
float* z;
}
```

The storage in memory is shown in Figs.3.7.(a) and .(b) for the AoS and the SoA structures, respectively. For each operation a block of contiguous memory can be passed to the VPU instead of a single memory slot. A vector of three-vectors, i.e., an AoS, is not efficient, because mathematical operations use one component for each cycle. On the contrary, three vectors containing the components of many particles can be adopted to exploit the SIMD instruction sets.

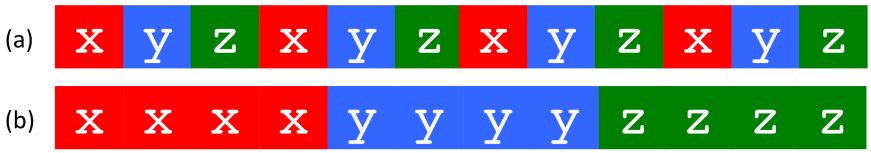

Figure 3.7: Schematic view of the SoA vs. AoS for the storing of the coordinates set of three-dimensional points.

Because the most computationally expensive part of the code is the integration of the particle trajectories, modifications are limited to such portion. Thus, the standard code is used to compute the crystal electrical characteristics and the multiple scattering coefficients. The electrical characteristics are stored in arrays of fixed dimensions. Then such values are adopted in the following integration.

Such modification of the basic structures for the computation of the integrations allows to vectorizing the core of the `DYNECHARM_Phi` code. The Velocity-Verlet algorithm adopted for the integration of particle trajectory only needs simple functions, i.e., sum, multiplication and division.

In addition, the main functions are already vectorized by adopting the Intel Compiler [131], such as `sin`, `cos` and `exp` functions. However, the addition of the multiple scattering

to the calculation slows down significantly the code. Indeed, the multiple scattering takes approximately $\sim$ 83% of the total workload of the CPUs. Such high value is justified because of the need of computationally expensive functions for the generation of random number distributed according to a Gaussian function. The bottleneck is the standard random number generator which can not process an array. Thus, vectorization can not be applied. To enhance the performance the Box-Muller algorithm has been used.

3.4.3 Preliminary results

The code has been tested with Intel Xeon Phi Coprocessor. We are grateful to Colfax International Ltd. for the possibility to use one of their server for the test. The machine was equipped with two Intel Xeon CPU E5-2680 @ 2.70GHz processors and two Intel Xeon Phi Coprocessors 5110P @ 1.053 GHz with 60 cores and 8GB of memory onboard.

First, the code scalability has been tested. The code has been parallelized at thread level with OPENMP [108]. The total computation time for the same configuration has been used. The performance has been measured in a fully parallel region. Results of speedup are reported in Tab. 3.1 and shown in Fig. 3.8. The speedup is

$$speedup = \frac{t_1}{t_n} \tag{3.19}$$

where t_1 is the computation time for one thread ad t_n the same with n-threads.

The code scalability is very good until the physical cores of the coprocessor are present. Then, the code is capable to enhance the performance but not to maintain the same slope for the reduction of computation time. Indeed, the cores exploit Hyper-Threading which allows the core to queue four operations and process them in sequence but not simultaneously. Thus, the computation time grows and the performance is slightly reduced. The slope for the four stages are 0.99 for the physical cores, 0.47 for the second processed operation with the HT from 60 to 120 cores, 0.23 for third from 120 to 180 cores and 0.15 for the fourth from 180 to 240 cores. Thus, a speed-up of 99% has been registered for the physical cores. In addition, HT allows to sensibly improve performance up to 47% for the first cycle to 23% and 15% for the second and third cycles, respectively.

The second test regards the capability to exploit vectorization. The same code has been compiled with and without the appropriate flag to enable auto-vectorization of the code. Results of computation times are reported in Tab. 3.2 and shown in Fig. 3.9. The average speed-up of 4.49 is registered by only enabling auto-vectorization of the code. Thus, the code exploit vectorization but not completely. The speed-up for a perfectly vectorized code

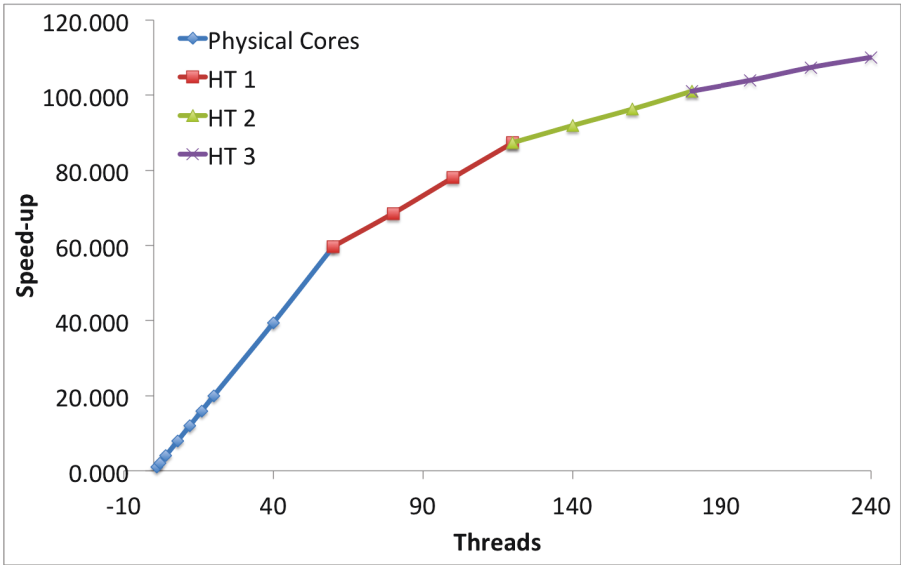

Figure 3.8: Speed-up on one thread as a function of the number of cores for the optimized version of DYNECHARM++ running on the Intel Xeon Phi.

Table 3.1: Speedup on one thread as a function of the number of cores for the optimized version of DYNECHARM++ running on the Intel Xeon Phi.

Core Number	Speedup on one thread	Core Number	Speedup on one thread
1	1.000	80	68.530
2	2.000	100	78.026
4	3.998	120	87.322
8	7.991	140	91.908
12	11.967	160	96.295
16	15.950	180	101.073
20	19.922	200	103.990
40	39.437	220	107.394
60	59.708	240	110.090

can reach up to 8.00, thanks to the wide 512-bit register. In fact, the register can store and process at the same time up to 8 double precision floating point (64-bit).

Lastly, the code has been tested both with the Intel Xeon Phi and the Intel Xeon processors. The results has been compared to highlight the range of usage of the Phi card. Indeed, as shown in Fig. 3.10, the Xeon Phi coprocessor beats the Xeon Phi processor for a large number of particles, while it is slower when the total number of particles processed is small. Such behavior happens because of the dynamical distribution of the workloads

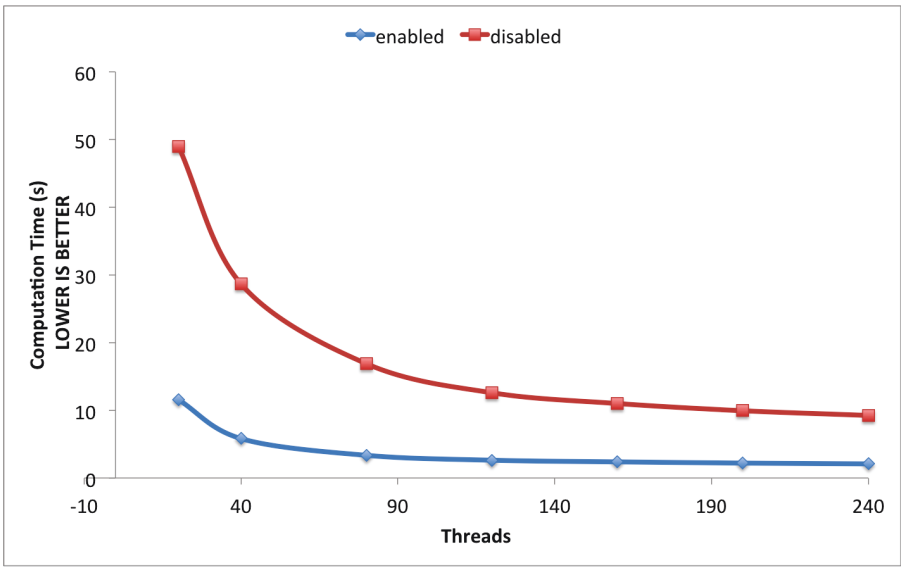

Figure 3.9: Computation time with and without auto-vectorization enabled as a function of the number of cores for the optimized version of `DYNECHARM++` running on the Intel Xeon Phi.

Table 3.2: Computation time with and without auto-vectorization (Vec) enabled as a function of the number of cores for the optimized version of `DYNECHARM++` running on the Intel Xeon Phi.

Core Number	Vec Enabled	Vec Disabled	Core Number	Vec Enabled	Vec Disabled
20	11.523	48.982	160	2.38392	11.0014
40	5.82097	28.6638	200	2.20751	9.93763
80	3.34974	16.8768	240	2.0852	9.24374
120	2.62889	12.5913			

between the threads. Because the cores are 240 for the Xeon Phi, if the computation of the trajectory of a single particle takes longer than others, it is not a bottleneck for all the computations, thanks to the large number of cores. Thus, the greater the number of particles, the more efficient the distribution between the threads. In Tab. 3.3 the results of the comparison are shown.

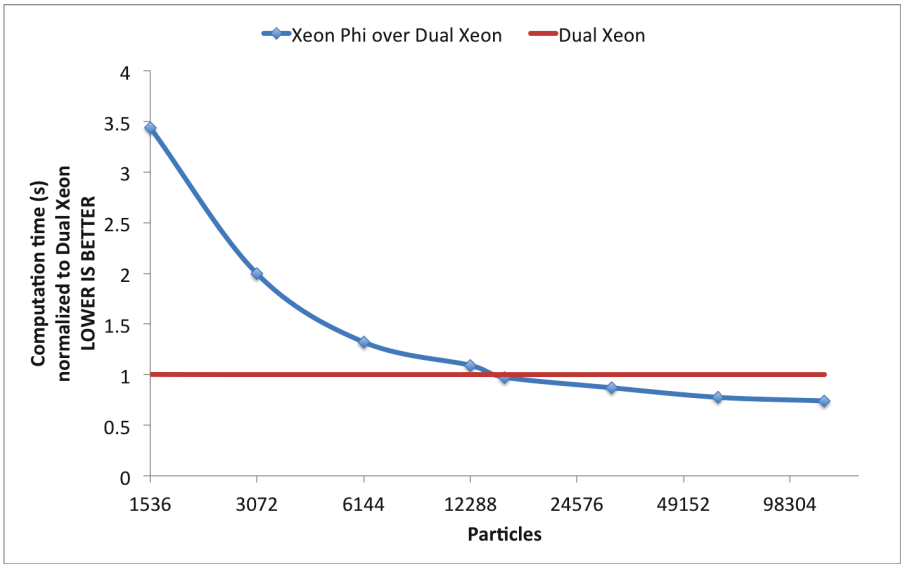

Figure 3.10: Computation time of Xeon Phi over computation time of Dual Xeon as a function of the total number of particles processed for the optimized version of `DYNECHARM++`.

Table 3.3: Computation time of Xeon Phi over computation time of Dual Xeon as a function of the total number of particles processed for the optimized version of `DYNECHARM++`.

Number of particles	Xeon Phi over Dual Xeon	Number of particles	Xeon Phi over Dual Xeon
1536	3.436	15360	0.973
3072	1.996	30720	0.870
6144	1.321	61440	0.775
12288	1.091	122880	0.740

Chapter 4

Channeling model for Geant4

Monte Carlo simulation of interaction of particle with matter is usually made with downloadable toolkit as Geant4 [132] and Fluka [56]. Such Monte Carlo codes are continuously expanded and improved thanks to the concurrent work of scientists from all over the world. Geant4, an object-oriented toolkit, has had a large expansion of the users' community in the last years. As an example, applications simulated by Geant4 range from particle transportation in ATLAS detector [133] to calculation of the dose distribution curves for a typical proton therapy beam line [134], from radiation analysis for space instruments [135] to early biological damages induced by ionizing radiation at the DNA scale [136].

In November 2012 a version of Geant4 with the first implementation of a physical process in a crystal was released. In fact, an extension has been developed to manage properties of periodic structures in Geant4. The process of the phonon propagation within Ge crystal has been added to the toolkit, but no orientational effects for charged particles has been developed. A physical model implemented into Geant4 requires a description of the interaction length of the process involved. Thus, the cross-section of the process has to be known or computed to developed an extension of the toolkit. In addition, the concurrent presence of many physical processes force to use an integration step greater than a μm to limit the computational time. As a result, the full solution of the equation of motion is not suitable and a model based on experimental data restrict the possible expansion to already proved initial condition. Thus, a suitable model lacks at the moment for Geant4.

A general model for simulation of orientational effects in straight and bent crystal for high-energy charged particles is presented. The model is based on continuous potential approximation but does not rely on the full integration of particle motion. Implementation into Geant4 and comparison with experimental data have been worked out. Since the

models for channeling and volume reflection are based on the continuous potential approximation, a resume of the Lindhard work and its applicability range are presented in the following.

The model has been developed in collaboration with the Geant4 team of SLAC National Accelerator Laboratories during a five months visiting period.

4.1 Models for orientational effects

4.1.1 Channeling

When a charged particle hits a crystal aligned with an atomic plane it can be trapped by the strong electromagnetic field between by two planes, i.e., it undergoes planar channeling. Channeled particles follow the direction of crystal plane oscillating between or on planes if particle charge is positive or negative, as shown in Fig. 4.1.a. Positive particles penetrate deeper into the crystal under channeling condition with respect to not aligned orientation because the trajectory is forced to swing far from the nuclei. On the contrary, negative particles interact more frequently because of the attraction in the zone of high-density due to the nuclei.

Continuous interplanar potential for main planes in crystals [57] can be approximately described by an harmonic potential well for positive particles, as shown in Fig. 4.1.c. On the contrary, since negative particles are attracted by nuclei, interplanar potential has to be reversed and becomes non-harmonic with a discontinuity point in the middle of the potential well, as shown in Fig. 4.1.d. Because the trajectory is strongly affected by such interplanar potential, positive and negative particles under channeling draw different shapes in phase space (see Fig. 4.1.b).

Channeling holds for particles with transverse energy $E_{x,\theta}$ lower than the maximum of the potential well depth U_0, i.e., $E_{x,\theta} < U_0$. Such particles follow channeling plane or axes until they exit the crystal or are dechanneled. Dechanneling mechanism behaves the same for both straight and bent crystals. If all the processes which lead to dechanneling are disabled by contradiction, a particle remains under channeling for the whole crystal length if $E_{x_{in},,\theta_{in}} < U_0$, where x_{in} and θ_{in} are impact position and incoming angle with respect to channeling plane. Thus, conservation of transverse energy allows treating channeling through knowledge of initial impact position on crystal channel x_{in} and angle with respect to crystal plane θ_{in}.

$$E_{x_{in},\theta_{in}} = U(x_{in}) + \frac{1}{2} p\beta {\theta_{in}}^2 \tag{4.1}$$

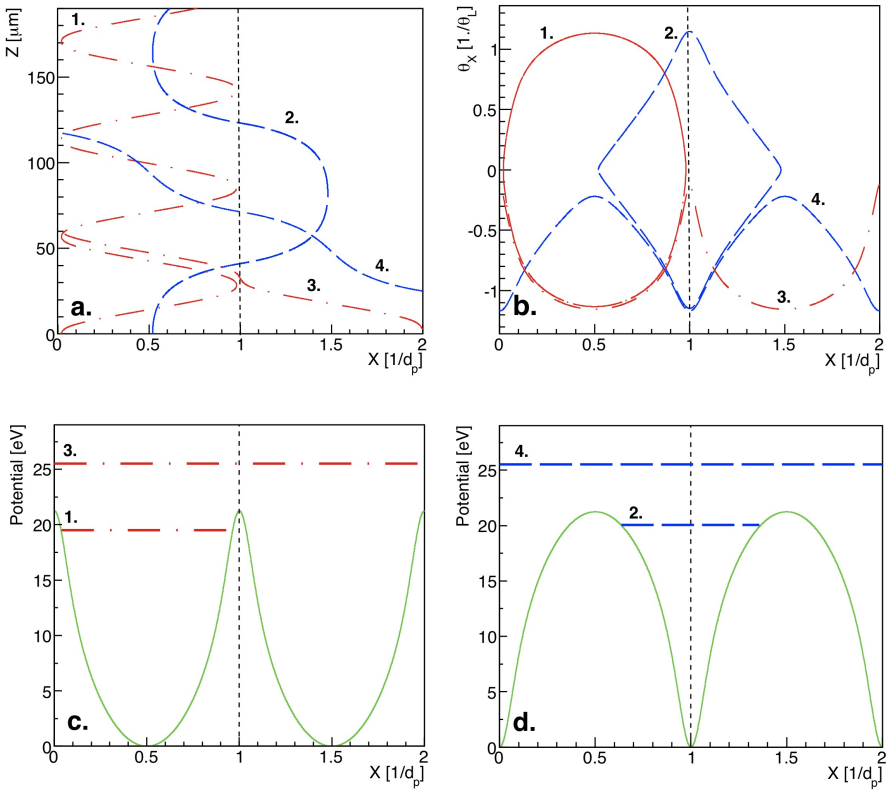

Figure 4.1: Channeled (1. and 2.) and over-barrier (3. and 4.) 400 GeV/c positive (dot-dashed line) and negative (dashed line) particles interacting with Si (110) planes (dotted lines). (a) Trajectories as a function of transverse position (X) and penetration depth (Z). (b) Trajectories as a function of transverse position (X) and transverse angle (θ_X). (c) and (d) Continuous planar potential (continuous line) and transverse energies.

Solution of the equation of motion requires the knowledge of transverse position and transverse momentum of a oscillating particle point by point. However, by choosing a crystal with length along the beam larger than one oscillation period for a channeled particle, the energy level occupied by a particle in the electrostatic potential well, generated between atomic planes or axes, is the only physical quantity to link initial to final parameters in a real-case study. By imposing a continuous and uniform distribution in position x_{out} for a channeled particle of energy E_t, an outgoing angle θ_{out} is generated by evaluating

$$\theta_{out} = \sqrt{2p\beta(E_t - U(x_{out}))} \tag{4.2}$$

Therefore, information regarding x_{in} and θ_{in} can be condensed into the sole variable E_t, which determines the occupied energy level of a channeled particle and allows to compute outgoing distribution of channeled particles by means of E_t and continuous potential.

For bent crystals the model is still valid. The sole difference relies in the modified potential in the non-inertial reference frame orthogonal to the crystal plane or axis. In fact, the centrifugal force acting on the particle in this frame pulls down potential barrier resulting in a lower potential well depth. Thus, condition for channeling holds with a modified maximum potential and transverse energy related to the non-inertial reference system.

4.1.2 Dechanneling and volume capture

Channeled particles which leave the channeling condition have suffered dechanneling. Not channeled particles which enter channeling state undergo volume capture. Dechanneling and volume capture take place when particles interact incoherently with nuclei or electrons. In deed, a channeled particle can acquire enough transverse energy to leave the channeling state by exceeding the maximum of the potential well or a not channeled particle can lose energy and decrease the transverse energy passing under the maximum of the potential well.

All physical phenomena occurring for a channeled particle are strongly affected by the occupied energy level. As shown in Fig. 4.3, the average density of material, seen by a particle traversing a crystal aligned with its planes, is strongly affected by the transverse energy of the particle. Thus, the probabilities of interaction with nuclei and electron have to be weighted as a function of the transverse energy. Kitagawa and Ohtsuki [81] demonstrated that the dependence of incoherent interaction rate by the material density scales linearly with the ratio of the density seen by the particle. Therefore, the modified cross section $\sigma(E_t)$ of each phenomenon holds

$$\sigma(E_t) = \sigma_{am}\frac{n(E_t)}{n_{am}} \tag{4.3}$$

where σ_{am} is the cross section in amorphous material, n_{am} is the density of the amorphous material and $n(E_t)$ is the modified density.

Since each incoherent phenomenon produces a variation of transverse energy ΔE_t, the maximum distance traveled by a channeled particle has to be limited by the probability to overcome or to under passing the potential barrier during each step. As an example, modified rms $\sigma_{is}(E_t)$ for incoherent scattering on nuclei depends approximately on the square root of the crossed material [137]. Thus, the step can be limited by the condition

$$|U_0 - E_t| = |\Delta E| = \Delta\left(p\beta\theta^2\right) \approx p\beta\frac{n(E_t)}{n_{am}}\Delta\left(\sigma^2_{is,am}\right) \tag{4.4}$$

where $\sigma_{is,am} \sim \frac{E_s}{p\beta}\sqrt{\frac{z}{X_0}}$ is the rms of incoherent scattering in the amorphous material, $E_s = 13.6$ MeV, β is the particle velocity in unit of the speed of light and X_0 is the radiation length for the material. Thus, the step Δz holds

$$\Delta z \sim X_0 \frac{p\beta}{E_s^2} \frac{n_{am}}{n(E_t)} |\Delta E| \tag{4.5}$$

Such approach can be applied to all the concurrent incoherent processes to determine the maximum step by comparing the contributions. The model is still valid for positive and negative particles since no restriction has been applied.

By averaging the density over an oscillation period the same response for the interaction probability can not be obtained. Therefore, this model has to be adopted for crystal with length along the beam higher than one oscillation period. On the contrary, by integrating the particle trajectory is possible to determine the interaction probability for each step depending on the position in the channel. Thus, peculiar characteristics of channeling in first layers of a crystal are lost by the average.

4.1.3 Volume reflection

When charged particles cross a bent crystal tangent to its planes they are "reflected" in the direction opposite to that of the bending curvature, i.e., they suffer the so-called volume reflection. In fact, particle is rejected by the continuous potential barrier of one plane, but immediately leaves the channel because the barrier of the opposite plane is lowered due to the bending and thus it can not keep particle under channeling state. Therefore, the condition for volume reflection holds when the particle projection on the direction of a plane change the signs. Volume reflection and related phenomena limit the maximum allowed step length. Indeed, particles can be captured into a channeling state if they lose enough transverse energy to fulfill the channeling condition $E_x < U_0$. Thus, the step has to be comparable to the oscillation period near the turning point. The distance of a particle to the tangency point in a bent crystal has to be evaluated at each step to size the step in the proximity of the interesting region.

For a slightly bent crystal, the mean deflection angle for volume reflection holds approximately $\sim 1.4\theta_L$ for positive particle [38] and $\sim 0.8\theta_L$ for negative [88], where $\theta_L = (2U_0 p\beta)^{1/2}$ is the Lindhard angle [30]. In fact, a positive particle spends more time in a zone with high transverse velocity, while negative particle do the opposite, as shown in Fig 4.2.a. By decreasing the radius of curvature, mean deflection angle decreases. Indeed deflection angle of volume reflection depends on the transverse energy at the turning point.

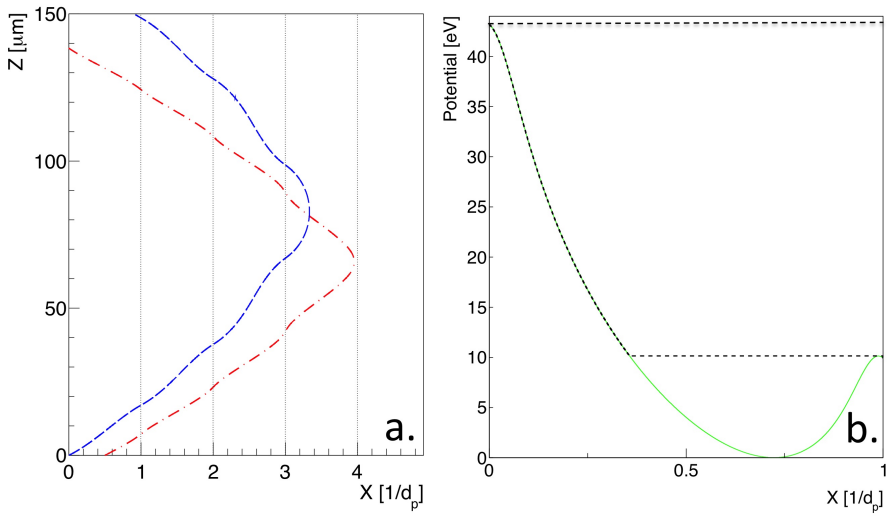

Figure 4.2: (a) Simulation of volume reflection for positive (dot-dashed line) and negative (dashed line) particles with the same initial transverse energy in the non-inertial reference frame orthogonal to the crystal plane. Dotted lines are crystal planes. Due to higher momentum of positive particle near the turning point, deflection angle of volume reflection results higher. (a) Continuous planar potential in the non-inertial reference frame orthogonal to the Si (110) plane for $p\beta/R = 17.3eV/\text{Å}$. Dotted lines delimit region of volume reflection.

The more the crystal is bent the larger the angular spread [38]. In Fig. 4.2.b the potential in the non-inertial reference frame orthogonal to the crystal plane is shown. The maximum energy difference delimits the reflection region. Potential shapes the trajectories of particles with transverse energy a bit higher than the maximum of the potential, the so-called over-barrier particles. By approximating the potential in the reflection region with a linear function, the volume reflection angle is proportional to the position of the turning point. Thus, deflection angle can be generated by adopting a continuous and uniform distribution proportionally to the reflection region.

4.1.4 Average density

The average density seen by a particle undergoing orientiational effect is a very important parameter for the model proposed in this thesis. As shown in Fig. 4.3, the average density is strongly affected by transverse energy for channeled and over-barrier particles. Computation is made with the DYNECHARM++ code [138] disabling all the incoherent process. The DYNECHARM++ code is based on the full solution of the equation of motion in the continuous potential and allows to compute the electric characteristics of

the crystal through the ECHARM calculation method [79, 110]. Therefore, density as a function of transverse energy for complex atomic structures and for many planes and axes can be computed.

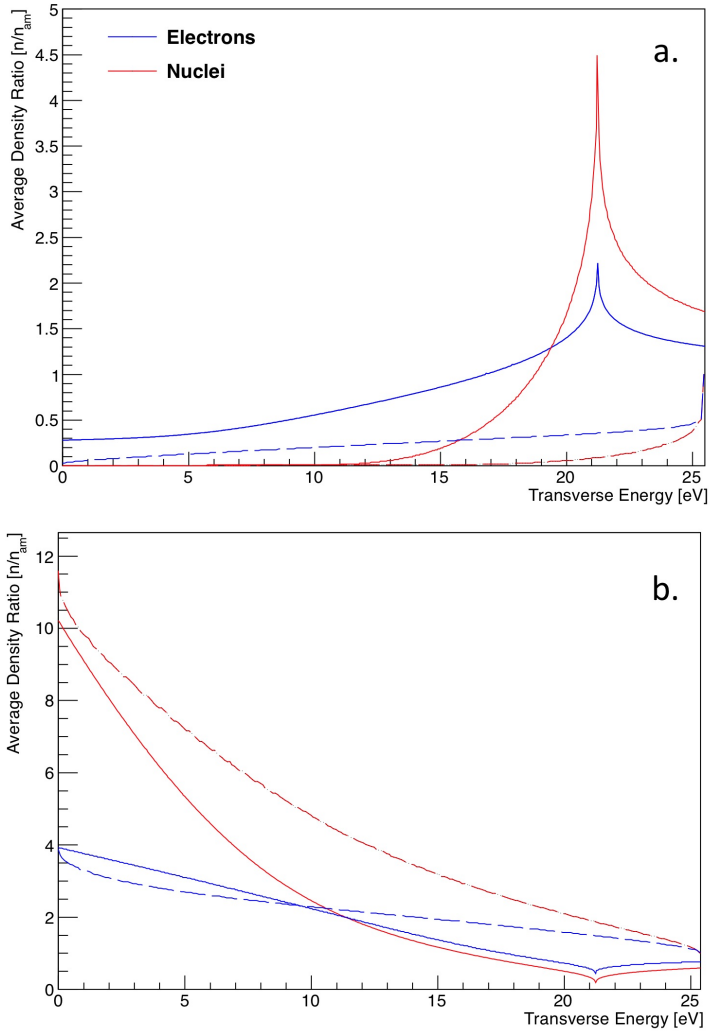

Figure 4.3: (a) Ratio of average density of nuclei and electron over density for an amorphous material as a function of the transverse energy of a positive channeled particle computed with DYNECHARM++ (continuous lines) and with fast model (dashed lines). Over-barrier particles experience higher density as a result of the different motion in the crystal lattice. (b) Ratio of a negative channeled particle. To be noted different scales for vertical axes.

Calculation of the average density through DYNECHARM++ is very accurate, but, at the same time, can be very slow. Thus, a fast version has been developed to compute average density. By integrating density of all the possible state in which a particle with

transverse energy E_t may lie, an approximated expression for the average density $\overline{\rho}(E_t)$ can be computed.

$$\overline{\rho}(E_t) = \int_{U(x)<E_t} \rho(x)dx \tag{4.6}$$

Since no approximation has been imposed to $U(x)$ and $\rho(x)$, such approximation is still valid for any potential and average density functions. Experiments with orientational effects rely mostly on the usage of crystal planes with low Miller indexes. For them, averaged nuclei density $\overline{\rho}(x)$ has been analytically derived starting by the nuclei density function averaged over thermal and space fluctuations

$$\rho(x) = \frac{1}{u_T\sqrt{2\pi}} e^{-\frac{x^2}{2u_T^2}} \tag{4.7}$$

where u_t is thermal vibration amplitude. Thus, the average density holds

$$\overline{\rho}(E_t) = \mathrm{erf}(x|U(x) = E_t) + 1 \tag{4.8}$$

where $E_t \leq U_0$ and $U(x) = U_0$ at $x = d_p/2$. Such fast calculation model can not take into consideration the time spent in a particular region by particle. The model can be applied to compute the density for both positive and negative particles. In Fig. 4.3 the average density ratio of electrons and nuclei is shown for both the fast model and DYNECHARM++.

4.2 Geant4 implementation

Geant4 toolkit allows adding a physical process by describing its mean interaction length and how particle properties are affected after the interaction. The model proposed in this paper has been implemented through a class for the description of orientetional process and wrapper classes to modify the density in existing processes. In addition, classes for fast calculation of crystal characteristics have been developed to allow simulating orientational processes with no need for external softwares. The class used for implementation of orientational processes is `G4VDiscreteProcess`. Processes are forced to be called at each step to check the presence of a crystal lattice, since they can always modify particle trajectory and cross-sections of other physical processes. When a particle cross a boundary between two geometrical volumes, one without and one with a lattice, i.e., to which a XV-LogicalLattice class has been assigned, condition for orientational processes are evaluated

and step of particle is limited consequently.

At first the step into a crystal, the impact position of the particle in the channel is generated following a continuous uniform distribution. Thus, the initial transverse energy is computed. When a particle is under channeling, the process proposes to turn the particle momentum $\bar{p}$ parallel to direction of crystal plane $\hat{n}$. In the following steps, the transverse energy can be modified by concurrent Geant4 processes such as incoherent scattering on nuclei and electrons. Since channeled particle has $\bar{p}$ parallel to $\hat{n}$, only non orientational processes would result in dechanneling. Volume reflection implementation strictly follows the rule described in the model section. In fact, the particle undergoes volume reflection when the projection of $\bar{p}$ on $\hat{n}$ changes sign. This is possible only for bent crystal and for particles whose trajectories is tangent to $\hat{n}$ in a point.

At each step the average densities of nuclei and electrons are recomputed as a function of transverse energy. Modified average density of the material is used by specific wrapper classes, allowing computation of modified cross-section of existing processes and preserving code reusability for future release of Geant4. In particular, G4VDiscreteProcess and G4VEnergyLoss classes have been wrapped. The interaction length of discrete processes is resized proportionally to the average density ratio. Crossed length for continuous energy loss processes is also resized proportionally to average density, because cross-section depends on unit distance along the path, i.e., density multiplied by crossed length.

The presence of torsion in a crystal spoils channeling efficiency in bent crystals [22]. In deed, orientation of channeling angle with respect to beam direction changes with the impact position on the crystal surface. Since a beam has a finite size, two particles with the same direction and the same impact position on the potential well but different impact position on the crystal surface have different transverse energy. Such effect has been introduced in the simulation by changing the plane direction with respect to the impact position on the crystal surface.

Another important parameter for channeling in bent crystal is the miscut [139], i.e., the angle between the lateral surface of a crystal and the atomic planes. Only the trajectories of particles channeled near a crystal edge are touched by the presence of the miscut, because it modifies the total length of the bent plane of channeling. The effect has been introduced by defining the plane orientation independently of the crystal volume.

4.3 Examples of calculations

Firstly, the Geant4 code has been compared to the DYNECHARM++ code in order to evaluate its advantages of the approach in term of computation. Same initial conditions have been used as in Ref. [138], i.e. a 400 GeV/c proton beam interacting with a 1.94 mm thick (1 1 0) Si bent crystal with a 38 m curvature radius. The Geant4 single thread version 10.00b has been adopted and only discrete single scattering model has been added to the list of physics processes. The computer was the same used for DYNECHARM++ test, i.e. a standard personal computer with 8 GB of RAM and Intel(R) Core(TM) i7-2600K CPU running at 3.40GHz. Computation time has taken approximately 14 ms per particle in Geant4 vs. the 38 ms per particle in DYNECHARM++, in spite of the higher complexity of the Geant4 code. Such result is explained by considering the number of step needed for by the first and the second models adopted for the simulation. Full integration of trajectories requires step much lower than the oscillation period in the potential well.

4.3.1 Channeling

Model validation has been worked through comparison with already published experimental data. Experiments regard efficiency of channeling vs. incoming angle [43], rate of inelastic nuclear interaction under channeling [13]. Such comparisons allow one to check both precision of the model and quality of Geant4 implementation, especially regarding wrapped processes for physical processes other than channeling.

The bent crystal has been modeled as a small fraction of a toroid with a given bending radius and length along the beam direction with sizes exactly equal to the real ones. Though torsion and miscut can be simulated, they have not been considered. In deed experimental data have been corrected for torsion and the miscut value has no influence for the particles impinging far from crystal edges. Three silicon detectors to track the trajectories of the particles have been inserted in the simulation. For the measurement of the rate of inelastic nuclear interaction, two scintillators have been added to reproduce the experimental setup of Ref. [13]. To speed up simulation, volumes other than crystal and detectors have been filled with galactic vacuum (`G4_Galactic` material).

In Fig.4.4, the channeling efficiency as a function of incoming angle is found to superimpose experimental results (Fig. 3 of Ref. [43]) and Monte Carlo simulation with complete integration of the trajectories. Maximum efficiency for channeling in Geant4 is in good agreement with experimental data as well as efficiency in the tails. However, a fair agreement is obtained between maximum efficiency and tail, with some 5% deviation in

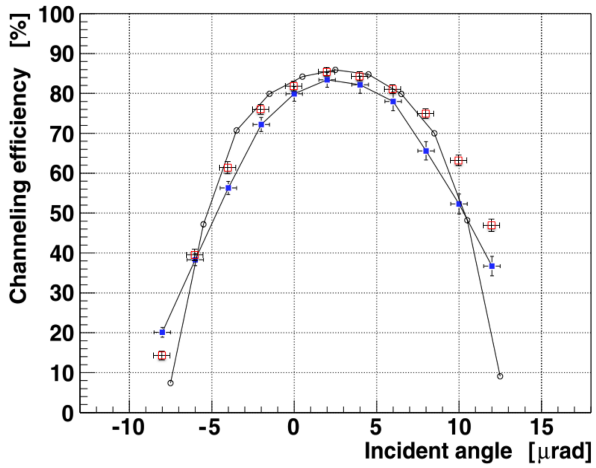

Figure 4.4: Deflection efficiency for a narrow beam fraction as a function of the incoming beam direction with respect to plane direction of a (110) Si bent crystal. Empty squares are results of Geant4 simulation with the model described in the paper, filled squares are experimental measurements and circles are simulation with complete integration of particle trajectory. The figure is partially a reproduction of Fig. 3 of Ref. [43].

efficiency is observed. In this region the model lacks of accuracy because the trajectories were not completely integrated. Thus, such behavior is to be ascribed to the shape of interplanar potential used in simulation for both the models.

4.3.2 Density modification

Fig. 4.5 has to be compared with Fig. 5 of Ref. [13]. The rate of secondary particles is shown as normalized to the amorphous condition . Standard Geant4 release without channeling extension has been used for simulation of amorphous Si and of no crystal. Simulations are in agreement with experimental data. The channeling extension allows correct modification of the cross-sections of incoherent phenomena, reducing the rate with respect to amorphous case.

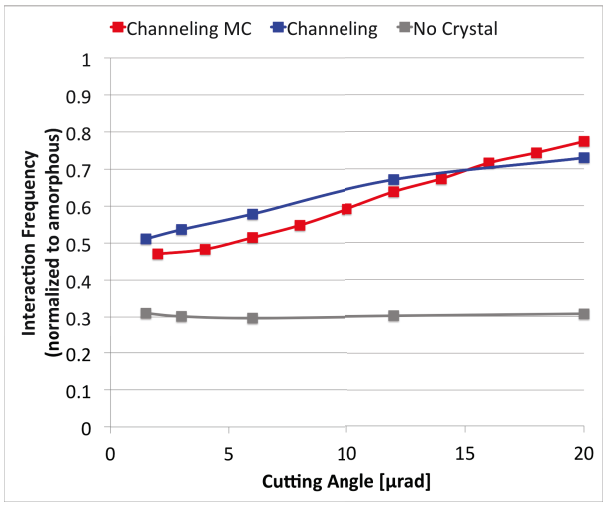

Figure 4.5: Dependence of inelastic nuclear interaction rate of protons on cutting angle of a 400 GeV/c incident proton beam channeling (blue line) and Monte Carlo simulation (red line) and for no crystal along the beam (gray line), i.e. experimental background. Experimental data have been taken from Fig.5 of Ref. [13].

Chapter 5

Experimental measurements

5.1 Multi Volume Reflection in Multi-Crystals

Multiple volume reflection in a multi-crystal (MVRMC) has been recognized as an efficient method to steer high-energy particle beams for beam extraction or collimation. Deflection efficiency of MVRMC is conditional to precision of mutual alignment of the crystals in the multi-crystal. Initial experiments with multi-crystal [40, 46] made use of time-consuming on-beam operations to align individual crystal with a precision of tens of μrad. In Summer 2010 experiments have been performed [50] to test the efficiency of topologically connected multistrip crystal (TCMC) [46]. TCMC is a static system for reciprocal alignment of a sequence of strip-like crystals (Fig. 5.1), whose peculiar geometry allows static control of mutual alignment and curvature of all the strips. As a consequence, TCMC can be set up and fully characterized out-beam to save beam time and enhance the precision of the alignment.

TCMC is fabricated through chemical etching of a (110) Si 4" wafer. It consists of sixteen 1-mm-thick strips spaced by 1 mm with the edges shared in a common frame. The frame is clamped between stainless steel gauges to cause anticlastic deformation of the strips [140]. A complete description of the bending device is in Ref. [141]. Primary crystal bending is achieved by clamping the frame between flat stainless steel gauges. All the materials used for fabrication of the bending device are ultra-high vacuum compatible. Proper alignment of the strips is achieved by fine adjustment of a series of screws on the holder to impress uniform pressure. Each step is monitored through a white-light interferometer (VEECO NT-1100). A more detailed description of the TCMC is in Ref. [50]. On-beam experiments has been performed H8 line with the experimental apparatus described in Ref. [38]. It allows detecting particle tracks with an angular resolution less

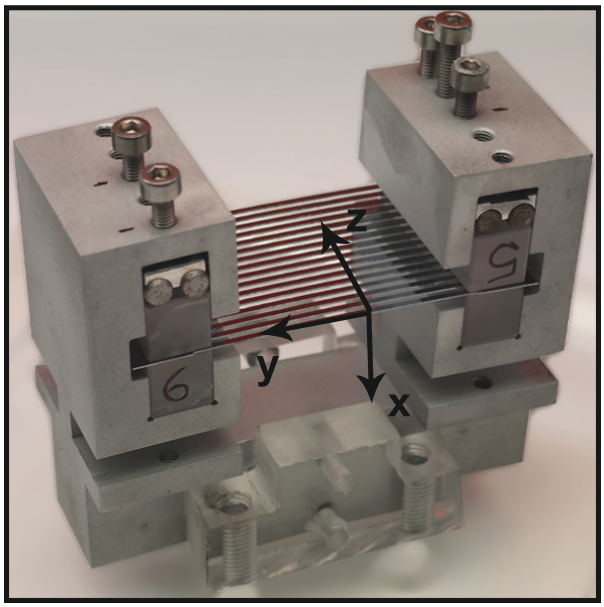

Figure 5.1: Photo of the TCMC tested at H8 line at CERN. A TCMC is a series of crystalline strips merged together by a common frame and aligned to each other to cause MVR.

than 3 μrad, enough to resolve the deflection imparted by an individual VR ($\sim$9 μrad at 400 GeV/c).

Interaction between the proton beam with the TCMC has been studied as a function of the incoming angle of the particles as shown in Fig. 5.2a, where four regions are highlighted. In region 1, extending over (110 $\pm$ 2) μrad, a total of 13 strips are found to cause MVR. In fact, in addition to the twelve aligned strips, a strip is misaligned by an angle less than that of VR acceptance. As expected by interferometric characterizations, the first and the last strips are misaligned (regions 2 and 3). Measured deflection angle for the two strips are (250 $\pm$ 1) μrad and (274 $\pm$ 1) μrad, respectively. Region 2 corresponds to channeling from the last strip, as can be noticed by its broader spot as compared to the one in region 3 due to multiple scattering. Double channeling with an efficiency of (2.5 $\pm$ 0.5) % is recorded in region 4. Particles deflected through channeling by the first strip are rechanneled and deflected by a second crystal, so that deflection angles sum up. Efficiency is limited by non-perfect alignment of the two strips.

To measure MVR characteristics, an angular range of $\pm$ 10 μrad is chosen in the neighborhood of the mean position of MVR angular region (see Fig. 5.2b). Particles impinging onto the crystal in a region of $\pm$ 200 μm from the center of the beam vertical

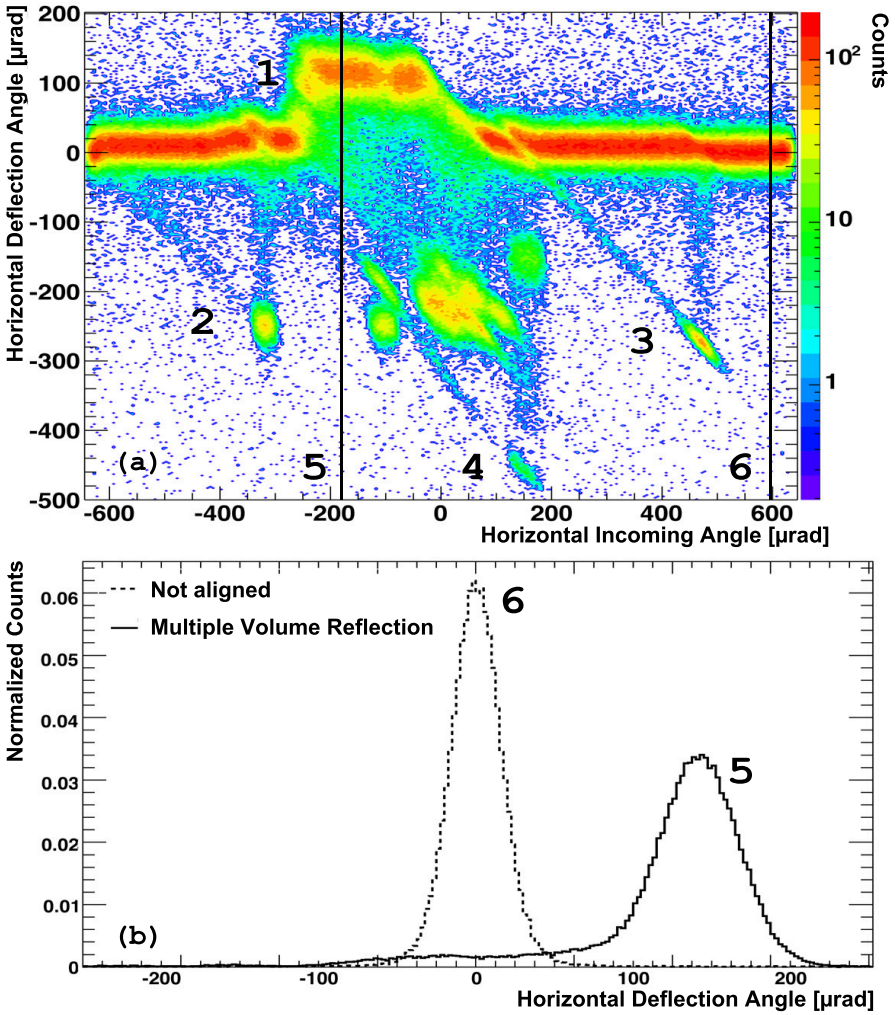

Figure 5.2: (a) Experimentally recorded distribution of 400 GeV/c protons after interaction with the TCMC as a function of horizontal incoming angle and horizontal outgoing deflection angle. Horizontal coordinate refers to coordinate x. Particles undergoing VR and MVRMC have positive deflection angle, while particles undergoing CH have negative deflection angle. Horizontal incoming angle is the angle between the TCMC with the proton-beam direction. Region 1 highlights CH from the first strip, region 2 is for CH from the last strip, region 3 is for MVRMC angular region and region 4 is an example of double channeling. (b) Experimentally recorded distribution of 400 GeV/c protons after interaction with the TCMC on the center of MVRMC region (region 5 in (a)) and in horizontal incoming angle at which no coherent effects appear (region 6 in (a)).

distribution, thereby hitting all the strips, are selected. The efficiency of the MVR process is defined as the fraction of the particles deflected within an angular region of $\pm 3\sigma_{MVR}$ from

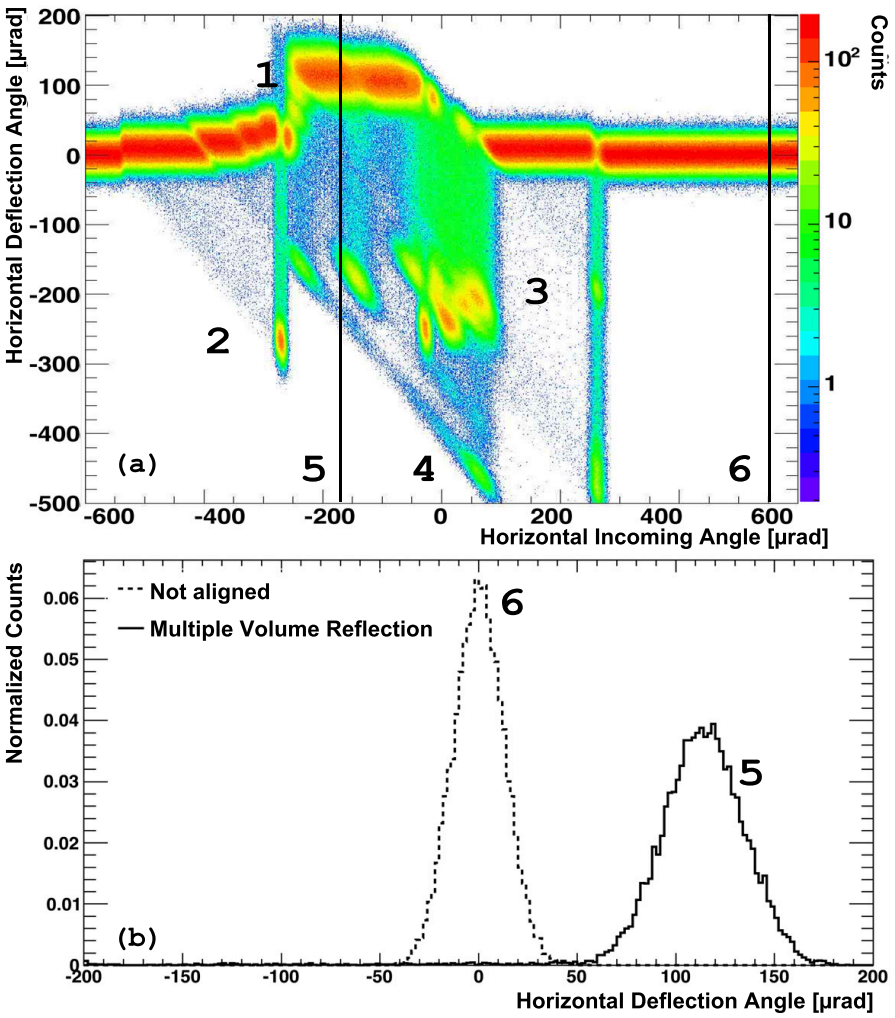

Figure 5.3: (a) Monte Carlo "black-box" simulation of distribution of 400 GeV/c protons after interaction with the TCMC with same meaning of lettering as for Fig.5.2 a. TCMC parameters used in the simulation have been acquired through interferometric measurements of the strip surfaces. (b) Simulated distribution of 400 GeV/c protons after interaction with the TCMC with the same meaning as for Fig.5.2 b.

the average deflection angle over the whole number of particles counted in the acquisition. This value has to be normalized to the ratio of the particles lying within a region of $\pm 3\sigma_{AM}$ for the crystal misaligned with the beam [41]. An efficiency of (96.0 $\pm$ 0.5) % with mean deflection angle of (112.2 $\pm$ 0.1) μrad and mean spread σ_{MVR} = (21.4 $\pm$ 0.1) μrad are measured. Such efficiency overwhelms the maximum observed efficiency for a large deflection angle obtained in previous experiments with coherent phenomena [43, 46]. Based on the deformation and alignment of all the strips determined through interferometry

and the beam parameters, the experiment has been simulated with the "Black-box" Monte Carlo and compared with experimental results (see Fig. 5.2). In Fig. 5.3a and b the results of the emulation for the TCMC crystal for MVR are shown. (98.4 ± 0.1) % efficiency, (114.1 ± 0.1) μrad mean deflection angle, (20.2 ± 0.1) μrad standard deviation are obtained.

5.2 Orientational effects in $Si_{1-x}Ge_x$

In this section we propose the study of graded aperiodic $Si_{1-x}Ge_x$ to manipulate the trajectories of high-energy particles owing to coherent interaction. The crystal has been purposely grown with intrinsically and uniformly curved atomic planes.

Ingots of $Si_{1-x}Ge_x$ single crystals were grown by Czochralski technique [142]. Due to a gradient in Ge concentration, the larger size of Ge atoms with respect to those of Si results in a net curvature of the atomic planes. The lattice parameter of such a crystal changes almost linearly by increasing Ge concentration. $Si_{1-x}Ge_x$ crystals with concentrations up to $x = 7\%$ Ge can be grown with high quality [143, 144]. With current fabrication techniques, the curvature radius can be tailored up to some hundreds meters and down to 15 m. Wafers 500 μm thick were cut from an ingot with the major surfaces of the wafer (111) oriented. Ge concentration was set to produce a cylindrical curvature on a small area [145]. $Si_{1-x}Ge_x$ crystals were introduced in the scientific community to achieve broadband optical components for focusing x- and γ-rays in a Laue lens [146]. Indeed, the usage of graded $Si_{1-x}Ge_x$ in channeling experiments is not a novelty [147–149]. In those cases, the graded crystal was limited to a film deposited onto a conventional crystalline substrate. In contrast, our crystals have no severe constraint with the thickness, so that bulky graded crystals can easily be produced with a thickness up to some mm. In addition, crystal torsion [41] is prevented for graded crystal because of the lack of any external bending device, which is needed by a conventional bent crystal.

Strip-like crystal was achieved by dicing the wafer on the mid-plane of the wafer in order to have the crystalline planes perpendicular to the entry face of the beam. If not, a particle with a trajectory parallel to the geometrical main surface of the strip would not be captured under planar channeling at the entry face, but rather it would cross the crystal as it was an amorphous material or undergo volume reflection [3, 37]. Isotropic etching of the crystal was done according to the procedure described in Refs. [20, 21] to get rid of the lattice damage induced by the blade while dicing. The strip was characterized with the X'Pert Pro MRD XL PANalytical^{TM} high-resolution x-ray diffractometer (HR-XRD). A Ge concentration gradient $0.79 \pm 0.04\%/cm$ was deduced by measuring the variation

of the lattice inter planar distance of the two faces of the sample [150]. Mosaic-spread measurement by HR-XRD [151] allowed one to determine the curvature radius $R = 25 \pm 3$ m. EPD (etch pit density) of the sample was performed after the experiment. 10^2 cm^{-2} dislocation density was measured for both the two faces of the strip.

The crystal was mounted on a two-axis goniometric system with angular resolution $\sim$1 μrad and tested vs. 400 GeV/c proton beam at the H8 line of the CERN-SPS. The beam was tracked before and after interaction with the crystal by a telescope system of Si strip detectors [53]. Each detector featured $\sim$ 5 μm spatial resolution, resulting in $\sim$ 0.5 μrad angular resolution. Beam size $(1.36 \pm 0.02 \times 0.73 \pm 0.01)$ mm^2 and angular divergence $(10.15 \pm 0.04 \times 8.00 \pm 0.03)$ μrad^2 were measured with the telescope system.

The crystal was aligned with the beam for planar channeling or volume reflection. Under planar channeling, the distribution of the outgoing horizontal deflection angle was fitted with one gaussian for the channeling peak, one for the undeflected peak and an exponential for the fraction of particles between the two peaks. Under volume reflection, the distribution was fitted with one gaussian only. Channeling deflection efficiency was computed as the fraction of particles deflected within plus and minus three RMS of the gaussian centered on the mean deflection angle. The efficiency of volume reflection was computed as the fraction of particles deflected within $-\infty$ and plus three RMS of the gaussian. Efficiencies were normalized to the fraction of the particles within plus and minus three RMS of the outgoing distribution when the beam impinging on the crystal is misaligned, i.e., when coherent effects do not take place. An exhaustive description of efficiency calculation methodology can be found in Ref. [41]. Torsion measurement was performed by studying the dependence of maximum efficiency peak on horizontal incoming angle and vertical position.

Analysis was performed over a 500 x 500 μm^2 portion of the incoming beam centered on the strip. Average channeling deflection angle $\Delta\theta_{x,ch} = 156 \pm 2$ μrad, channeling deflection RMS $\sigma_{ch} = 6.6 \pm 0.3$ μrad and channeling deflection efficiency $\epsilon_{ch} = 62 \pm 3$ % were measured. Channeling parameters were obtained by selecting a 2 μrad portion of the horizontal divergence of the incoming beam centered on planar channeling alignment, while no selection was applied to vertical divergence. As a result, crystal bending radius $R = L/\Delta\theta_{x,ch}$ was $R = 25.6 \pm 0.3$ m, $L = 4.00 \pm 0.01$ mm being the crystal length along the beam direction, in good agreement with HR-XRD characterization. Average deflection angle, RMS and deflection efficiency were $\Delta\theta_{x,vr} = -13.5 \pm 0.2$ μrad, $\sigma_{vr} = 7.6 \pm 0.3$ μrad and $\epsilon_{vr} = 96 \pm 2$ % for volume reflection (see Fig. 5.4). Since angular acceptance of volume reflection is equal to the deflection angle of the strip [37], no selection was applied to the horizontal and vertical divergences. Torsion was measured to be less than 1 μrad/mm, as expected.

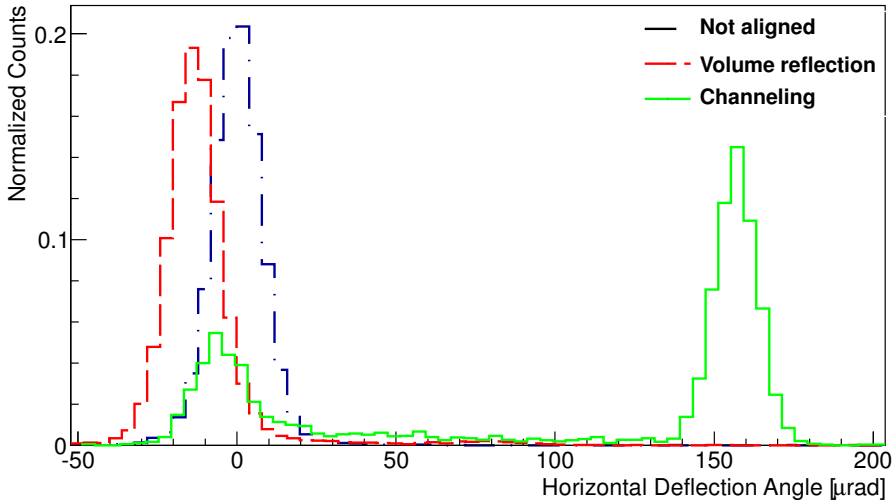

Figure 5.4: Distribution of the deflection angle of particles after the interaction with the crystal aligned for planar channeling (continuous line), for volume reflection (dotted line) and not aligned for any coherent effect (dot-dashed line).

To interpret experimental data of $Si_{1-x}Ge_x$ crystals, simulation of a strip with the same geometrical features has been worked out through Monte Carlo simulation with the DYNECHARM++ toolkit. The presence of higher atomic-number Ge atoms in the lattice [152] increases the depth of the potential well (see Fig. 5.5.a), slightly affecting channeling critical angle ($\simeq$ 9.6 μrad vs. $\simeq$ 9.5 μrad) with respect to pure Si crystal. Thereby, the average contribution of Ge atoms has been included in the calculation of the continuous potential averaged along main planes [79, 110]. The enhancement of static lattice disorder caused by the coexistence of different bond lengths in the crystalline matrix negligibly alters the efficiency because the maximum difference between Ge-Si and Si-Si bond length is $\sim$0.02 Å for diluted Ge concentration [152]. Therefore, atomic static displacement cannot exceed this value, causing a small increase in the Debye-Waller factor and a consequent decrease in channeling deflection efficiency to less than 1 % [57].

Monte Carlo simulations with and without the presence of edge dislocations have been performed to quantify their influence on coherent effects. Measured beam parameters and dislocation density per cm^2 have been used as inputs. Electrical characteristics of the $Si_{1-x}Ge_x$ has been evaluated by considering the influence of both Si and Ge atoms. Calculated efficiency for channeling and volume reflection are $\epsilon_{ch,MC} = 76.5\pm1.5\%$ and $\epsilon_{vr,MC} = 98.0\pm0.5\%$, respectively. Once the dislocations are included, the same physical quantities hold $\epsilon_{ch,MC,dis} = 62.5\pm1.5\%$ and $\epsilon_{vr,MC,dis} = 96.5\pm1.0\%$. Fig. 5.5.c shows a comparison between the experimental record and the Monte Carlo simulations.

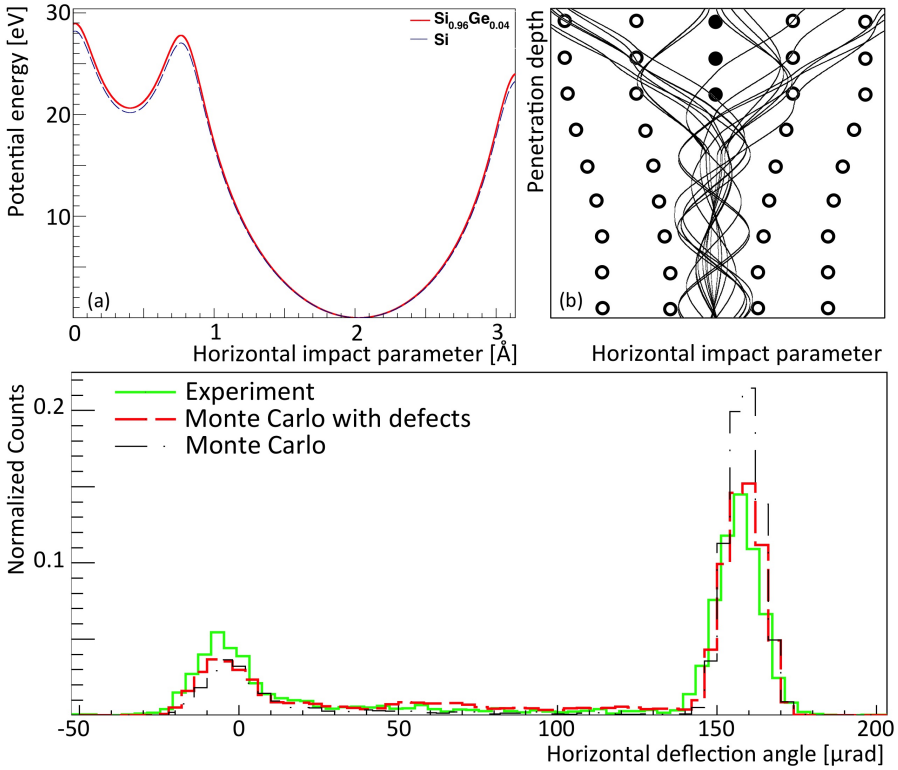

Figure 5.5: (a) Average (111) interplanar potential energy for a perfect Si crystal and for a $Si_{0.96}Ge_{0.04}$ crystal. (b) Qualitative schemes of lattice misalignment due to edge dislocation and its influence on particle trajectories. (c) Experimental data (continuous line), Monte Carlo simulation (dot-dashed line) and Monte Carlo simulation including the presence of defects (dotted line) of the distribution of horizontal deflection angles of particles after the interaction with the crystal aligned for planar channeling.

As expected, the probability to undergo dechanneling, i.e., to leave the channeling state, rises up because of the presence of the strain field generated by defects. Such effect manifests itself all the way along the trajectory (see Fig. 5.5 (b)) of a channeled particle in the crystal and consequently spoils deflection efficiency. On the contrary, volume reflection acts within one particle oscillation in the crystal, i.e., for about a few tens of μm at 400 GeV/c. Hence, the presence of neither Ge atoms nor defects are crucial and deflection efficiency is very much the same as for a perfect bent crystal. In some more general sense, volume reflection is more robust than channeling vs. presence of crystal imperfection and/or impurities, and that explains why the latter has been observed to perform very efficiently with high-energy particles solely in the cases of Si [43] and high-purity Ge [49].

5.3 High-efficiency Ge

Germanium may be a valid alternative to Silicon for channeling. However, the usage of Ge for orientational effects at high-energy has been retarded by the lack of defect-free samples. Because the Ge atomic number is the double of the Si, higher critical angle and efficiency of deflection are expected under channeling. The angle of deflection for volume reflection also benefits because it linearly depends on the critical angle for channeling. In addition, the Tsyganov critical curvature and radiation emission efficiency should increase by a factor 2 with respect to Si because they linearly depend on Z.

In this experiment we tested two Ge strips oriented along (111) and (110) planes [49, 153, 154]. The length of the strips along the beam are 1.85 mm and 1.97 mm, respectively. Ge is nowadays available in high-quality wafers ($\sim$ 1 dislocation / cm^2 as for Si). The strips were fabricated according to the procedure described in Refs. [154, 155], which makes use of chemical etching and does not alter the crystalline structure at the entrance surface of the samples. Moreover, the bending strategy based on the exploitation of anticlastic deformation [140] allows to achieve homogenous curvature, thus causing an enhancement of deflection efficiency. The strips highlight two different planes for channeling, the (111) and (110). Each strip was bent at two different curvature radius.. Planar channeling and volume reflection were intensively investigated. In addition, axial channeling along the <110> axis was observed for the first strip.

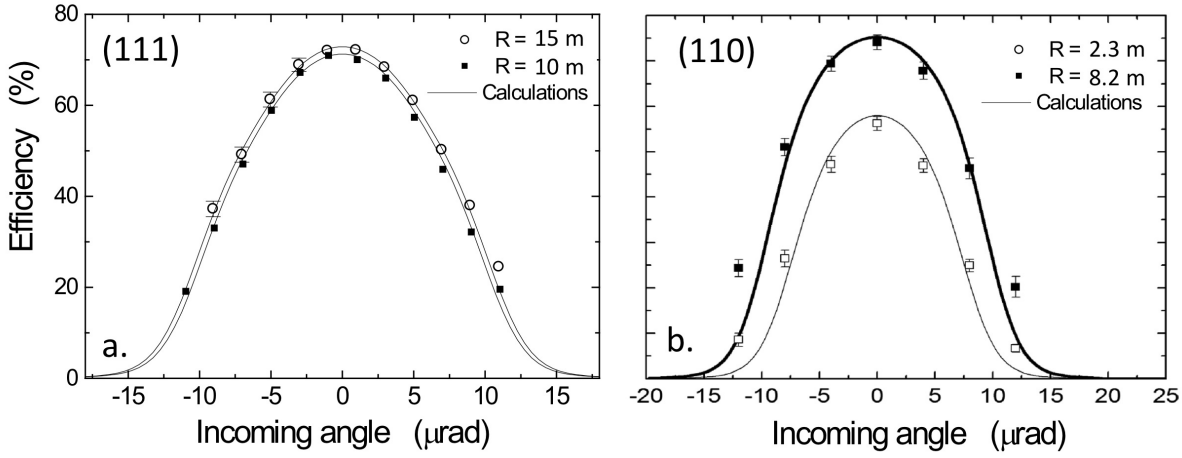

Figure 5.6: Efficiency of deflection vs. the incoming angle for 400 GeV/c proton under planar channeling in Ge (111) (a.) and (110) (b.) planes for various bending radii. To be noted different range of abscissa.

The experiment was carried out at the H8 extracted beam line of the SPS accelerator at CERN in two runs. The beam was tracked before and after interaction with the crystal by two Si strip detector telescope system [156]. Beam had 11.6 μrad horizontal and 9.4 μrad and vertical divergence at the crystal entrance for the run with the (111) strip and 10.8 μrad horizontal and 8.0 μrad and vertical divergence with the (110). The crystal was mounted on a two-axis high resolution ($\sim 2\mu$rad) goniometer. Measured maximum efficiency, mean deflection angles and root mean squares of deflection angles for planar channeling are reported in Tab. 5.1. The analysis was performed on a 0.4 x 1.0 mm^2 area of the sample and an angular window of ± 2 μrad on the distribution of horizontal incoming angles. Channeling efficiency was also measured as a function of the horizontal incoming angle. In Fig. 5.6 the efficiency of deflection vs. the reciprocal alignment between particle direction and plane orientation are shown.

Table 5.1: Maximum efficiency ($\epsilon_{ch,max}$) and Mean deflection angle (μ_{ch}) and Root mean square of deflection angles (σ_{ch}) for planar channeling

Plane	Radius (m)	$\epsilon_{ch,max}$ (%)	μ_{ch} (μrad)	σ_{ch} (μrad)
(111)	15	(72.5 ± 1.5)	(122 ± 2)	(6.4 ± 0.3)
(111)	10	(71 ± 1)	(185 ± 2)	(5.7 ± 0.3)
(110)	8.2	(74.1 ± 1.5)	(242 ± 2)	(6.4 ± 0.3)
(110)	2.3	(56.2 ± 1.5)	(854 ± 3)	(5.7 ± 0.3)

For volume reflection the area for the analysis was the same. No angular window was selected, since the incoming divergence of the beam is small compared to the angular acceptance of the volume reflection effect. Results are reported in Tab. 5.2.

Table 5.2: Maximum efficiency ($\epsilon_{vr,max}$)and Mean deflection angle (μ_{vr}) for volume reflection

Plane	Radius (m)	$\epsilon_{ch,max}$ (%)	μ_{ch} (μrad)
(111)	15	(95.9 ± 0.4)	(15.9 ± 0.3)
(111)	10	(95.3 ± 0.4)	(15.3 ± 0.3)
(110)	8.2	(96.6 ± 0.9)	(17.3 ± 0.3)
(110)	2.3	(99.5 ± 0.8)	(11.4 ± 0.2)

The (111) strip with $R = 15$ m was also aligned along the <110> axis under axial channeling condition. In Fig. 5.7 a two-dimensional histogram of the angular deflection in

the vertical and horizontal planes is shown. The plot is obtained by selecting the incoming particles impinging on the strip with a circular angular window with radius 5 μrad on the plane consisting in horizontal and vertical incoming angles. The main feature is the spot deflected at around 122 μrad a the horizontal angle and 0 μrad vertical. The angular spread of the deflected particles was 13 ± 1 μrad rms. This spread is 2.3 times larger than the one obtained in (111) planar channeling, because of the particles deflected by doughnut scattering. In fact, the 15 m radius for Ge <110> is double the critical radius for axial channeling, a suitable condition to generate doughnut scattering [157]. On the other side, particles suffering dechanneling are readily captured into planar channeling by skew planes. As a result, $\sim 96\%$ of the particles are deflected at an horizontal angle > 0 μrad, thanks to the concomitant contribution of axial channeling, doughnut scattering and planar channeling in skew planes.

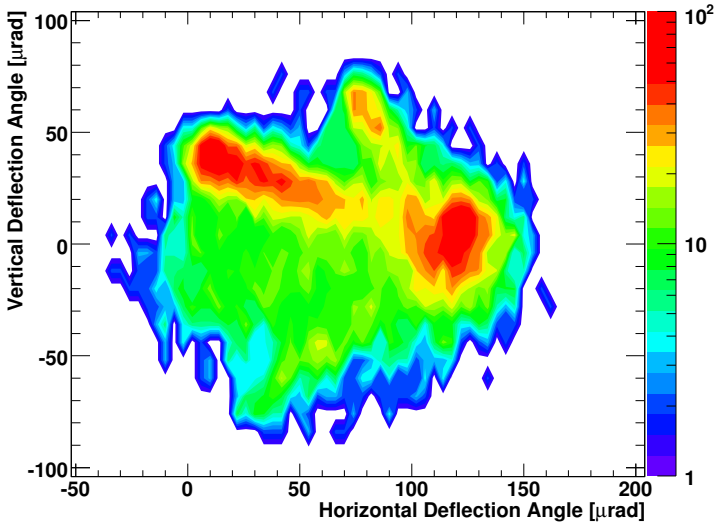

Figure 5.7: Distribution of the vertical vs the horizontal deflection angles for 400 GeV/c proton beam aligned with <110> Ge axis.

The DYNECHARM++ code has been used to simulate the channeling experiment, as summarized in Tab. 5.3. In order to correctly consider the contribution of the multiple scattering in the detectors, the incoming and outgoing angular distributions have been convoluted with the resolution of the experimental detectors. Since the Si detector is 330 μm long, the multiple scattering from two Si detectors used is ~ 2.5 μrad. For the outgoing angle the same holds. By considering the error of the incoming and the outgoing angle independent, the resolution of the deflection angle can be approximated by ~ 3.5 μrad.

Values are compatible with the experimental results. Efficiencies are quite close except

Table 5.3: Maximum efficiency ($\epsilon_{ch,max}$) and Mean deflection angle (μ_{ch}) and Root mean square of deflection angles (σ_{ch}) for DYNECHARM++ simulations

Plane	Radius (m)	$\epsilon_{ch,max}$ (%)	μ_{ch} (μrad)	σ_{ch} (μrad)
(111)	15	74	124	5.6
(111)	10	71	186	5.4
(110)	8.2	83	241	5.7
(110)	2.3	57	857	5.0

for the crystal with 8.2 m bending radius. The main difference lies in the values of σ_{ch} which can be ascribed both to simulation or to wrong assumption on the resolution of the Si detector contribution.

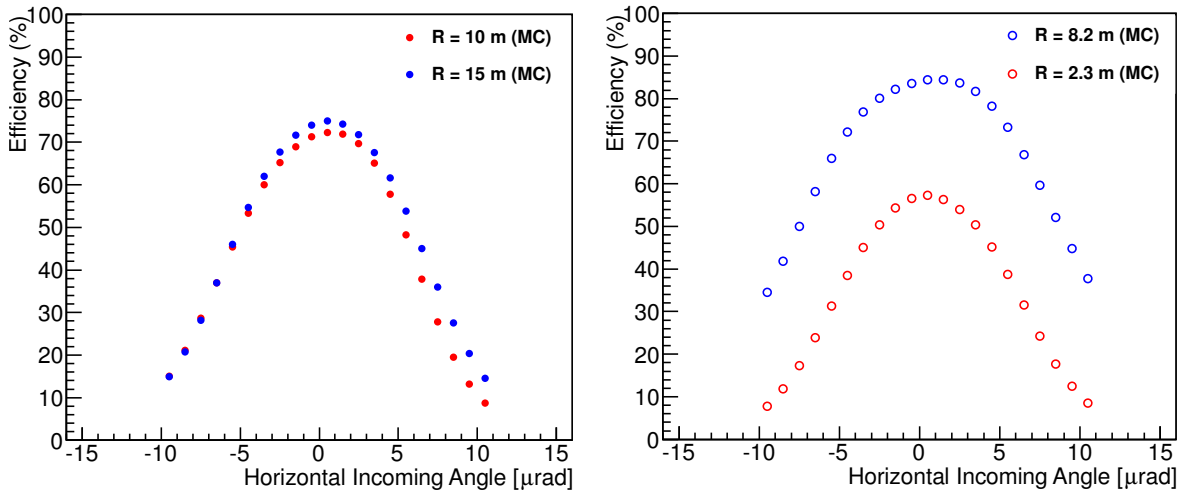

Figure 5.8: Efficiency of deflection vs. the incoming angle for 400 GeV/c proton under planar channeling in Ge (111) (a.) and (110) (b.) planes for various bending radii.

5.4 Evidence of planar channeling in a crystalline undulator

Recent developments in the fabrication of free electron laser based on magnetic undulators (FELs) have pointed out the possibility to gain high-intensity and monochromatic electromagnetic radiation through relativistic beam. Due to its features, application of FELs extend from solid state physics, material science and semiconductor industries to

molecular biology, medical diagnosis and medicine. Since usage of magnetic undulator adds constraint to the minimum oscillation period reachable, new techniques are under development in order to reach radiation of higher frequency than the FELs.

A crystalline undulator (CU) has been identified as a promising technique to reach such goal. The main idea of the CU is to impress the oscillatory motion to a bunch of particles by exploiting the strong interplanar field generated by ordered atoms in an oriented crystal. When a charged particle hits an oriented crystal, it can be captured between atomic planes, i.e., the particle undergoes channeling. Since the structure of Si can tolerate stress and torsion remaining into the elastic regime until the breaking point, a crystal with a periodic deformation can be fabricated in order to procure the frequency range of hard X- and gamma-ray with a single crystal of few millimeters.

The fabrication of a crystalline undulator requires both a high-precision in the shaping of the structure and a low-level of induced defects. A promising solution relies on the grooving method [109, 158, 159]. Surface grooving produces permanent plastic deformation in the neighborhood of the grooves. Indeed, plasticization occurred in a thin layer transfers coactive forces to the crystal bulk, thus producing an elastic strain field within the crystal. It was shown that a series of superficial grooves performed on a surface of a crystal may permanently and reproducibly bend the whole crystal. Since the invention of the method of superficial grooving, great progress has been done to improve the reliability of the technique. In particular, this method has been developed to produce bent crystals tailored for the realization of optics for hard X rays (e.g. Laue lens) [160, 161]. To date, this technique can be regarded as a mature method to reduce curvature between a crystal [162].

To realize the crystalline undulator via superficial grooving method, an alternating pattern of parallel grooves was performed on both surfaces of a 5 mm long Si strip [109, 158, 159]. The largest faces of the strip were given 1 mm periodic micro-scratches (grooves), by means of diamond blade through the usage of a DISCO DAD 3220 dicing machine. A proper indentation depth was adopted to achieve a $\sim$ 65 Å oscillation amplitude. The smaller face orthogonal to the (1 1 1) plane and <1 1 0> axis was the entry surface of the beam.

The undulator crystal was mounted on a two-axis goniometer with 2 μrad resolution and exposed to the 400 GeV/c proton beam of the H8 beam line at CERN-SPS. The beam was tracked before and after interaction with the crystal by a telescope system of Si strip detectors [38]. The beam has a size of 10.2 ± 0.1 μrad horizontal RMS divergence and 8.0 ± 0.1 μrad vertical RMS divergence.

The undulator was mounted with the vertical angle purposely misaligned to avoid axial

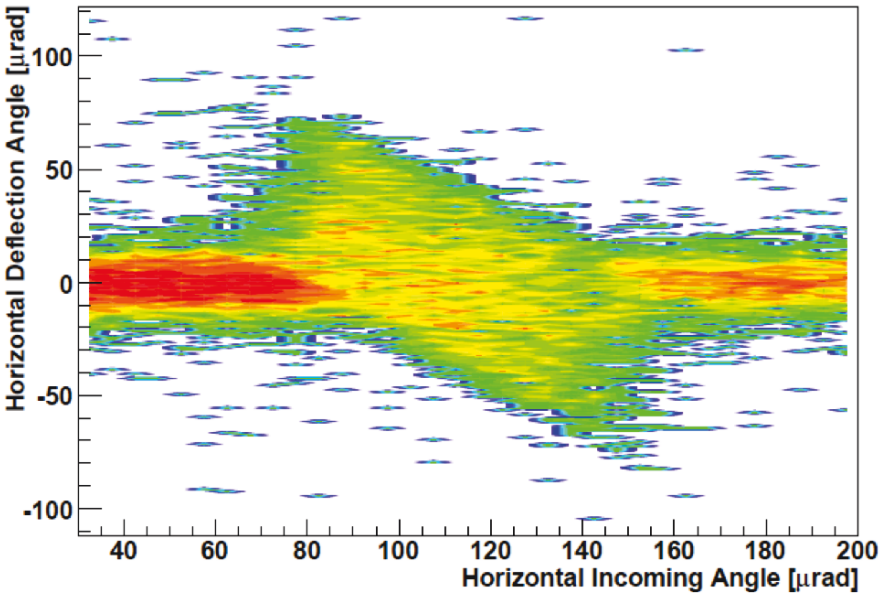

Figure 5.9: Horizontal deflection angle vs. horizontal incoming angle for a crystalline undulator exposed to a 400 GeV/c proton beam.

channeling. Pre-alignment of the sample was worked out by means of a laser system parallel to the beam direction. Distribution of deflection angle of the beam vs an horizontal angular scan of the Euler cradle was performed (see Fig. 5.9). By comparing with Si (1 1 0) angular scan with Fig. 1.8, a noticeable difference existed. In fact, the undulator exhibited a two-fold structure because particles are deflected both to plus and minus angles with the same intensity spanning over the whole angular acceptance. Such pattern suggested the presence of two curvatures in the crystal with opposite signs.

In order to get an insight into the experimental result the DYNECHARM++ toolkit was adopted. For every particle, the trajectory was simulated through the numerical resolution of the equation of motion. Undulator geometry was approximated through a sinusoidal function with the expected amplitude and oscillation period. The influence of such geometry on particle trajectories was evaluated through the application of a position-dependent centrifugal force. Intensity of scattering on nuclei and electrons was averaged over nuclear and electron densities in the channel to estimate the dechanneling probability.

Simulated particles were tracked during all the particle motion. Fig. 5.10 shows the distribution of horizontal deflection angle vs. the horizontal incoming angle for four different penetration depths. As shown in Fig. 5.10.a, at quarter-period of the undulator clear typical markers of a bent crystal are present, in particular channeling and volume

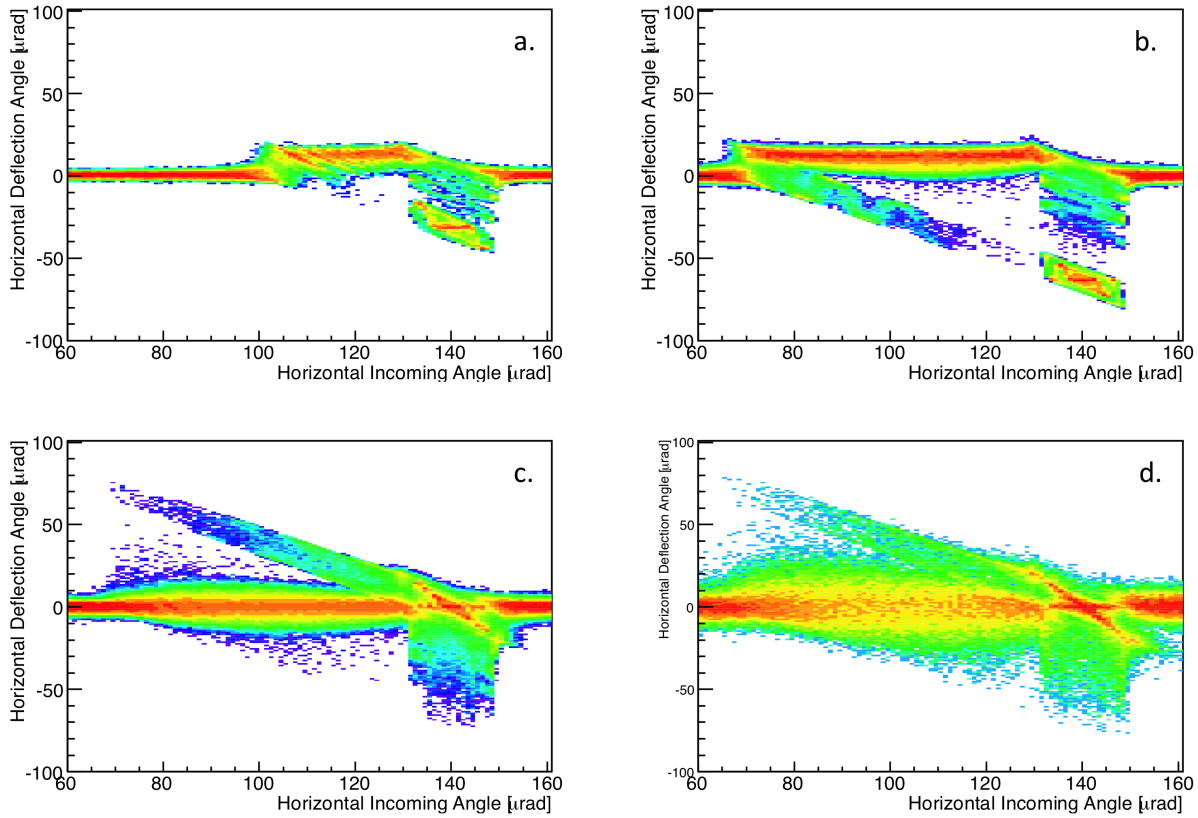

Figure 5.10: Monte Carlo simulation of horizontal deflection angle vs. horizontal incoming angle for a crystalline undulator exposed to a 400 GeV/c proton beam at various penetration depths.

reflection. In fact, channeled particles are distinguishable because they received -30 μrad deflection kick. On the other side, particles impinging tangent to the crystalline curved planes are deflected to the opposite direction, i.e., they undergo volume reflection. At half-period, particles suffering the strong centrifugal force to the opposite direction leave the channeling state (see Fig. 5.10.b). At such penetration depth, a fraction of particles is still trapped into the crystalline potential well, acquiring an overall zero deflection angle. After an entire period, the general picture evolves towards a double fold distribution, as shown in Fig. 5.10.c. Indeed, the particles undergoing volume reflection in the first half bounce against the potential wall of the second half-period with inverted bending radius or are captured into a channeling state and reflected to the opposite side. Finally, Fig. 5.10.d shows the simulation of the complete periodically bent crystal. Particles which are channeled along all the crystal exits with overall zero deflection angle. Reflected particles continue bouncing due to the increasing intensity of interaction with nuclei and electrons

during their motion.

5.5 Channeling efficiency vs. bending radius

Crystals with small thickness along the beam exhibit top performance for steering particle beams through planar channeling. The key parameter regarding utilization of bent crystals for beam manipulation is deflection efficiency. As some examples, performance of beam extraction and collimation via channeling is critically linked to the fraction of the beam deflected [18, 25]. The advent of a new generation of crystals manufactured through micro machining techniques allowed fabricating crystals with a thickness along the beam comparable to or even much lower than the nuclear dechanneling length. Thus, usage of such crystals allowed to measure nuclear dechanneling length and to record efficiencies larger than the maximum level foreseen [43]. "Thin" crystals in circular accelerators boosted extraction efficiency [163] and demonstated the possibility to be used as primary collimators [26]. Such crystals pointed out the necessity to revise the physical models to describe the dynamics of channeling features. In particular, no systematic measurement of deflection efficiency for channeling at various bending radii existed. The problem has been addressed through experimental work carried out with 400 GeV/c protons at fixed-target facilities of CERN-SPS. The dependence of efficiency vs. curvature radius has been investigated and compared to Monte Carlo simulation and analytical models.

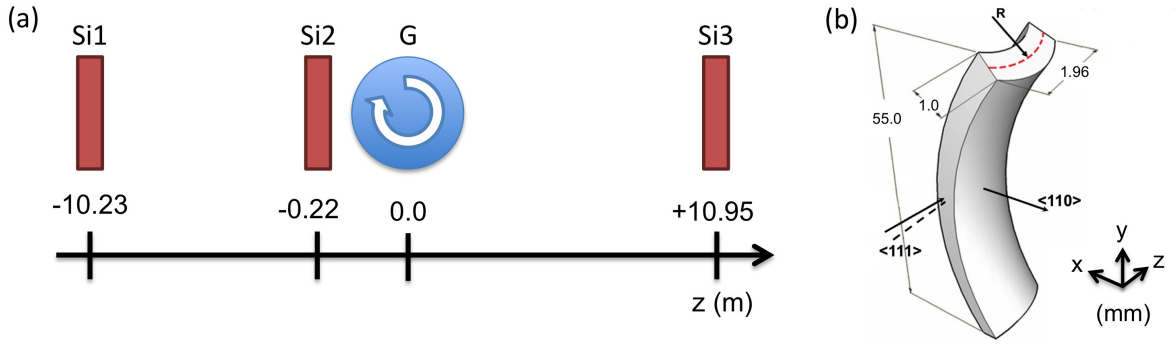

Figure 5.11: (a) Experimental setup used during data taking at H8 external line of the SPS accelerator at CERN. Three Si strip detector (S) were mounted $\sim$ 10 m one from another in order to reach a μrad angular resolution in the reconstruction of the particle track. The crystal was mounted on a high-resolution two-axis (G) offering an accuracy of 1.0 μrad. (b) A sketch of the bent Si strip.

The experiment was performed at external line H8 of the Super Proton Synchrotron

(SPS). A single strip-like crystal offering (110) planes for channeling was shaped to the size of 1 x 55 x 1.96 mm^3. The crystal was fabricated by means of silicon anisotropic etching techniques [20, 21]. The strip was mechanically bent through a purposely fabricated crystal holder made of Al [22]. Primary curvature along the 55 mm size was imposed through the holder to cause a secondary curvature driven by anticlastic deformation [140, 164] on the 1.96 mm size. The holder was mounted on a high-resolution two-axis goniometer with accuracy of 1.0 μrad on both movements. The crystal was exposed to a beam of 400 GeV/c protons with 10.2 ± 0.1 μrad horizontal RMS divergence and 8.0 ± 0.1 μrad vertical RMS divergence. Particle trajectories were tracked before and after interaction with the crystal thanks to a telescope made by three double-sided Si microstrip detectors [38].

The bent strip was aligned to attain the condition for planar channeling far from alignment with main <111> crystal direction to avoid interference by axial channeling. Optical pre-alignment of the strips without the beam was accomplished through a laser system, which allowed evaluating the relative angle between the strip face parallel to the beam and the beam direction. After that, an angular scan with the goniometer was performed in order to determine the best channeling alignment through the evaluation of the efficiency of deflection of the strips. When the maximum efficiency had been recorded, a low-statistic run was performed to measure the crystal torsion. A precise screw-system installed on the strip-holder was adopted to compensate for strip torsion induced by mechanical stresses [22]. The effect of residual torsion on channeling efficiency was corrected through a specific selection algorithm to add horizontal angular shift to an incoming particle proportional to its vertical impact parameter. Evaluation of strip torsion was first performed by studying the dependence of the maximum of efficiency peak on the horizontal incoming angle and vertical position. Precise measurement of residual torsion are reported in Tab. 5.4. Five curvatures of the crystal were considered and the whole procedure was repeated for each of them.

Data analysis was performed over a 800 x 2000 μm^2 portion of the incoming beam centered on the strip. Analysis of channeling deflection efficiency was done by selecting a 2 μrad wide region of horizontal angle of incoming particles over the observed peak of the maximum of channeling efficiency. The distribution of the outgoing horizontal deflection angle was fitted with one gaussian for the channeling peak, one for the undeflected peak and an exponential for the fraction of dechanneled particles between the two peaks, i.e., for the fraction of the particles not channeled at full bending angle. Channeling deflection efficiency was computed as described in Ref. [41]. Measured efficiencies for the five bending radii are reported in Tab. 5.4 and shown in Fig. 5.12.

In order to compare the experimental results with the DYNECHARM++ Monte Carlo

Table 5.4: Experimentally measured parameters of channeling. Radius is the bending radius of the crystal, $\Delta\theta$ the mean horizontal deflection angle, τ the torsion of the strip, ϵ the deflection efficiency evaluated as in Ref. [41]

Radius (m)	$\Delta\theta$ (μrad)	τ (μrad/mm)	ϵ (%)
28.4±0.4	69±1	12±1	81±4
18.4±0.2	107±1	-9±1	80±3
6.8±0.1	289±3	1±2	71±1
3.5±0.1	555±4	2±2	57±1
2.3±0.1	847±5	11±1	34±4

simulation and the analytical models for efficiency, the same input parameters have been used for the calculations. The fraction of particles impinging onto the nuclear corridor is $\sim 19.5\%$ [51], the critical radius and the oscillation period are $R_c \sim 0.7$ m and $\lambda \sim 67.5\mu m$ [57], respectively. Approximation of experimental form factor of Ref. [165] has been adopted to describe the electron density for a Si atom for the analytical calculation and Monte Carlo simulation. Calculated efficiencies for the three models are reported in Tab. 5.5 and visually superimposed to the experimental results in Fig. 5.12.

Table 5.5: Channeling efficiency of experimental data (Exp.) and calculation with analytical (An.), semi analytical (S.a.) and Monte Carlo (MC) methods. Values are also shown in Fig. 5.12

R/R_c	Exp.	An.	S.a.	M.C
40.6	81	81.1	83.1	81.2
26.3	80	79.0	81.9	79.7
9.7	71	68.2	74.1	72.3
5.1	57	56.3	54.1	56.8
3.3	34	43.7	40.42	39.9

As clearly shown in Fig. 5.12, the three models exhibit rather similar trends. The prevision of theoretical estimates lie within $\pm 5\%$ in efficiency from the corresponding experimental values. Though, the Monte Carlo method outputs the most accurate values. The dependence on radius for all the three models well follows the experimental curve, except for the zone near the critical radius. The discrepancy in this case has to be ascribed to the lack of knowledge of the exact density distribution between atomic planes. Indeed, dechanneling probability significantly changes with the atomic distribution in the structure

because of the different average density of nuclei and electrons encountered by a particle in its trajectory. In particular, the more the crystal is bent the more the particles are pushed against the high-density atomic region, i.e., the zone within which nuclear dechanneling takes place. To study the dependence of efficiency on atomic density, we have adopted two different models for the atomic form factor, i.e, the Moliére approximation and the approximation based on the experimental x-ray diffraction data. Channeling efficiency between the calculation of the above form factors differs by +0.4% and +3.0% at R/R_c equal to 40.6 and 3.3, respectively. Since, the efficiencies do not scale proportionally with the bending radius, the need for more precise experimental measurement of nuclei and electronic density arises to better evaluate and simulate channeling efficiency in a thin highly bent crystal.

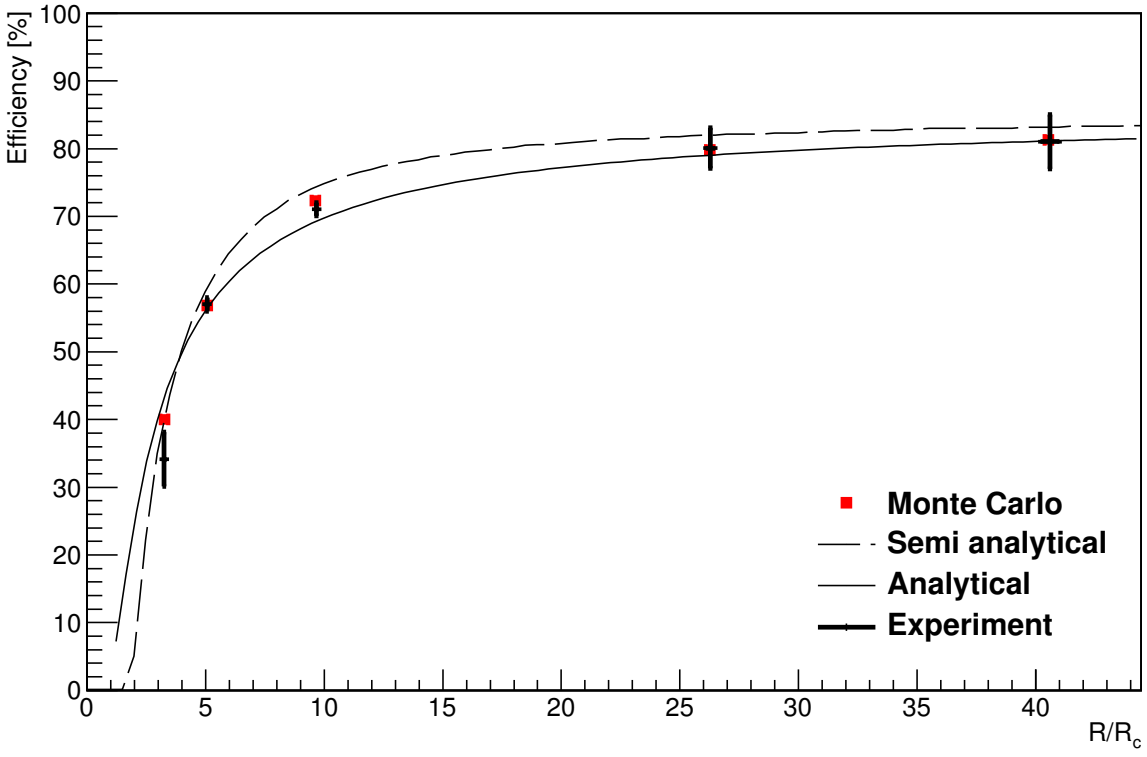

Figure 5.12: Channeling efficiency plotted Vs bending radius (R) over critical radius (R_c) for experiments with 400 GeV/c protons impinging on a Si crystal and for the analytical, the semi analytical and the Monte Carlo calculation methods.

5.6 Dechanneling length of 150 GeV/c π^-

In this section we present the measurement of the dechanneling length of 150 GeV/c π^- interacting with a short bent Si crystal.

Dechanneling of negative particle has been poorly investigated [78] because of the experimental difficulties encountered in studying channeling for such particles. Past experiments measured the dechanneling length of 1 GeV/c and 2-55 GeV/c electrons in a straight crystal [166, 167]. In this case, studying the emitted channeling radiation in an unbent crystal allows only an indirect measurement of the dechanneling length. Conversely, usage of bent crystals represents a useful opportunity for a direct measurement of the dechanneling length.

A slightly bent crystal ($R \gg R_c$, R being the crystal radius and R_c the critical radius [1, 2]) is the ideal choice to perform measurements of the dechanneling length. A slight bend to the crystal does not significantly alter the potential experienced by channeled particle with respect to an unbent crystal, and allows a direct measurement of the number of dechanneled particles as a function of the crystal depth. In fact, particles dechanneled at a crystal depth z are deflected by an angle $\theta_z \approx z/R$, thereby a measure of the rate of dechanneled particles as a function of crystal depth can be inferred [43, 67].

The experimental setup described in Ref. [38] allows reconstructing particle trajectories with an angular resolution of 2 μrad, which is limited by multiple scattering of particles in the detectors and in the air. A strip crystal of size 70x1.91x0.9 mm^3 (labelled as ST15) with the largest faces oriented parallel to (110) planes has been used. The crystal was fabricated according to the procedure described in Refs. [20, 21] and bent through anticlastic deformation [140].

The crystal was tested first with a 400 GeV/c proton beam at CERN-H8 line to compensate for the initial torsion [22], which inevitably comes out once the crystal has been mounted on the holder. Torsion was reduced to less than 3 μrad/mm. A deflection angle $\theta_{ch} = (99.6 \pm 0.2)$ μrad, deflection efficiency $\epsilon_{ch} = (79.3 \pm 0.9)$ % and $L_n^{(+)} = (1.23 \pm 0.05)$ mm have been measured. Deflection efficiency $\epsilon_{ch} = (79.1 \pm 0.4)$ % and nuclear dechanneling length $L_n^{(+)} = (1.18 \pm 0.03)$ mm predicted through simulation [138] are in good agreement with the experimental results.

Lately, the crystal was moved to CERN-H4 line and exposed to 150 GeV/c π^- beam. A deflection efficiency of (12.5 ± 1.0) % was recorded, in agreement with the simulation result (14.3 ± 0.3) %. Fig. 5.13 shows beam distribution after interaction with the crystal oriented for channeling. By fitting the dechanneling part of the distribution with the exponential function between the two maxima, we found $L_n^{(-)} = (0.93 \pm 0.05)$ mm, in agreement with

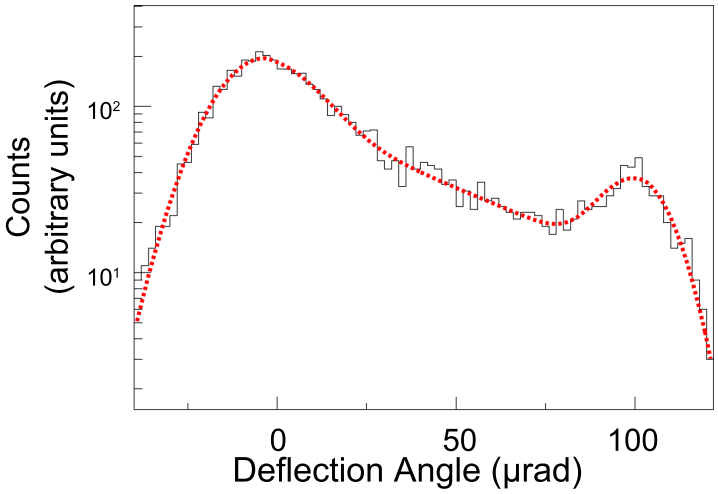

Figure 5.13: Distribution of deflection angle of 150 GeV/c π^- passed through a 1.91 mm long silicon crystal bent at $R = 19.2$ m along (110) planes. Only particles hitting the crystal within an angle of 5 μrad are selected. A fit was done with the sum of two gaussians shifted apart and an exponential function in between, the last one provides a measure of the $L_n^{(-)}$.

the DYNECHARM++ simulation result of (0.95±0.03) mm. By using Eq. 1.38 to evaluate $L_n^{(-)}$ we found (0.92 ± 0.05) mm, in agreement with the previous estimation.

In order to test the Geant4 model for channeling also for negative particles, such experiment has been reproduced. A dechanneling length of 1.54 ± 0.05 mm is obtained by Geant4 simulation with density computed by DYNECHARM++ code and 0.71 ± 0.05 mm with the density computed by the model of Geant4 (see Fig. 5.14). Dechanneling rate is increased or decreased due to stronger incoherent scattering with nuclei and electrons. Thus, the model is very sensitive to the distribution of nuclei and electrons and the average density as a function of the transverse energy of the particles. Both the simulations are in fair agreement with the data. However, the first outputs a value higher than expected, while the second is lower. Thus, the model for negative particle is very sensitive to the interaction rate in one oscillation period, since a big discrepancy between the two simulations exists. Indeed, the discrepancy of the dechanneling lengths turn into a big discrepancy in channeling efficiency, which pass from $26.8 \pm 0.5\%$ to $6.2 \pm 0.5\%$. As a consequence, by accurately computing the average density experienced by a particle the model can be able to output the measured dechanneling length.

The theory of dechanneling described in Ref. [57] investigates electronic dechanneling of positively charged particles under the assumption that distance from nuclei is larger than the Thomas-Fermi radius r_{TF}. However, if this theory would be applied to nuclear

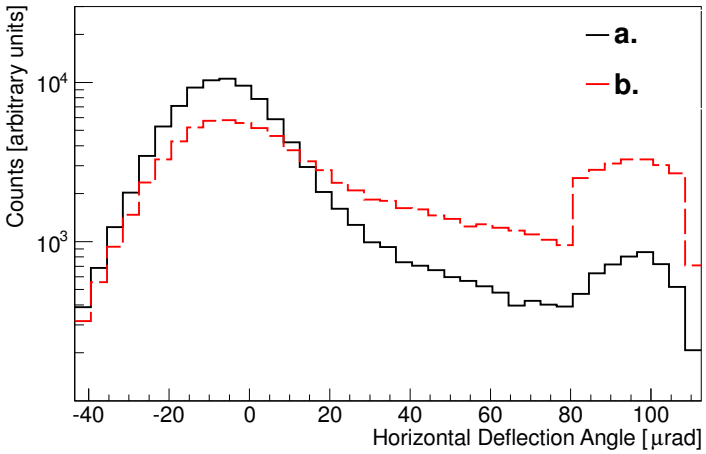

Figure 5.14: Geant4 simulation of the distribution of deflection angle of 150 GeV/c π^- passed through a 1.91 mm long silicon crystal bent at $R = 19.2$ m along (110) planes. Only particles hitting the crystal within an angle of 5 μrad are selected. Quantity of average density experienced by a channeled particle has been computed through DYNECHARM++ (a.) and algorithm implemented into Geant4 (b.).

dechanneling in spite of the vicinity of channeled particles with the nuclei, it comes out that the dechanneling length is proportional to pv. By comparing the results on $L_n^{(-)}$ for 150 GeV/c π^- with previously published paper on $L_n^{(+)}$ for 400 GeV/c proton it comes out a discrepancy between the 150 GeV/c $L_n^{(-)}$ the $L_n^{(+)}$ as scaled to the same energy. Such discrepancy is to be ascribed to the non validity of the assumption that the distance of the particles from the nuclei is larger than r_{TF}. However, due to independence of incoherent interaction strength on the charge sign and since the encountered average density has the same order of magnitude, the $L_n^{(-)}$ particles is of the same order of magnitude as the $L_n^{(+)}$. This knowledge may be important for the design of crystals for channeling of negative particles, inasmuch as it may open up new applications, such as steering of high-energy negative particle beams and the realization of innovative radiation sources.

5.7 Multiple Volume Reflection in One Crystal for 150 GeV/c π^-

This chapter presents the observation of multiple volume reflection in one crystal for 150 GeV/c negative particles, π^- mesons.

The experimental setup was the same as in Ref. [38]. Two upstream and two down-

stream silicon detectors measured the particle incoming and outgoing angles with a resolution of 8 μrad. The resolution was limited by the multiple scattering of the particles with the air.

A 70 x 2 x 0.5 mm^3 silicon strip was fabricated according to the technologies [20, 21]. The largest faces were parallel to the (110) planes and the side faces to the (111) planes. The strip was bent through anticlastic curvature produced along the crystal width. The crystal was mounted on a high-resolution two-axis goniometer with an accuracy of 2 μrad. The bending angle $\alpha = (702 \pm 0.4)\mu$rad was preliminary measured with a 400 GeV/c proton beam on H8 line. The divergence of the beam was $\sigma_x = (26.04 \pm 0.05)\mu$rad and $\sigma_x = (25.66 \pm 0.04)\mu$rad in the horizontal and vertical planes, respectively.

The optimal alignment for multiple volume reflection requires the exact knowledge of the axial channeling orientation. Thus, the horizontal orientation angle θ_h was scanned to find the angle θ_h^p of planar channeling in the (110) vertical plane. Then, the angle θ_v^a of axial channeling was found by scanning the vertical angle θ_v. The angles were tilted to the optimal level $\theta_{x0}^* = 346$ μrad and $\theta_{y0}^* = 168$ μrad. Such angles prevent the capture under axial channeling regime, since $\theta_{y0}^* \approx 5\psi_1$, where ψ_1 is the critical angle for axial channeling.

In Figs. 5.15.a and .b the distributions of outgoing deflection angles and the horizontal projection are shown. The mean deflection angle $\theta_{mvr} = (47.65 \pm 0.31)$ μrad was measured. For comparison, the deflection angle for single volume reflection θ_{vr} was (10.36 ± 0.32) μrad. It was measured by alignment of the vertical angle $\theta_{y0} \gg \theta_{y0}^*$. θ_{vr} was 4.6 times smaller than θ_{mvr}, as shown in Fig. 5.15.c.

The additional deflection by skew planes is approximately fifty due to $(110)^{sk}$ and $(112)^{sk}$ planes, fifty due to weaker planes. The deflection efficiency $P_d(\theta_x < 0) = (64.73 \pm 0.31)\%$ was measured as the fraction of particles which are deflected to the opposite side of the crystal bending. The efficiency is significantly smaller than for 400 GeV/c protons [92]. Indeed, negative particles tangent to crystal planes are captured more frequently under channeling because of the strong multiple scattering [44]. The captured particles follow the crystal bending and form the distribution tail. Since channeled particles continue to suffer the strong multiple scattering by atomic nuclei, they also are rapidly dechanneled.

Simulations have been worked out with `DYNECHARM++` and are shown in Fig. 5.16 and Fig. 5.17. The deflection for the best alignment under MVROC is $\theta_{mvr,mc} = (-48.0 \pm 1.5)$ μrad and the percentage of particles deflected at $\theta_x < 0$ is $\sim 68\%$. Such values are in agreement with experimental measurements. In particular, the similar deflection angle proves that the code is capable of evaluating correctly the contribution of many planes to the total MVROC deflection angle. Simulation has been also made for volume reflection. The deflection angle for volume reflection is $\theta_{vr,mc} = (-9.5 \pm 0.3)$ μrad and the efficiency

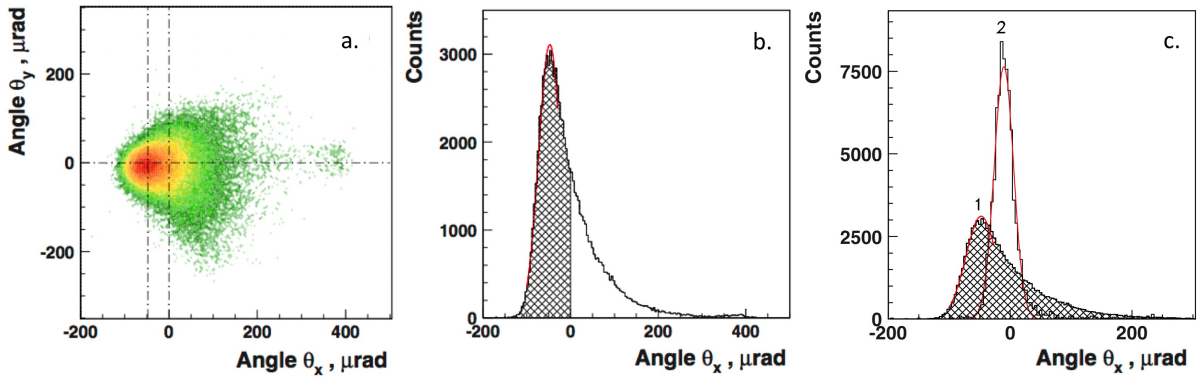

Figure 5.15: (a) Distribution of outgoing deflection angles for 150 GeV/c π^- under multiple volume reflections by different planes crossing the <111> axis in one bent Si crystal. Left dot-dashed line is the mean deflection angle $\theta_{mvr} = (47.65 \pm 0.31)$ μrad. (b) Horizontal projection of the distribution. The distribution part with θ_x¡0 (about 65%) is hatched. (c) Distribution of horizontal deflection angle distributions for 150 GeV/c π^- under multiple volume reflections by different planes crossing the <111> axis (1) and single volume reflection by (110) plane in one bent Si crystal.

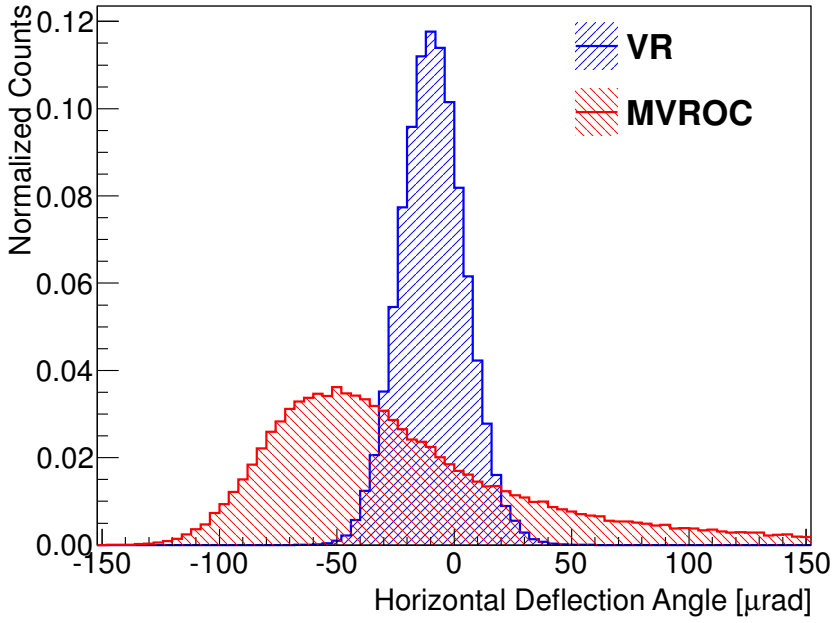

Figure 5.16: Monte Carlo simulation of the distribution of horizontal deflection angle distributions for 150 GeV/c π^- under MVROC crossing the <111> axis (red) and single volume reflection by (110) plane (blue) in one bent Si crystal.

is $\epsilon_{vr,mc} = (98 \pm 1)$ %.

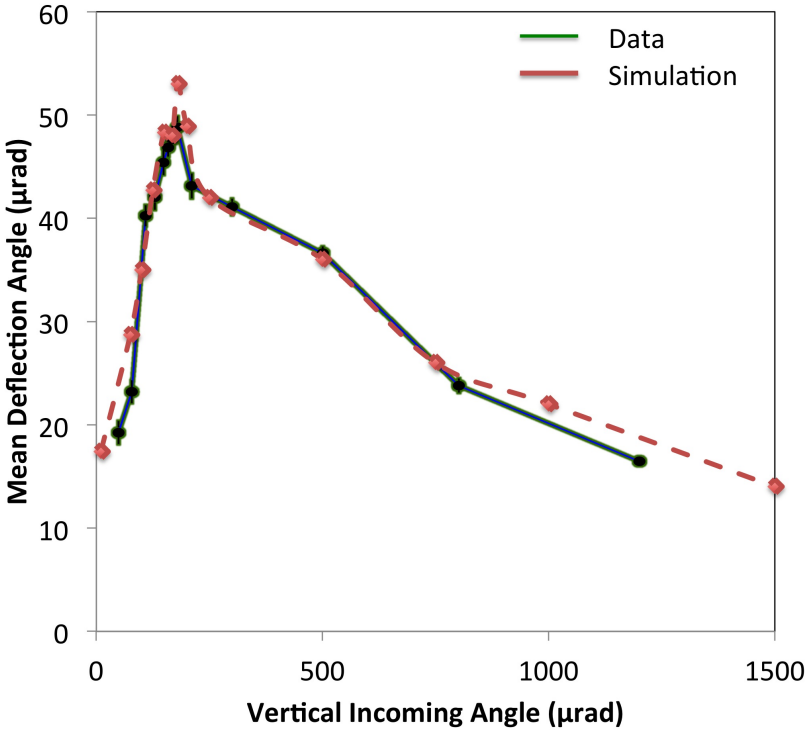

Figure 5.17: Experimental data (green) and Monte Carlo simulation (red) of the dependence of the MVROC deflection angle θ_{mvd} on the vertical incoming angle of the incident beam with the <111> axis.

Monte Carlo simulations have been used to reproduce experimental data of the mean deflection angle vs. the vertical incoming angle. The experimental data and the `DYNECHARM++` simulation are shown in Fig. 5.17. A good agreement both quantitatively and qualitatively is registered.

5.8 Deflection of sub-GeV electrons

Relevant applications for negatively charged particles have been suggested over a wide range of energies. On the very high-energy side, crystal aided collimation was proposed for beam collimation of the International Linear Collider (ILC) [168], while on the GeV energy range, which is accessible by most electron accelerators all over the world, beam steering in periodically bent crystals is interesting for the realization of innovative high-intensity and high-energy radiation sources [73, 75, 169]. Achievement of such goals does demand

greater knowledge on coherent interactions of a negative particle in the beam with the crystal.

Experiments performed with 150 GeV negative pions in last sections and Refs. [44, 45, 51, 93] demonstrated that a crystal with a length comparable with the dechanneling length (about 1 mm at that energy) allowed the achievement of axial/planar channeling up to the nominal bending of the crystal, and VR as for their positively charged counterparts [37, 38, 92].

In the GeV energy range, steering of negatively charged particles through bent crystals has never been reported mostly because of the difficulties to fabricate a bent crystal featuring a short thickness along the beam. Indeed, pioneering experiments with straight crystals [166, 170] provided a measure of the dechanneling length of GeV-electrons channeled between (110) silicon planes, which turned out to be in the range of a few tens of microns.

A proposal for a silicon crystal optimized for steering of GeV electrons was recently suggested in Ref. [151]. It consists of a plate crystal with short thickness along the beam, which is bent through quasi-mosaic effect [171] (see Fig. 5.18.a). The crystallographic orientations were chosen in order to obtain bending of (111) planes, which were used for coherent interaction with the electron beam. Thus, a silicon crystal 30.5 ± 0.5 μm thick with crystallographic orientations, as in Fig. 5.18.a was fabricated by starting with a 500 μm thick (211) Si wafer. The wafer was singulated to thin plate crystals through the so-called dicing before grinding process [172]. The crystal was mounted and mechanically bent by means of a holder at the desired bending. In order to achieve the desired bending, the crystal was mechanically bent by means of a mechanical holder. The crystal was characterized by high-resolution x-ray diffraction (Panalytical X-Pert MRD-PRO), highlighting a bending angle of 905 ± 15 μrad for the (111) planes, corresponding to a radius of 33.5 mm, i.e., 23 times the critical radius (see Fig. 5.18.a). The crystal lateral sizes were optimized to suppress parasitic anticlastic deformation across the central region of the crystal [151, 173], resulting in a cylindrical surface.

The experimental setup is sketched in Fig. 5.18.

The crystal holder was mounted on a high-precision goniometer equipped with 5 degrees of freedom. Translations along the x and y axes were used to geometrically align the crystal with the beam with an accuracy of 1 μm, while rotations around the x, y and z axes with an accuracy of 50, 9 and 175 μrad, respectively, were used to achieve angular alignment of the crystal planes with the electron beam. Care was paid in orienting the crystal far from axial channeling. An 855 MeV electron beam, available at the Mainz Microtron MAMI facility, was conditioned to a beam size of 200x70 μm^2 and a divergence of 70 and 30 μrad (less than

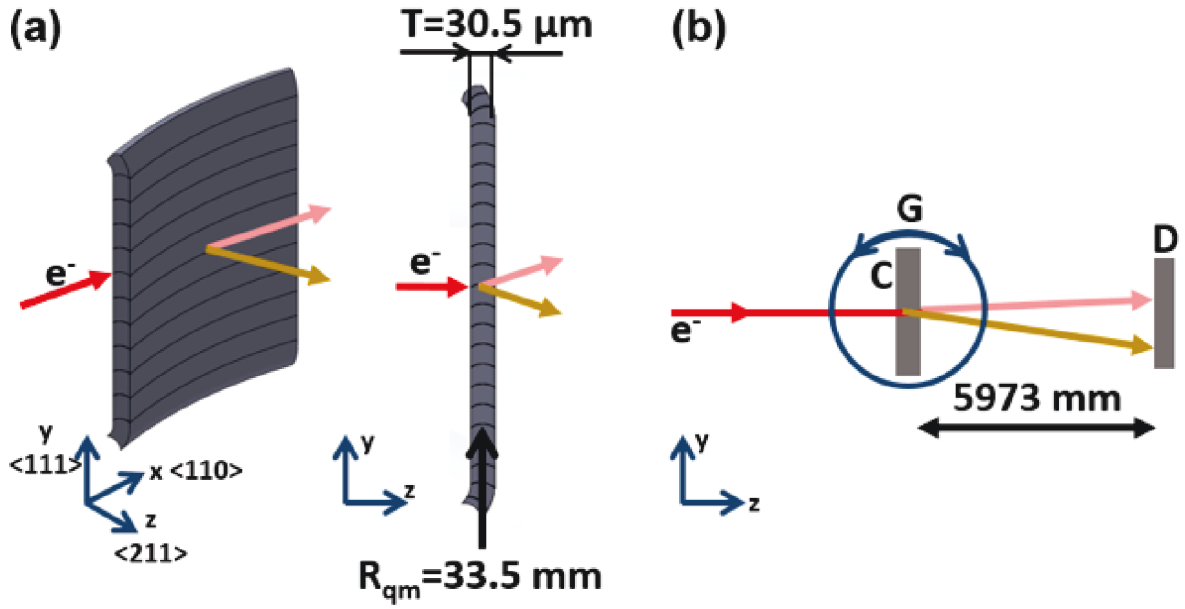

Figure 5.18: (a) Bending of a silicon plate-like crystal with properly chosen crystallographic orientations generates the quasi-mosaic effect, resulting in a secondary bending of the planes lying in the crystal thickness. (b) Sketch of the experimental setup. The red arrow indicates the incoming beam, impinging on the crystal mounted on a high-precision goniometer (G). The gold arrow indicates particles deflected thanks to planar channeling, pink arrow correspond to over-barrier particles. A silicon detector, (D), reconstructs the beam profile after interaction with the crystal.

the planar critical angle, 217 μrad at 855 MeV). A unit of the INSULAB Telescope [156] determined the beam profile after the interaction with the crystal. The detector was based on a single-sided silicon microstrip detector placed 5973 mm downstream of the crystal and contained two tiles with a lateral size of 1.92x1.92 cm^2 and a thickness of 300 μm arranged in an x-y geometry. Each tile contains 384 microstrips with a physical and readout pitch of 50 μm, allowing a spatial resolution of better than 15 μm. Data acquisition (DAQ) system was based on a custom analog-to-digital conversion (ADC) board for in-situ signal digitization and a dedicated VME readout board. The maximum DAQ rate was 3 kHz. The entire experimental setup was kept under vacuum to avoid multiple scattering of the beam by air, thus allowing an angular resolution of 70 and 30 μrad, respectively.

In order to excite coherent interactions between electrons and the crystal, the latter was rotated around the x-axis and, for each angular position, the particle distribution after interaction with the crystal was recorded. A peculiarity of this experimental scheme is the separate observation of channeled and dechanneled particles, which cannot be afforded by operating with a straight crystal.

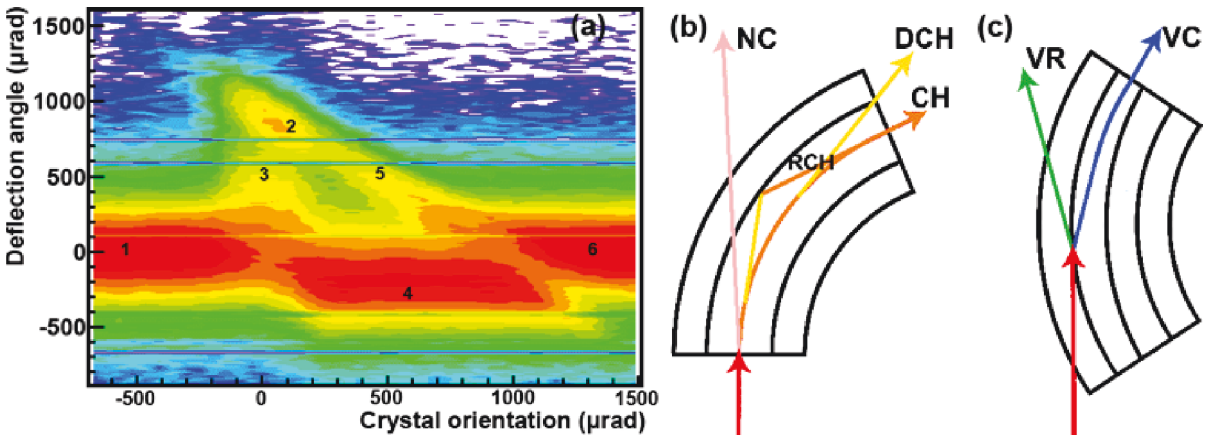

Figure 5.19: (a) an angular scan recorded during the interaction between the crystal and the 855 MeV electron beam. Six regions each, can be distinguished: (1) and (6) non-channeling regime; (2) channeling; (3) dechanneling; (4) volume reflection; and (5) volume capture. (b) The bent crystal is aligned with respect to the charged particle beam (red straight arrow) to excite planar channeling. Over-barrier particles are deflected toward the opposite side as that of crystal bending. Under-barrier particles are captured under the channeling regime (orange arrows). Due to multiple scattering, channeled particles may suffer dechanneling (yellow arrow). A fraction of dechanneled particles experiences rechanneling (RCH). (c) Bent crystal is aligned with respect to the incoming particle beam (red arrow) in such a way that the beam trajectory becomes tangent to the atomic planes inside the crystal bulk. Under such regime, either VR (green arrow) or the competitive process of volume capture (blue arrow) occurs.

Particle distribution after interaction with the crystal as a function of the crystal-beam angle is shown in Figure 5.19. This pattern very much resembles the results of a study about the interaction between a bent crystal and negative pions carried out at an energy more than two orders of magnitude higher than for this experiment [44, 93]. Fig. 5.19 also highlights that the same interaction phenomena were observed either at 150 GeV or 855 MeV. In particular, in regions (1) and (6), beam trajectory is never tangent to the crystalline planes so that coherent interactions are prevented. In region (2), the crystal is oriented for channeling, which arises as the beam impinges onto the crystal planes at an angle less than the critical angle for channeling (217 μrad). Under such conditions, particles transverse motion is governed by the interatomic potential averaged along the crystal planes. However, due to multiple scattering, channeled electrons may be subject to an increase in their transverse energy and overcome the interplanar potential barrier, resulting in dechanneling (region 3). The inverse of such a process may occur, too, i.e. a non channeled electron loses part of its transverse energy due to multiple scattering and

gets trapped in the channeling mode. This effect is referred to as rechanneling, which will be shown to play a fundamental role for efficient deflection. Aside from channeling, VR and volume capture (VC) (regions (4) and (5), respectively) manifest themselves as the trajectory of the beam becomes tangent to the bent atomic planes inside the volume of the crystal (see Fig. 2c). Particles subject to VR are reflected by the atomic planes, being deflected to the opposite side as that of crystal bending. In contrast, particles subject to VC are captured into the channeling regime inside the crystal volume. This phenomenon has an angular acceptance equal to the crystal bending angle, unlike channeling, in which the angular acceptance is limited by the critical angle.

Figure 5.20 shows beam profiles under either channeling or VR alignment (black curves) as compared with the predictions of Monte Carlo simulations (red curves). The code uses an inter-planar potential based on measured atomic form factors for Si [174] and solves the equation of motion for the electrons interacting with the crystal. More information about the code is in Ref. [175] and references therein.

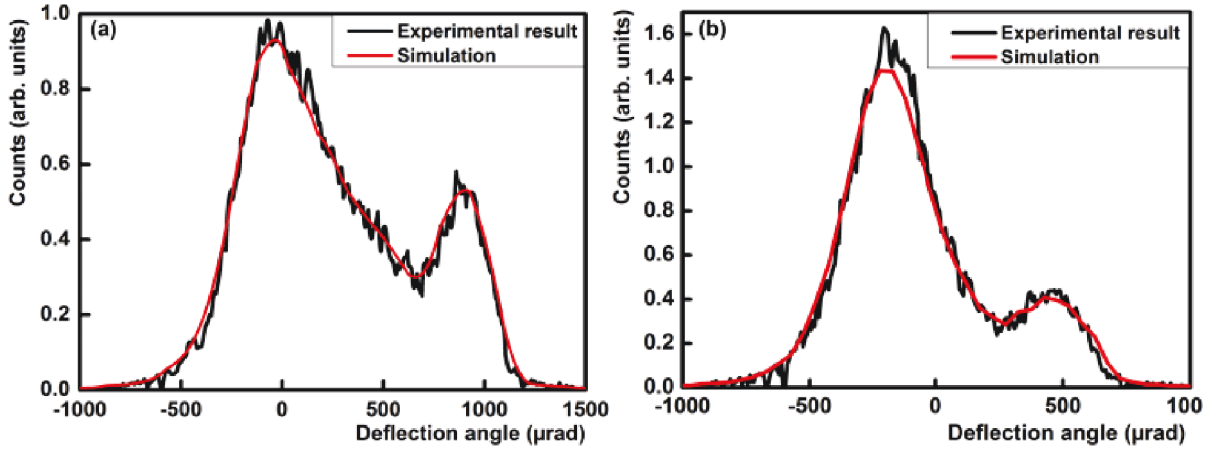

Figure 5.20: (a) Beam profile with the crystal aligned for channeling. The left peak (with maximum at ~ 20 μrad) corresponds to over-barrier particles, which are slightly deflected to the side opposite to the crystal bending, the right peak owes to channeled particles. (b) Beam profile with the crystal aligned for VR. The left peak corresponds to volume-reflected particles and the right one corresponds to particles subject to volume capture.

In Fig. 5.20.a, the peak on the right corresponds to the particles deflected under channeling. A Gaussian fit of the distribution highlights a deflection angle of 910 ± 5 μrad. The fraction of deflected particles within $\pm 3\sigma$ around the channeling peak was $20.1 \pm 1.2\%$, a value in agreement with the simulation results (21.2%). The left peak is due to deflection of over-barrier particles, whose distribution is centered to the opposite direction as that of channeling. The distribution is asymmetric because of the contribution

of rapidly dechanneled particles on the right side. The beam profile recorded for channeling was fitted as the sum of two gaussian and one exponential curves. The decay constant of the exponential term provides a direct experimental determination of the dechanneling length, which results to be 19.2 ± 1.5 μm. Fig. 5.20.b shows the deflection occurring as the crystal is oriented about on the middle of the VR region (450 μrad far from the channeling peak). A Gaussian fit to the reflected beam distribution yields a deflection angle of 191 ± 10 μrad with an efficiency of $76.7 \pm 1.\%$, in agreement with the prediction of the Monte Carlo simulation (75.8%). As expected, VR occurs with lower efficiency with respect to higher-energy experiments [37, 44], because of larger probability of competitive VC at lower energies [176]. In fact VC is aided by incoherent scattering, which favors the transition from over-barrier to channeling states, and that becomes stronger at lower energies [175].

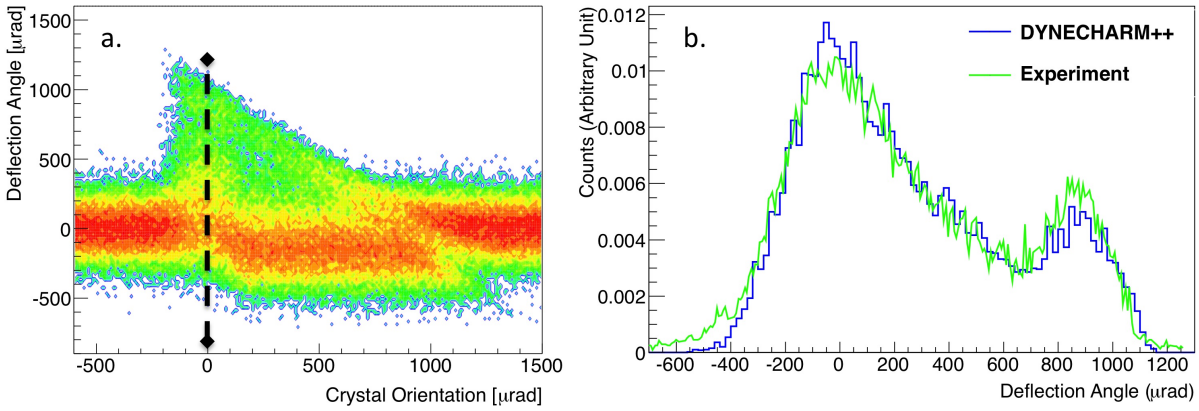

Figure 5.21: (a) Simulation with `DYNECHARM++` of the angular scan during the interaction between the crystal and the 855 MeV electron beam. (b) Simulation of beam profile highlighted with the dashed line in Fig a.. The crystal is aligned for channeling. Blue line is the simulation and green line the experimental data.

Simulation with `DYNECHARM++` have been made. In Fig. 5.21 the simulation of Figs. 5.19.a and 5.20.a and .b are shown. The efficiency is 19.5 ± 1 % and the dechanneling length 19.4 ± 1.5 μm. Scan and profile are in good agreement with experimental data. The main difference has been observed at the tails. In fact, the multiple scattering model is approximated by a simple gaussian in the code, and that is probably not sufficient for the purpose.

The simulation of the distribution of the outgoing angle has been worked out also with the Geant4 channeling code (see Fig. 5.22). The distribution is in agreement with experimental data. Channeling efficiency holds 20 ± 1 %. Dechanneling length is 17.9 ± 1.5 μm. Thus, the code is capable of selecting and tracking the channeled particles but some

improvements have to be made on the routine for the computation of the outgoing angle of channeled particles.

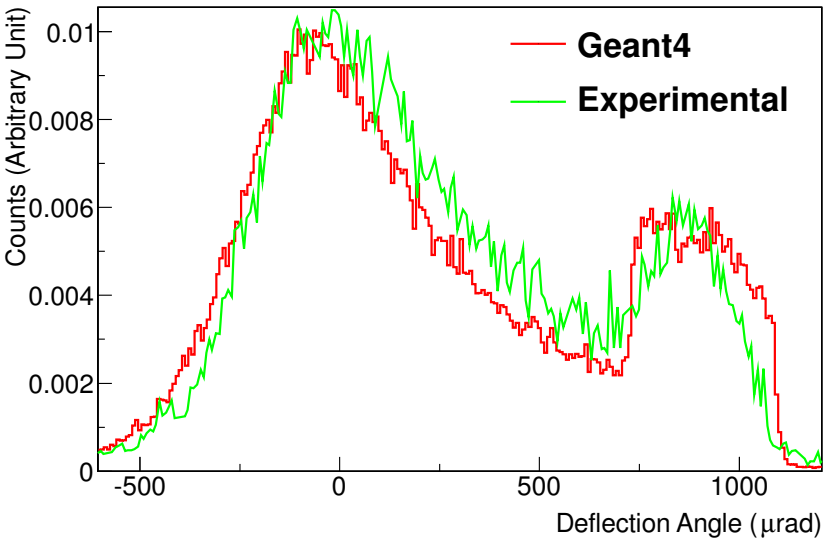

Figure 5.22: Geant4 simulation (red line) and experimental data (green line) of the distribution of deflection angle of 855 MeV/c electrons passed through a 30.5 μm long silicon crystal bent at $R = 33.5$ mm along (111) planes.

Chapter 6

Crystal collimation

6.1 Introduction

In this section the on-beam characterization procedure of the strip used for the UA9 experiment and a summary of the results obtained at the SPS for the crystal collimation are presented.

In a hadron collider, such as the Large Hadron Collider (LHC), a multi-stage collimation system is used to absorb the beam halo particles preventing quenches of its superconducting magnets and reducing the background at the experiments[177]. Halo generation is a rather complex process, resulting in a diffusive growth of the oscillation amplitudes of the particles at the edge of the beam core. The increase in amplitude per turn of halo particles is in general very small (considerably smaller than 1 μm). A primary collimator is a solid-state target, which scatters halo particles due to Coulomb scattering. Then, impact parameters are increased with a massive secondary collimator-absorber located downstream the primary collimator. However, a significant probability exists for these protons to be back scattered in the vacuum pipe and produce losses in the sensitive areas of the accelerator. Tertiary collimators are used to absorb these protons.

In principle, scattering of protons from the absorber back to the accelerator with stray trajectories should be strongly reduced if a bent crystal has been used as a primary collimator. The crystal indeed should deflect particles in channeling states and direct them onto the absorber far from its edge (see Fig. 6.1).b. This property could also be used to keep the secondary collimators at larger amplitudes, therefore minimizing their beam coupling impedance. Experiments on the beam halo collimation with short bent crystals have been firstly performed at the U-70, RHIC [112] and Tevatron [111]. In the last case, the background in the CDF experiment was reduced by using the crystal as a primary

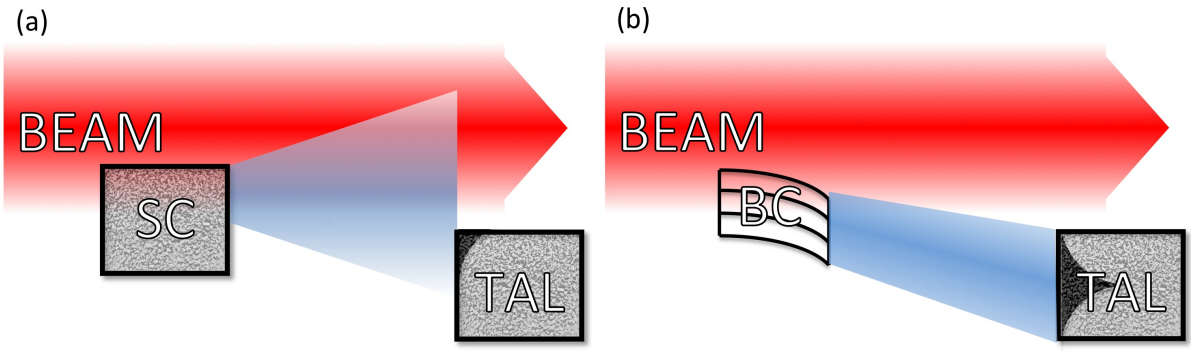

Figure 6.1: (a) Collimation scheme using a solid state primary collimator- scatterer (SC). (b) Collimation scheme with a bent crystal (BC) as a primary collimator. Halo particles are deflected and directed onto the absorber (TAL Target Aperture Limitation) far from its edge.

collimator by a factor of two with respect to what was obtained in the same conditions with a tungsten primary collimator.

The UA9 experiment is devoted to the study and the realization of a crystal-assisted collimation system for the Super Proton Synchrotron (SPS) and the Large Hadron Collider (LHC). In the past years it was proved that the alignment of the crystal under channeling condition was reproducible and fast [26]. Because channeled particles oscillate far from nuclei during their motion in the crystal, they experience less nuclear inelastic reaction than not channeled particles [13]. As a direct consequence, beam losses are strongly reduced through the adoption of a crystal-collimator system under proper channeling condition. The maximum measured reduction ratio was 20 for protons and 7 for Pb ions.

The capability of a crystal to deflect particles is a fundamental parameter for the successful collimation of a beam via orientational effects. Thus, a specific analysis procedure was developed by the Sensor and Semiconductor Laboratory of the University of Ferrara for the UA9 experiment in order to characterize the strip which were going to be installed in the SPS.

Firstly, the structural properties of the sample were characterized with Channeling Rutherford Backscattering (C-RBS) and x-ray diffraction.

C-RBS involves measuring the number and energy of ions in a MeV-beam which backscatter after colliding with the atoms in the near-surface region of a sample. By orienting the sample under channeling condition (C-RBS) it is possible to determine the crystalline quality. Indeed, under channeling the backscattering from buried atoms in the lattice are drastically reduced since these atoms are shielded from the incident ions by the atoms in the surface layers. By measuring the reduction in backscattering when a sample

is in channeling, it is possible to quantitatively measure and profile the crystal perfection.

X-ray characterization allows to highlight the presence of defects in a crystalline structure. The x-ray intensity around a Bragg's diffraction can be studied as a function of the incidence angle variation obtained by tilting the crystal, i.e. by performing, a rocking curve. Since Bragg's diffraction allows to producing intense peaks of reflected radiation at specific wavelengths and incident angles, the intensity distribution for an ideal crystal with a monochromatic x-ray beam would match the instrument resolution. If defects are present lattice planes are deformed and part of the intensity is scattered at higher or lower angle (diffuse scattering).

After the quality of the crystalline structure was certified, the strip was tested on-beam at the H8 external line of the SPS with a 400 GeV/c proton beam. The on-beam characterization allows the measurement of the main parameters of orientational effects, such as the mean deflection angle and the deflection efficiency for planar channeling.

6.2 On-beam characterization at the H8 line

6.2.1 Experimental setup

The study of channeling phenomena requires very accurate angular alignment of the silicon crystals with respect to the beam. Indeed, the critical angle for channeling is of the order of 10 μrad for 400 GeV/c protons. A charged particle telescope has been constructed by the Imperial College London group for the data taking at high rates in a CERN 400 GeV/c proton beam line. A full description of the system can be found in Ref. [178].

The objective of the system is to provide excellent angular and spatial resolution for measuring the trajectories of incident and outgoing particles. The system utilizes ten planes of Si microstrip sensors, arranged as five pairs each measuring two orthogonal coordinates, with an active area of 3.8 x 3.8 cm^2. The apparatus has a long baseline, approximately 10 m in each arm, and achieves an angular resolution in the incoming arm of 2.8 μrad and a total angular resolution on the difference of the two arms of 5.2 μrad, with performance limited by multiple scattering in the sensor layers. The Si microstrip telescope was tested in the CERN H8 beam line in September 2010. The layout of the telescope is described in Fig. 6.2.

The upstream section of the telescope for the measurement of incoming tracks is formed by planes 1 and 2 while outgoing tracks are measured using planes 3, 4 and 5. Plane 4 is a rotated XY plane (45), used in order to resolve ambiguities in reconstruction from multiple outgoing tracks. Events were triggered on the signal coincidence recorded by a

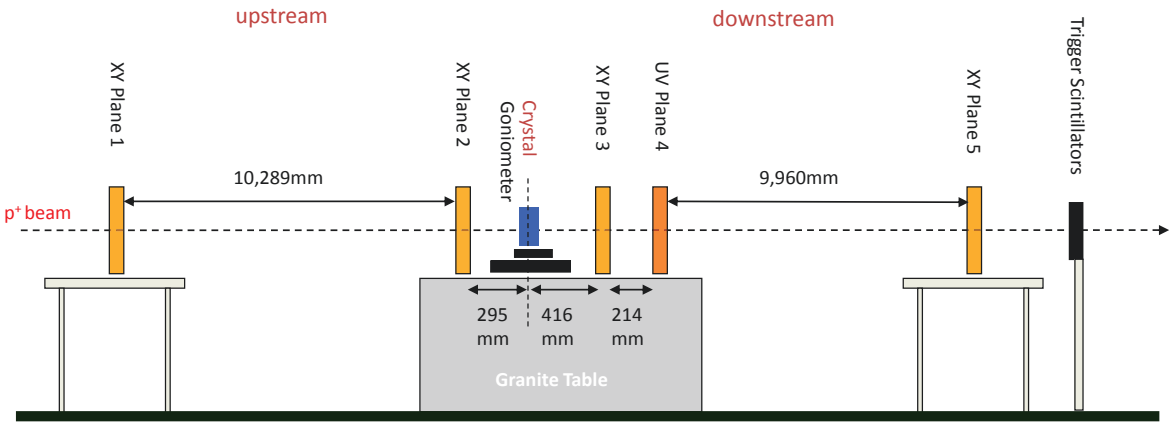

Figure 6.2: Experimental layout in the H8 beam line. The UV plane denotes the rotated (45) XY plane.

pair of plastic scintillators placed downstream the telescope.

6.2.2 Geometrical feature characterization

The relative position of the strip and the strip width were first studied to determine the range on which the analysis can be performed. The enhancement of multiple scattering due to the presence of the strip was exploited to determine the position of the strip. In fact, the strip was not aligned for channeling or volume reflection. Thus, the crystal behaved as a thin amorphous layer, causing further spreading of the beam with respect to the beam fraction which only crosses the detectors.

The distribution of the outgoing angles was analyzed for contiguous impact position at the strip entry surface. The variation of the root mean square of the distribution of the outgoing angles allows determining the position and the dimension of the crystal (see Fig.6.3).

The distance between the FWHM at the lateral edges of the strip was evaluated to determine the width of the strip, as shown in Fig.6.3).

The same procedure was adopted to characterize all the strips. The fabrication parameters of the crystal are reported in Tab. 6.1. The mean deflection angle of the strip can be evaluated as the ratio between the length and the bending radius of the strip. The height of the strip does not affect the channeling performance and the usage as a primary collimator, because the beam spot is of the order of hundreds μm. A ± 125 μm region around the center of the strip was selected for the analyses.

In Tab. 6.2 the crystalline and geometrical parameters of the strip are presented. All

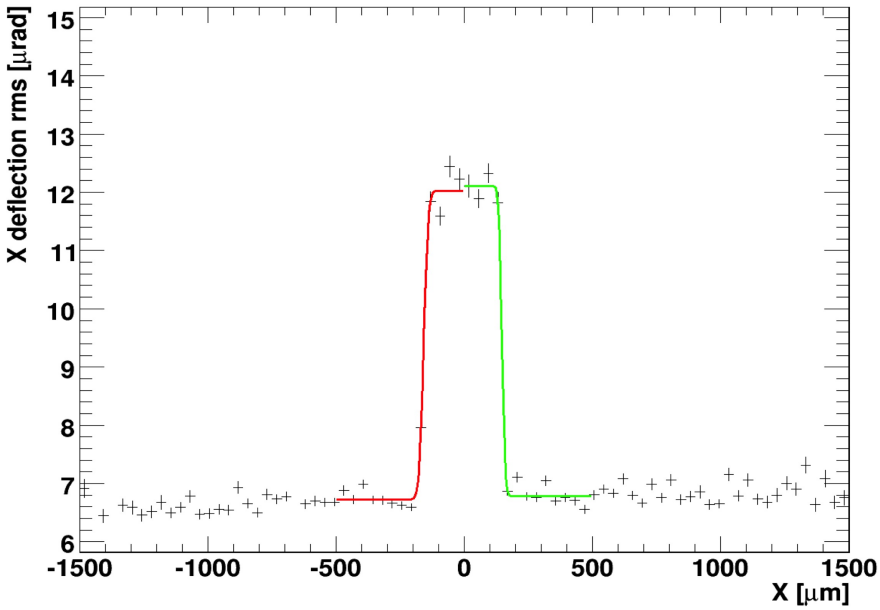

Figure 6.3: Horizontal deflection root mean square of the non channeled beam versus the horizontal hit position with statistical error bars for the ST45A strip.

Table 6.1: Fabrication parameters of the strips

Strip Name	Year	Width (mm)	Length (mm)	Height (mm)	Off axis (μrad)
STF38A	2010	1.00±0.05	1.89±0.05	55.00±0.01	100 ± 30
STF45A	2010	1.00±0.05	2.00±0.05	55.00±0.01	70 ± 30
STF47	2011	1.99±0.05	3.10±0.05	55.00±0.01	150 ± 30
STF48	2011	0.97±0.08	2.00±0.05	55.00±0.01	140 ± 30
STF49	2011	0.51±0.05	0.80±0.05	55.00±0.01	170 ± 30
STF50 (C4)	2012	1.00±0.05	2.00±0.05	55.00±0.01	170 ± 30
STF51	2012	2.00±0.05	3.00±0.05	55.00±0.01	70 ± 30

the strips exploit the (110) plane for channeling, because it allows reaching the highest deflection efficiency in Si [57]. The absence of a measurable number of defects has been determined through x-ray and cRBS. The bending radius has been computed by using the VEECO NT-1100 white-light interferometer.

6.2.3 Channeling properties characterization

The strip was aligned under channeling. Because the divergence of the beam was greater than the channeling Lindhard angle $\theta_L = 10.3$ μrad at 400 GeV/c for Si (110) plane, the

Table 6.2: Crystalline and geometrical parameters of the strips

Strip Name	Plane	Axis	Defects	Bending Radius (m)
STF38A	(110)	$< 110 >$	$< 1/\mathrm{cm}^2$	8.7±0.1
STF45A	(110)	$< 110 >$	$< 1/\mathrm{cm}^2$	12.9±0.2
STF47	(110)	$< 110 >$	$< 1/\mathrm{cm}^2$	63±1
STF48	(110)	$< 110 >$	$< 1/\mathrm{cm}^2$	14.1±0.3
STF49	(110)	$< 110 >$	$< 1/\mathrm{cm}^2$	3.3±0.2
STF50 (C4)	(110)	$< 110 >$	$< 1/\mathrm{cm}^2$	14.3±0.3
STF51	(110)	$< 110 >$	$< 1/\mathrm{cm}^2$	84.5±1.5

efficiency of deflection of planar channeling was studied as a function of the horizontal incoming angle. Such study allows the determination of the best alignment for channeling (see Fig. 6.4).

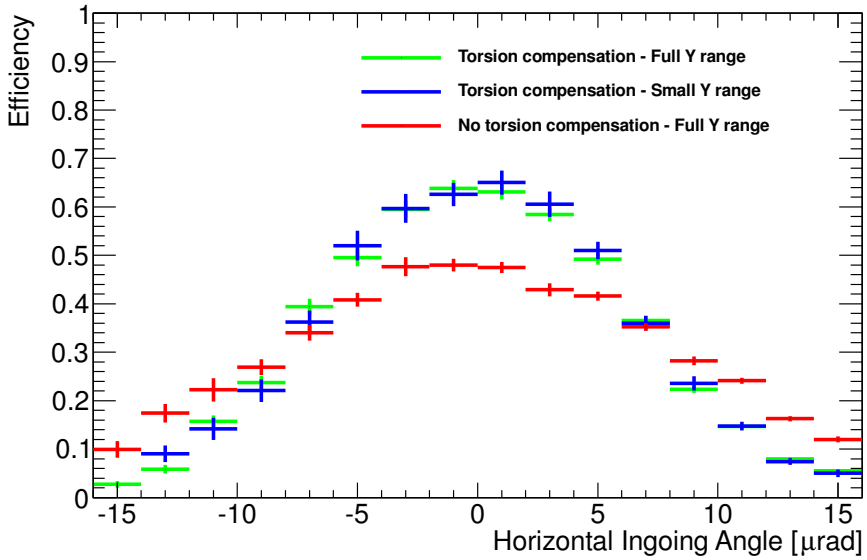

Figure 6.4: Efficiency of deflection of planar channeling as a function of horizontal incoming angle for the ST38A strip with statistical error bars. The efficiency was analyzed for a small portion of vertical impact position and for a wide portion with and without the correction for the torsion.

The presence of mechanical torsion makes the alignment of the incoming particle to the crystalline planes dependent on the vertical impact position at the strip entrance. The twist of the section perpendicular to the torque axis propagates linearly along the torque axis. Since the vertical size of the beam is of the order of hundreds μm, a twist of the order

~ 100 μrad/mm could cause an angular misalignment comparable to the critical angle for channeling and a spoiling of deflection efficiency. By selecting a narrow vertical region for the analysis, the effect of torsion on deflection efficiency can be removed, as shown in Fig. 6.4. However, such method limits the number of used data for the analysis. Therefore, a specific algorithm has been developed to compensate the presence of torsion in the analysis.

The measured incoming angle $\theta_{x,in}$ of the particles was modified depending on the vertical impact position y_{in} and the value of residual torsion τ of the strip. The modified incoming angle θ_x was evaluated by applying a shift $\theta_{x,\tau} = y_{in}\tau$ to $\theta_{x,in}$.

$$\theta_x = \theta_{x,in} + \theta_{x,\tau} = \theta_{x,in} + y_{in}\tau \tag{6.1}$$

The method allows reaching the same deflection efficiency obtained by selecting a narrow vertical region, as shown in Fig. 6.4, but it does not diminish the number of particles analyzed.

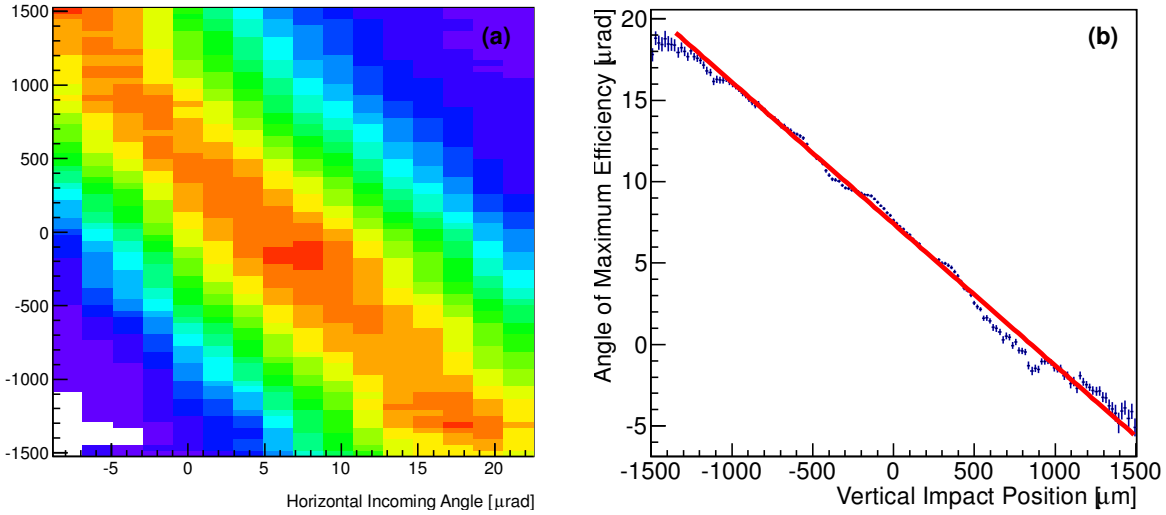

Figure 6.5: (a) Efficiency of deflection of planar channeling as a function of horizontal incoming angle and the vertical hit position for the ST38A strip with statistical error bars. If torsion is absent, the efficiency of deflection is independent from the vertical impact position. (b) Angular distribution of the maximum planar channeling efficiency as a function of the vertical impact position for the ST38A strip with statistical error bars.

The deformation due to the torsion was measured by studying the efficiency of deflection as a function of the horizontal incoming angle and vertical impact position. In Fig. 6.5.a a plot is shown for the ST38A strip. If torsion was absent, deflection efficiency would be independent of the vertical impact position. The linear correlation between the vertical impact position and the incoming angle is shown in Fig. 6.5.b for the maximum deflection

efficiency. Thus, the slope, i.e., torsion coefficient τ, was measured and applied to the analysis.

The features of channeling were studied for all the strips with the same procedure. Measured values are reported in Tab. 6.3.

Table 6.3: Channeling properties of the strips

Strip Name	Mean Deflection Angle (μrad)	Efficiency (%)	Torsion (μrad/mm)
STF38A	214.8±0.2	65±2	< 10
STF45A	144.0±0.2	74±2	< 10
STF47	31.8±0.3	64±1	< 5
STF48	141.8±0.3	40±1	< 8
STF49	246.2±0.3	32±2	< 9
STF50 (C4)	140.0±0.5	71±2	< 1
STF51	35.5±0.3	65±2	< 1

6.3 SPS experiment

A brief report of the results of the UA9 experiment for the collimation of the SPS circular accelerator are here presented.

6.3.1 Experimental setup

Fig. 6.6 shows the schematic layout of the UA9 experiment in the SPS. A complete description of the experimental setup can be found in Ref. [72]. The crystal primary collimator and the absorber stations are installed at the SPS azimuths with relative horizontal betatron phase advance close to 90 degrees and with large horizontal beta function. In the first station four singular crystals were installed. The C4 crystal was used for the measurements. The crystal was mounted on a IHEP goniometer. Such device allows rotating the crystal with an accuracy of $\sim 10\mu$rad. The alignment of the UA9 devices relative to the beam orbit was worked out by using the two-sided collimator (COL). The second station contains a 60 cm long tungsten absorber (TAL) used as a secondary collimator. The third station is in the HD area downstream the collimator-absorber.

In the interaction of the beam halo with the crystal or the absorber, particles with sufficiently large momentum offset are produced. Because of the large displacements from the design orbit, such particles can escape from the collimation area. By moving a HD

Figure 6.6: The simplified layout of the UA9 experiment. The crystal primary collimator C4 is located upstream the quadrupole QF1. The TAL acting as a secondary collimator-absorber is upstream the quadrupole QF2. Some target, SC or RP, in a high dispersion HD area is used to measure off-momentum particles produced in the collimation process. QD1 and QD2 are the defocusing quadrupoles.

target at a specific distance from the design orbit in the shadow of the TAL, off-momentum particles interact with the HD target causing the production of secondary particles. Thus, the beam loss monitors (BLM) downstream detect such secondary particles and allow the estimation of the off-momentum halo intensity. A 10 cm long bar of duralumin beam scraper (SC) and a movable 3 cm long stainless steel edge Roman pot (RP) were used as targets. The BLMs developed for LHC [179] and the scintillation telescopes described in Ref. [72] were adopted as beam loss monitors (BLM1 and BLM2 in Fig. 6.6)

In the SPS, the beams of protons or Pb ions were accelerated to 120 GeV/c or 270 GeV/c per charge with nominal betatron tunes $Q_H = 26.13$ and $Q_V = 26.18$. The average number of particles per bunch was 1.15 x 10^{11} for protons and 1.4 x 10^8 for Pb ions. The horizontal RMS emittance was $\epsilon = 0.012$ μm rad and the RMS bunch length $\sigma_t = 0.6$ ns and $\epsilon = 0.011$ μm rad and $\sigma_t = 0.55$ ns for 120 GeV/c and 270 GeV/c per charge, respectively. The relevant accelerator parameters at the azimuths of some UA9 elements are listed in Table 6.4.

Table 6.4: Beam parameters of SPS at some UA9 elements. β_x is the horizontal beta-function, σ_x is the RMS value of the horizontal beam size (here for the RMS emittance $\epsilon = 0.012$ μm rad) and $\Delta\mu_x$ is the horizontal phase advance between the elements.

Parameter	C4	TAL	SC	RP
β_x (m)	76.156	87.675	90.432	99.033
σ_x (mm)	0.956	1.026	1.042	1.09
$\Delta\mu_x$ from C4 (2π)	0	0.2475	0.4908	0.4951
D_x (m)	-0.7856	-6.4 x 10^{-4}	3.4015	3.5922

6.3.2 Protons

120 GeV/c

In Fig. 6.7 curves 1 show the dependences of beam losses observed in the crystal (a) and in the HD area target (b) on the angular position of C4 for a SPS stored beam of 120 GeV/c protons. Two scintillation telescopes were used as beam loss monitors. The observed dependences are normalized to the beam intensity and to the loss value for the amorphous orientation of the crystal. A full description of the experimental setup parameters can be found in Ref. [26].

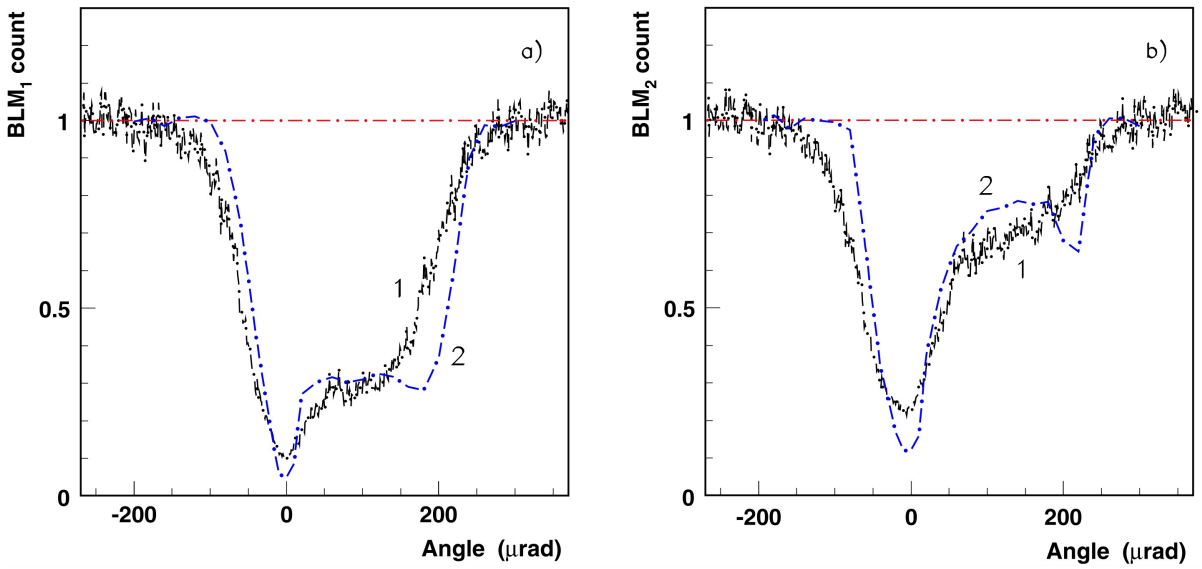

Figure 6.7: Beam of 120 GeV/c protons. Curves (1) are the dependences of beam losses observed in the crystal (a) and in the HD area target (b) on the angular position of the crystal C4 normalized to its value for the amorphous orientation of the crystal (dot-dashed line). Two scintillation telescopes were used as BLM1 in (a) and BLM2 in (b), respectively.

The curves of Figs. 6.7.a and .b are correlated. Because of inelastic interactions with the crystal nuclei are strongly suppressed for channeled particles, the loss minima are observed at the channeling angle. Thus, the beam losses in the minimum occur mainly due to the non-channeled fraction. The beam loss reduction is defined as the ratio of the losses for the amorphous and channeling orientations. A reduction $R(\mathrm{C4}) = 10$ was measured in the crystal area. Off-momentum particles collected in the HD target are part of the same non-channeled beam fraction. A reduction $R(\mathrm{HD}) = 4.5$ was measured in the HD area. The lowering of the reduction may occur because of the scattering of some particles from the TAL back to the beam.

Reduced losses are also observed in the volume reflection region next to the channeling minimum. Indeed, volume reflection allows off-momentum particles to reach the TAL aperture in a smaller number of passages through the crystal with respect to amorphous orientation. Thus, the beam losses are reduced near C4 and in the HD area. As for channeling the reduction is smaller in the HD area.

270 GeV/c

Similar experiments were performed with a SPS stored beam of 270 GeV/c protons. Due to the higher beam momentum, the critical channeling and volume reflection angles are decreased by a factor of ~ 1.5 and the angle of multiple Coulomb scattering is decreased by a factor of ~ 2.25. Thus, particles scattered by a non-oriented crystal should require a larger number of passages to reach the TAL aperture. As a consequence, the beam losses for the non-oriented crystal grow up and the loss reduction R(C4) should increase.

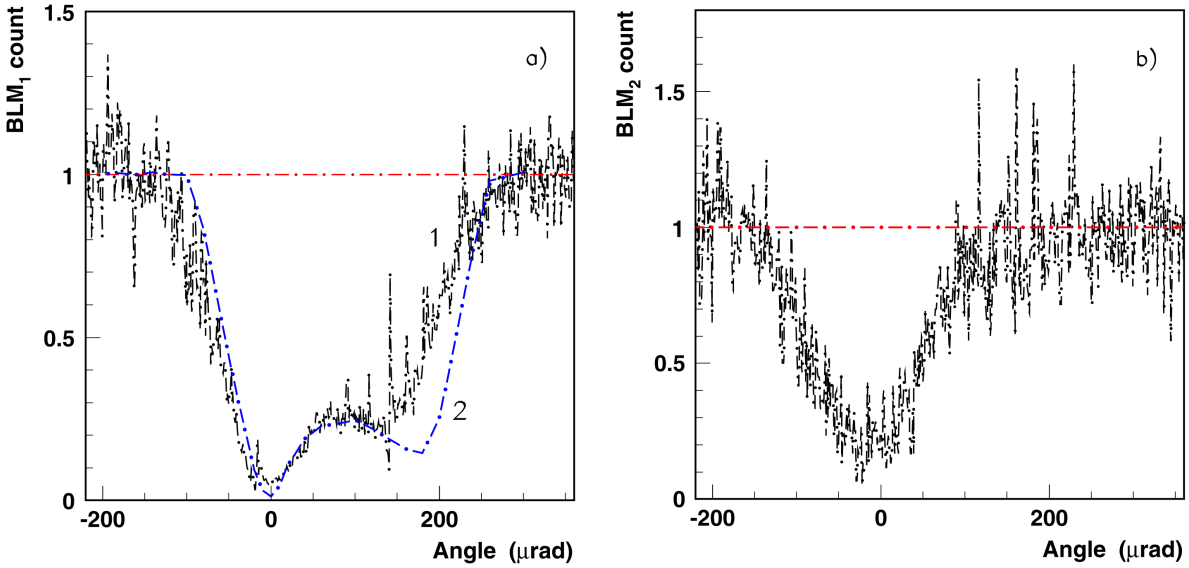

Figure 6.8: Beam of 270 GeV/c protons. The same as in Fig. 6.7. The BLMs developed for LHC were used as BLM1 in (a) and BLM2 in (b), respectively.

In Fig. 6.8 curves 1 show the dependence of beam losses observed at the crystal area (a) and at the HD target (b) on the angular alignment of C4. The crystal and the TAL collimation positions were larger than for 120 GeV/c protons. Measured reduction beam loss was R(C4) = 20 under channeling condition. The reduction is considerably larger than for 120 GeV/c protons. Such larger gap of the positions and the smaller angular kicks of multiple scatterings are probably the cause of the increase for the amorphous

crystal orientation. Thus, the ratio of the beam losses is increased. Amplitude drift of trajectories for off-momentum particles due to volume reflections [18] originates the second minimum in the VR region.

An aluminum scraper was the target in the HD area. The scraper was moved far from the orbit to avoid disturbance to the collimation. The beam loss minima of Figs. 6.8.a and .b for the crystal area and the HD target are both observed under channeling condition. The measured beam loss reduction under channeling at the HD was $R(\mathrm{HD}) = 6$. The loss reduction in the VR area is visible but considerably smaller than for 120 GeV/c protons. Such behavior may depend on the different beam momentum. In fact, because of the smaller deflection angles given by volume reflection and multiple scattering, an higher number of angular kicks is needed to reach the TAL

6.3.3 Pb ions

Experiments with a SPS stored beam of Pb ions with 270 GeV/c per charge were also carried out. The crystal channeling characteristics are determined by the ratio of $p_z = p/Z$. Thus, the same channeling properties hold for protons and Pb ions with the same p_z. However, the interactions with the crystal for protons and Pb are considerably different. As an example ionization losses scale as Z^2 [27]. The average ionization losses in 2 mm of Si for the considered energy is ~ 7 GeV, causing a strong orbit shift. As a consequence, the amplitude of oscillation increases. Debunching of Pb ions is caused by three passages through the crystal.

Curves 1 in Figs. 6.9.a and .b show the dependences of beam losses vs. the crystal orientation at the crystal area and at the HD area, respectively. A remarkable similarity has been observed. The loss reduction under channeling condition is > 7 in both cases. Such behavior highlights that the TAL contribution to the formation of the off-momentum halo is negligible for Pb ions. Indeed, most of the Pb ions should be lost in the TAL due to inelastic nuclear interactions. Measurements performed with various distances between C4 and TAL showed the existence of an optimum gap which is larger than for the optimum one for protons. Such difference is caused by the increase of oscillation amplitudes for ions due to greater ionization losses in the crystal. Therefore, the gap has to be larger to permit channeling of particles after the first unsuccessful passage through the crystal.

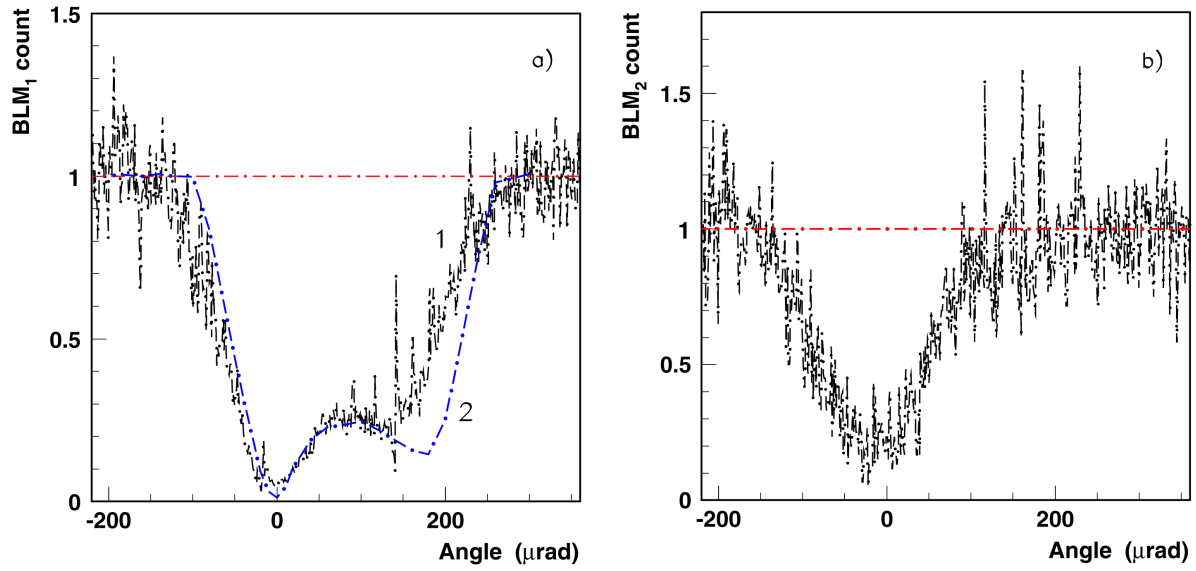

Figure 6.9: Beam of Pb ions with 270 GeV/c per charge. The same as in Fig. 6.7. Two scintillation detectors were used as BLM1 in (a) and BLM2 in (b), respectively.

Conclusions

In this thesis two Monte Carlo codes were developed for the simulation of coherent interactions between charged particles and crystals. The Monte Carlo codes were tested for comparison with the experimental results of various experiments on channeling and related topics.

The first code, named `DYNECHARM++`, is completely object-oriented and deals with numerical integration of the equation of motion to determine the trajectory of a particle in straight and bent complex crystalline structures. The electrical characteristics of the structures are computed through the ECHARM routine. A specific version suitable for high-performance computing was worked out for the new Xeon Phi coprocessors. The object-oriented nature of the code and the capability of tracking trajectories allows the addition of other packages to the simulation, such as the presence of defects and the periodic structure of a undulator.

The second code addresses the implementation of coherent effects, such as planar channeling and volume reflection to Geant4, which is a widespread used toolkit for the simulation of the passage of particles through matter. Specific models for channeling, volume reflection and dechanneling were developed for the purpose in order to limit the computation time. The implementation to Geant4 allows utilizing the physics processes constantly updated by its worldwide community of developers and users in the simulation of coherent effects.

Experiments on coherent interactions were carried out at the H8 and H4 external lines of the SPS at CERN and at the MAMI of the Johannes Gutenberg University of Mainz. The developed codes have been a useful tool for the analysis and interpretation of the results and for the prediction of new effects.

At the H8 line experiments of coherent interaction in "exotic" atomic structure and crystal configuration were worked out. A self-bent Si_xGe_{1-x} crystal was used to deflect proton via channeling and volume reflection. Multi-crystals were characterized and lined at μrad precision to enhance multi volume reflection. Bent high-efficiency Ge strips were tested

and proved to work better than Si crystals as predicted by theory. A preliminary proof of planar channeling in crystalline undulator was observed. Systematic studies on channeling efficiency were worked out for high-energy protons. Such experiments demonstrated the capability of enhancing coherent effects through innovative crystalline structures and precise mechanical inventions.

At the H4 line and at MAMI the interaction of negative particles with bent crystals was studied. A measurement of the dechanneling length of 150 GeV/c pions was carried out. Multi volume reflection in one crystal for negative particles was clearly observed for the first time. The possibility to deflect sub-GeV electrons via channeling and volume reflection in bent crystals was proved. These experiments increased the knowledge of coherent interaction for negative particles in bent crystals.

Within the UA9 experiment a procedure for the on-beam characterization of the strips for the UA9 experiment was developed. The strips were characterized at the H8 line. Main results for the collimation via channeling and volume reflection have been summarized.

Bibliography

[1] E. Tsyganov, *Some aspects of the mechanism of a charge particle penetration through a monocrystal*, Tech. Rep. (Fermilab, 1976) preprint TM-682.

[2] E. Tsyganov, *Estimates of cooling and bending processes for charged particle penetration through a mono crystal*, Tech. Rep. (Fermilab, 1976) preprint TM-684.

[3] A. Taratin and S. Vorobiev, "bibfield journal "bibinfo journal Phys. Lett. A" "textbf "bibinfo volume 119," "bibinfo pages 425 ("bibinfo year 1987"natexlaba).

[4] Y. Okazaki, M. Andreyashkin, K. Chouffani, I. Endo, R. Hamatsu, M. Iinuma, H. Kojima, Y. P. Kunashenko, M. Masuyama, T. Ohnishi, H. Okuno, Y. L. Pivovarov, T. Takahashi, and Y. Takashima, "bibfield journal "bibinfo journal Physics Letters A" "textbf "bibinfo volume 271," "bibinfo pages 110 ("bibinfo year 2000).

[5] V. A. Maisheev, ArXiv High Energy Physics - Experiment e-prints (1999), arXiv:hep-ex/9904029 .

[6] M. L. Ter-Mikaelian, *High-energy Electromagnetic Processes in Condensed Media* (Wiley, New York, 1972).

[7] L. Landau and E. Lifshitz, *The Classical Theory of Fields. Vol. 2 (4th ed.).* (Butterworth-Heinemann, 1975).

[8] A. Akhiezer and N. Shulga, *High-energy electrodynamics in matter* (Gordon & Breach, New York, 1996).

[9] V. Baier, V. Katkov, and V. Strakhovenko, *Electromagnetic Processes at High Energies in Oriented Single Crystals* (World Scientific, Singapore, 1998).

[10] A. V. Korol, A. V. Solov'yov, and W. Greiner, "bibfield journal "bibinfo journal International Journal of Modern Physics E" "textbf "bibinfo volume 13," "bibinfo pages 867 ("bibinfo year 2004).

[11] Yu A Chesnokov *et al.*, "bibfield journal "bibinfo journal Journal of Instrumentation" "textbf "bibinfo volume 3," "bibinfo pages P02005 ("bibinfo year 2008).

[12] V. Guidi, L. Bandiera, and V. Tikhomirov, “bibfield journal “bibinfo journal Phys. Rev. A“ “textbf “bibinfo volume 86,“ “bibinfo pages 042903 (“bibinfo year 2012).

[13] W. Scandale *et al.*, “bibfield journal “bibinfo journal Nucl. Instrum. Methods Phys. Res., Sect. B“ “textbf “bibinfo volume 268,“ “bibinfo pages 2655 (“bibinfo year 2010).

[14] A. F. Elishev *et al.*, “bibfield journal “bibinfo journal Phys. Lett. B“ “textbf “bibinfo volume 88,“ “bibinfo pages 387 (“bibinfo year 1979).

[15] A. G. Afonin *et al.*, “bibfield journal “bibinfo journal Phys. Rev. Lett.“ “textbf “bibinfo volume 87,“ “bibinfo pages 094802 (“bibinfo year 2001).

[16] R. A. Carrigan *et al.*, “bibfield journal “bibinfo journal Phys. Rev. ST Accel. Beams“ “textbf “bibinfo volume 5,“ “bibinfo pages 043501 (“bibinfo year 2002).

[17] R. P. Fliller *et al.*, “bibfield journal “bibinfo journal Nucl. Instrum. Methods Phys. Res., Sect. B“ “textbf “bibinfo volume 234,“ “bibinfo pages 47 (“bibinfo year 2005).

[18] W. Scandale *et al.*, “bibfield journal “bibinfo journal Phys. Lett. B“ “textbf “bibinfo volume 692,“ “bibinfo pages 78 (“bibinfo year 2010“natexlaba).

[19] A.S. Denisov *et al.*, “bibfield journal “bibinfo journal Nucl. Instrum. Methods Phys. Res., Sect. B“ “textbf “bibinfo volume 69,“ “bibinfo pages 382 (“bibinfo year 1992).

[20] S. Baricordi *et al.*, “bibfield journal “bibinfo journal J. Phys. D“ “textbf “bibinfo volume 41,“ “bibinfo pages 245501 (“bibinfo year 2008).

[21] S. Baricordi *et al.*, “bibfield journal “bibinfo journal Applied Phys. Lett.“ “textbf “bibinfo volume 91,“ “bibinfo eid 061908 (“bibinfo year 2007).

[22] A. Mazzolari *et al.*, Proc. of 1st International Particle Accelerator Conference: IPAC’10 , TUPEC080 (2010).

[23] W. Scandale *et al.*, *LHC Collimation with Bent Crystals - LUA9*, Tech. Rep. CERN-LHCC-2011-007. LHCC-I-019 (CERN, Geneva, 2011).

[24] A. Rakotozafindrabe *et al.*, *Ultra-relativistic heavy-ion physics with AFTER@LHC*, Tech. Rep. arXiv:1211.1294. SLAC-PUB-15270 (2012).

[25] J. P. Lansberg *et al.*, *Prospectives for A Fixed-Target ExpeRiment at the LHC:AFTER@LHC*, Tech. Rep. arXiv:1212.3450. SLAC-PUB-15304 (2012).

[26] W. Scandale *et al.*, “bibfield journal “bibinfo journal Phys. Lett. B“ “textbf “bibinfo volume 714,“ “bibinfo pages 231 (“bibinfo year 2012).

[27] W. Scandale *et al.*, “bibfield journal “bibinfo journal Phys. Lett. B“ “textbf “bibinfo volume 703,“ “bibinfo pages 547 (“bibinfo year 2011“natexlabb).

[28] M. T. Robinson and O. S. Oen, “bibfield journal “bibinfo journal Phys. Rev.“ “textbf “bibinfo volume 132,“ “bibinfo pages 2385 (“bibinfo year 1963).

[29] G. R. Piercy *et al.*, “bibfield journal “bibinfo journal Phys. Rev. Lett.“ “textbf “bibinfo volume 10,“ “bibinfo pages 399 (“bibinfo year 1963).

[30] J. Lindhard, Danske Vid. Selsk. Mat. Fys. Medd. **34**, 14 (1965).

[31] P. Smulders and D. Boerma, Nucl. Instrum. Methods Phys. Res., Sect. B **29**, 471 (1987).

[32] X. Artru, “bibfield journal “bibinfo journal Nucl. Instrum. Methods Phys. Res., Sect. B“ “textbf “bibinfo volume 48,“ “bibinfo pages 278 (“bibinfo year 1990).

[33] A. Taratin, Physics of Particles and Nuclei **29**, 437 (1998).

[34] V. M. Biryukov, “bibfield journal “bibinfo journal Phys. Rev. E“ “textbf “bibinfo volume 51,“ “bibinfo pages 3522 (“bibinfo year 1995“natexlaba).

[35] Babaev, A. and Dabagov, S.B., “bibfield journal “bibinfo journal Eur. Phys. J. Plus“ “textbf “bibinfo volume 127,“ “bibinfo pages 62 (“bibinfo year 2012).

[36] Yu. M. Ivanov *et al.*, “bibfield journal “bibinfo journal Phys. Rev. Lett.“ “textbf “bibinfo volume 97,“ “bibinfo pages 144801 (“bibinfo year 2006).

[37] W. Scandale *et al.*, “bibfield journal “bibinfo journal Phys. Rev. Lett.“ “textbf “bibinfo volume 98,“ “bibinfo pages 154801 (“bibinfo year 2007).

[38] W. Scandale *et al.*, “bibfield journal “bibinfo journal Phys. Rev. Lett.“ “textbf “bibinfo volume 101,“ “bibinfo pages 234801 (“bibinfo year 2008“natexlaba).

[39] W. Scandale *et al.*, “bibfield journal “bibinfo journal Phys. Lett. B“ “textbf “bibinfo volume 658,“ “bibinfo pages 109 (“bibinfo year 2008“natexlabb).

[40] W. Scandale *et al.*, “bibfield journal “bibinfo journal Phys. Rev. Lett.“ “textbf “bibinfo volume 102,“ “bibinfo pages 084801 (“bibinfo year 2009“natexlaba).

[41] W. Scandale *et al.*, “bibfield journal “bibinfo journal Phys. Rev. ST Accel. Beams“ “textbf “bibinfo volume 11,“ “bibinfo pages 063501 (“bibinfo year 2008“natexlabc).

[42] Scandale, W. *et al.*, “bibfield journal “bibinfo journal Phys. Rev. A“ “textbf “bibinfo volume 79,“ “bibinfo pages 012903 (“bibinfo year 2009).

[43] W. Scandale *et al.*, “bibfield journal “bibinfo journal Phys. Lett. B“ “textbf “bibinfo volume 680,“ “bibinfo pages 129 (“bibinfo year 2009“natexlabb).

[44] W. Scandale *et al.*, “bibfield journal “bibinfo journal Phys. Lett. B“ “textbf “bibinfo volume 681,“ “bibinfo pages 233 (“bibinfo year 2009“natexlabc).

[45] W. Scandale *et al.*, “bibfield journal “bibinfo journal Phys. Lett. B“ “textbf “bibinfo volume 680,“ “bibinfo pages 301 (“bibinfo year 2009“natexlabd).

[46] W. Scandale *et al.*, “bibfield journal “bibinfo journal Phys. Lett. B“ “textbf “bibinfo volume 688,“ “bibinfo pages 284 (“bibinfo year 2010“natexlabb).

[47] W. Scandale *et al.*, “bibfield journal “bibinfo journal Phys. Lett. B“ “textbf “bibinfo volume 693,“ “bibinfo pages 545 (“bibinfo year 2010).

[48] W. Scandale *et al.*, “bibfield journal “bibinfo journal Phys. Lett. B“ “textbf “bibinfo volume 701,“ “bibinfo pages 180 (“bibinfo year 2011“natexlabc).

[49] D. De Salvador *et al.*, “bibfield journal “bibinfo journal Applied Phys. Lett.“ “textbf “bibinfo volume 98,“ “bibinfo eid 234102 (“bibinfo year 2011).

[50] E Bagli *et al.*, “bibfield journal “bibinfo journal Journal of Instrumentation“ “textbf “bibinfo volume 7,“ “bibinfo pages P04002 (“bibinfo year 2012).

[51] W. Scandale*et al.*, “bibfield journal “bibinfo journal Physics Letters B“ “textbf “bibinfo volume 719,“ “bibinfo pages 70 (“bibinfo year 2013).

[52] E. Bagli *et al.*, “bibfield journal “bibinfo journal Phys. Rev. Lett.“ “textbf “bibinfo volume 110,“ “bibinfo pages 175502 (“bibinfo year 2013).

[53] L. Celano *et al.*, “bibfield journal “bibinfo journal Nucl. Instrum. Methods Phys. Res., Sect. A“ “textbf “bibinfo volume 381,“ “bibinfo pages 49 (“bibinfo year 1996).

[54] S. Hasan, “bibfield journal “bibinfo journal Nucl. Instrum. Methods Phys. Res., Sect. A“ “textbf “bibinfo volume 617,“ “bibinfo pages 449 (“bibinfo year 2010), 11th Pisa Meeting on Advanced Detectors - Proc. of the 11th Pisa Meeting on Advanced Detectors.

[55] P. Schoofs, F. Cerutti, A. Ferrari, and G. Smirnov, “bibfield journal “bibinfo journal Nuclear Instruments and Methods in Physics Research Section B: Beam Interactions with Materials and Atoms“ “textbf “bibinfo volume 309,“ “bibinfo pages 115 (“bibinfo year 2013).

[56] A. Ferrari, P. R. Sala, A. Fass, and J. Ranft, *FLUKA: A multi-particle transport code (program version 2005)* (CERN, Geneva, 2005).

[57] V. M. Biryukov, Y. A. Chesnekov, and V. I. Kotov, *Crystal Channeling and Its Applications at High-Energy Accelerators* (Springer, 1996).

[58] J. Stark, Phys. Zs. **13**, 973 (1912).

[59] V.A. Andreev *et al.*, Pis'ma v Zh. Eksp. Teor. Fiz. **36**, 340 (1982).

[60] V.A. Andreev *et al.*, Pis'ma v Zh. Eksp. Teor. Fiz. **38**, 58 (1984).

[61] V.A. Andreev *et al.*, Pis'ma v Zh. Eksp. Teor. Fiz. **44**, 101 (1986).

[62] G. Moliére, Z. Naturforsch. A **2**, 133 (1947).

[63] R. J. Carrigan and J. Ellison, *Relativistic Channeling* (Plenum Press, 1987).

[64] W. Leo, *Techniques for nuclear and particle physics experiments* (Springer-Verlag, Second Revised Edition, 1987).

[65] G. Arduini *et al.*, "bibfield journal "bibinfo journal Physics Letters B" "textbf "bibinfo volume 422," "bibinfo pages 325 ("bibinfo year 1998).

[66] J.F. Bak *et al.*, "bibfield journal "bibinfo journal Nuclear Physics B" "textbf "bibinfo volume 242," "bibinfo pages 1 ("bibinfo year 1984).

[67] W.M. Gibson *et al.*, "bibfield journal "bibinfo journal Nucl. Instrum. Methods Phys. Res., Sect. B" "textbf "bibinfo volume 2," "bibinfo pages 54 ("bibinfo year 1984).

[68] V. V. Beloshitsky, M. A. Kumakhov, and V. A. Muralev, "bibfield journal "bibinfo journal Radiation Effects" "textbf "bibinfo volume 13," "bibinfo pages 9 ("bibinfo year 1972), http://www.tandfonline.com/doi/pdf/10.1080/00337577208231156 .

[69] L. Feldman, J. Mayer, and S. Picraux, *Materials analysis by ion channeling* (Academic Press, 1982).

[70] H. Esbensen *et al.*, "bibfield journal "bibinfo journal Nuclear Physics B" "textbf "bibinfo volume 127," "bibinfo pages 281 ("bibinfo year 1977).

[71] J.F. Bak *et al.*, "bibfield journal "bibinfo journal Nuclear Physics A" "textbf "bibinfo volume 389," "bibinfo pages 533 ("bibinfo year 1982).

[72] W. Scandale *et al.*, "bibfield journal "bibinfo journal Journal of Instrumentation" "textbf "bibinfo volume 6," "bibinfo pages T10002 ("bibinfo year 2011"natexlabd).

[73] V. Baryshevsky, I. Dubovskaya, and A. Grubich, "bibfield journal "bibinfo journal Phys. Lett. A" "textbf "bibinfo volume 77," "bibinfo pages 61 ("bibinfo year 1980).

[74] V. Kaplin, S. Plotnikov, and S. Vorobiev, Zh. Tekh. Fiz. **50**, 1079 (1980).

[75] Mehdi Tabrizi *et al.*, "bibfield journal "bibinfo journal Phys. Rev. Lett." "textbf "bibinfo volume 98," "bibinfo pages 164801 ("bibinfo year 2007).

[76] X. Artru *et al.*, "bibfield journal "bibinfo journal Phys. Rev. ST Accel. Beams" "textbf "bibinfo volume 6," "bibinfo pages 091003 ("bibinfo year 2003).

[77] M. Satoh *et al.*, "bibfield journal "bibinfo journal Nucl. Instrum. Methods Phys. Res., Sect. B" "textbf "bibinfo volume 227," "bibinfo pages 3 ("bibinfo year 2005), radiation from Relativistic Electrons in Periodic Structures (RREPS'03).

[78] R. A. J. Carrigan, “bibfield journal “bibinfo journal International Journal of Modern Physics A“ “textbf “bibinfo volume 25S1,“ “bibinfo pages 55 (“bibinfo year 2010).

[79] E. Bagli, V. Guidi, and V. A. Maisheev, “bibfield journal “bibinfo journal Phys. Rev. E“ “textbf “bibinfo volume 81,“ “bibinfo pages 026708 (“bibinfo year 2010“natexlaba).

[80] D. S. Gemmell, “bibfield journal “bibinfo journal Rev. Mod. Phys.“ “textbf “bibinfo volume 46,“ “bibinfo pages 129 (“bibinfo year 1974).

[81] M. Kitagawa and Y. H. Ohtsuki, “bibfield journal “bibinfo journal Phys. Rev. B“ “textbf “bibinfo volume 8,“ “bibinfo pages 3117 (“bibinfo year 1973).

[82] H. Nitta and Y. H. Ohtsuki, “bibfield journal “bibinfo journal Phys. Rev. B“ “textbf “bibinfo volume 38,“ “bibinfo pages 4404 (“bibinfo year 1988).

[83] A. Taratin and S. Vorobiev, “bibfield journal “bibinfo journal Nucl. Instrum. Methods Phys. Res., Sect. B“ “textbf “bibinfo volume 47,“ “bibinfo pages 247 (“bibinfo year 1990).

[84] A. Baurichter *et al.*, “bibfield journal “bibinfo journal Nuclear Instruments and Methods in Physics Research Section B: Beam Interactions with Materials and Atoms“ “textbf “bibinfo volume 164-165,“ “bibinfo pages 27 (“bibinfo year 2000).

[85] Akhiezer A. I., Akhiezer I. A. and Shul’ga, N.F., Sov. Phys. Journal of Experimental and Theoretical Physics **49**, 631 (1979).

[86] Shul’ga, N.F., Journal of Experimental and Theoretical Physics Letters **32**, 166 (1980).

[87] A. I. Akhiezer and N. F. Shul’ga, “bibfield journal “bibinfo journal Soviet Physics Uspekhi“ “textbf “bibinfo volume 25,“ “bibinfo pages 541 (“bibinfo year 1982).

[88] A. Taratin and S. Vorobiev, “bibfield journal “bibinfo journal Nucl. Instrum. Methods Phys. Res., Sect. B“ “textbf “bibinfo volume 26,“ “bibinfo pages 512 (“bibinfo year 1987“natexlabb).

[89] Y. Chesnokov, N. Galyaev, V. Kotov, S. Tsarik, and V. Zapolsky, “bibfield journal “bibinfo journal Nuclear Instruments and Methods in Physics Research Section B: Beam Interactions with Materials and Atoms“ “textbf “bibinfo volume 69,“ “bibinfo pages 247 (“bibinfo year 1992).

[90] N. Shul’ga, V. Truten, V. Boyko, and A. Esaulov, “bibfield journal “bibinfo journal Physics Letters A“ “textbf “bibinfo volume 376,“ “bibinfo pages 2617 (“bibinfo year 2012).

[91] A. M. Taratin and S. A. Vorobiev, “bibfield journal “bibinfo journal physica status solidi (b)“ “textbf “bibinfo volume 133,“ “bibinfo pages 511 (“bibinfo year 1986).

[92] W. Scandale *et al.*, “bibfield journal “bibinfo journal Physics Letters B“ “textbf “bibinfo volume 682,“ “bibinfo pages 274 (“bibinfo year 2009“natexlabe).

[93] W. Scandale *et al.*, “bibfield journal “bibinfo journal EPL (Europhysics Letters)“ “textbf “bibinfo volume 93,“ “bibinfo pages 56002 (“bibinfo year 2011“natexlabe).

[94] C. Erginsoy, Phys. Rev. Lett. **15**, 360 (1965).

[95] B. R. Appleton, C. Erginsoy, and W. M. Gibson, Phys. Rev. **161**, 330 (1967).

[96] W. K. Chu, W. R. Allen, S. T. Picraux, and J. A. Ellison, Phys. Rev. B **42**, 5923 (1990).

[97] S. Bellucci and V. A. Maisheev, Phys. Rev. B **71**, 174105 (2005).

[98] V. Maisheev, V. Mikhalev, and A. Frolov, Phys. JETP **74**, 740 (1992).

[99] V. Maisheev, Nucl. Instrum. Methods Phys. Res. B **119**, 42 (1996).

[100] S. Bellucci and V. Maisheev, Nucl. Instrum. Methods Phys. Res. B **234**, 87 (2004).

[101] D. Cromer and J. Waber, Acta Cryst. **18**, 104 (1965).

[102] D. Cromer and J. Waber, Acta Cryst. **19**, 224 (1965).

[103] G. Gottardi, *Natural Zeolites* (Springer-Verlag, Berlin, 1985).

[104] R. González-Arrabal, V. Khodyrev, N. Gordillo, G. Garca, and D. Boerma, Nuclear Instruments and Methods in Physics Research Section B: Beam Interactions with Materials and Atoms **249**, 65 (2006).

[105] W. Meier, Z. Kristallogr. **115**, 439 (1961).

[106] A. Alberti, American Mineralogist **64**, 1188 (1979).

[107] R. Brun and F. Rademakers, “bibfield journal “bibinfo journal Nucl. Instrum. Methods Phys. Res., Sect. A“ “textbf “bibinfo volume 389,“ “bibinfo pages 81 (“bibinfo year 1997), new Computing Techniques in Physics Research V.

[108] OpenMP Architecture Review Board, “enquote “bibinfo title OpenMP application program interface version 3.1,“ (2011).

[109] S. Bellucci *et al.*, “bibfield journal “bibinfo journal Phys. Rev. ST Accel. Beams“ “textbf “bibinfo volume 7,“ “bibinfo pages 023501 (“bibinfo year 2004).

[110] E. Bagli, V. Guidi, and V. A. Maisheev, Proc. of 1st International Particle Accelerator Conference: IPAC'10 , TUPEA070 (2010).

[111] V. D. Shiltsev *et al.*, Proc. of 1st International Particle Accelerator Conference: IPAC'10 , TUOAMH03 (2010).

[112] R. P. Fliller *et al.*, "bibfield journal "bibinfo journal Phys. Rev. ST Accel. Beams" "textbf "bibinfo volume 9," "bibinfo pages 013501 ("bibinfo year 2006).

[113] V. L. Highland, "bibfield journal "bibinfo journal Nuclear Instruments and Methods" "textbf "bibinfo volume 129," "bibinfo pages 497 ("bibinfo year 1975).

[114] V N Ivanchenko *et al.*, Journal of Physics: Conference Series **219**, 032045 (2010).

[115] C. Kittel, *Introduction to Solid State Physics (7th ed.).* (John Wiley & Sons, 1996).

[116] V. M. Biryukov, "bibfield journal "bibinfo journal Phys. Rev. E" "textbf "bibinfo volume 52," "bibinfo pages 2045 ("bibinfo year 1995"natexlabb).

[117] M. J. Hytch, J.-L. Putaux, and J.-M. Penisson, "bibfield journal "bibinfo journal Nature" "textbf "bibinfo volume 423," "bibinfo pages 270 ("bibinfo year 2003).

[118] J. P. Hirth and J. Lothe, *Theory of Dislocations vol. 1 (2nd edn)* (Wiley, New York, 1982).

[119] V.M. Biryukov *et al.*, "bibfield journal "bibinfo journal Nucl. Instrum. Methods Phys. Res., Sect. B" "textbf "bibinfo volume 86," "bibinfo pages 245 ("bibinfo year 1994).

[120] V. A. Maisheev, "bibfield journal "bibinfo journal Phys. Rev. ST Accel. Beams" "textbf "bibinfo volume 10," "bibinfo pages 084701 ("bibinfo year 2007).

[121] W. T. Scott, "bibfield journal "bibinfo journal Rev. Mod. Phys." "textbf "bibinfo volume 35," "bibinfo pages 231 ("bibinfo year 1963).

[122] G. R. Lynch and O. I. Dahl, "bibfield journal "bibinfo journal Nucl. Instrum. Methods Phys. Res., Sect. B" "textbf "bibinfo volume 58," "bibinfo pages 6 ("bibinfo year 1991).

[123] W. Scandale *et al.*, "bibfield journal "bibinfo journal Phys. Rev. Lett." "textbf "bibinfo volume 101," "bibinfo pages 164801 ("bibinfo year 2008"natexlabd).

[124] J. J. Pluth and J. V. Smith, American Mineralogist **75**, 501 (1990).

[125] W. Scandale *et al.*, "bibfield journal "bibinfo journal Phys. Lett. B" "textbf "bibinfo volume 660," "bibinfo pages 610 ("bibinfo year 2008"natexlabe).

[126] Intel, "The intel xeon phi product family," www.intel.com/content/dam/www/public/us/en/docu
briefs/high-performance-xeon-phi-coprocessor-brief.pdf.

[127] A. Valles, "Performance insights to intel hyper-threading technology," software.intel.com/en-us/articles/performance-insights-to-intel-hyper-threading-technology.

[128] A. Vladimirov, "bibfield journal "bibinfo journal Intel Technology Journal" "textbf "bibinfo volume 6," "bibinfo pages 11 ("bibinfo year 2002).

[129] S. Casey, "How to determine the effectiveness of hyper-threading technology with an application," software.intel.com/en-us/articles/how-to-determine-the-effectiveness-of-hyper-threading-technology-with-an-application.

[130] A. Vladimirov, *Auto-Vectorization with the Intel Compilers: is Your Code Ready for Sandy Bridge and Knights Corner?*, Tech. Rep. (Colfax International, 2012).

[131] M. Sabahi, "A guide to auto-vectorization with intel c++ compilers," http://software.intel.com/en-us/articles/a-guide-to-auto-vectorization-with-intel-c-compilers.

[132] S. Agostinelli *et al.*, "bibfield journal "bibinfo journal Nuclear Instruments and Methods in Physics Research Section A: Accelerators, Spectrometers, Detectors and Associated Equipment" "textbf "bibinfo volume 506," "bibinfo pages 250 ("bibinfo year 2003).

[133] M. Gallas *et al.*, in "emph "bibinfo booktitle Astroparticle, Particle and Space Physics, Detectors and Medical Physics Applications, Proceedings of the 9th Conference (2005) Chap. 90, pp. 551–555.

[134] G.G.P. Cirrone *et al.*, in "emph "bibinfo booktitle Nuclear Science Symposium Conference Record (NSS/MIC), 2009 IEEE (2009) pp. 4186–4189.

[135] G. Santin, V. Ivanchenko, H. Evans, P. Nieminen, and E. Daly, "bibfield journal "bibinfo journal Nuclear Science, IEEE Transactions on" "textbf "bibinfo volume 52," "bibinfo pages 2294 ("bibinfo year 2005).

[136] S. Incerti *et al.*, "bibfield journal "bibinfo journal International Journal of Modeling, Simulation, and Scientific Computing" "textbf "bibinfo volume 01," "bibinfo pages 157 ("bibinfo year 2010), http://www.worldscientific.com/doi/pdf/10.1142/S1793962310000122 .

[137] B. Rossi and K. Greisen, "bibfield journal "bibinfo journal Rev. Mod. Phys." "textbf "bibinfo volume 13," "bibinfo pages 240 ("bibinfo year 1941).

[138] E. Bagli and V. Guidi, "bibfield journal "bibinfo journal Nuclear Instruments and Methods in Physics Research Section B: Beam Interactions with Materials and Atoms" "textbf "bibinfo volume 309," "bibinfo pages 124 ("bibinfo year 2013).

[139] K. Elsener *et al.*, "bibfield journal "bibinfo journal Nucl. Instrum. Methods Phys. Res., Sect. B" "textbf "bibinfo volume 119," "bibinfo pages 215 ("bibinfo year 1996).

[140] V. Guidi, L. Lanzoni, and A. Mazzolari, "bibfield journal "bibinfo journal Journal of Applied Physics" "textbf "bibinfo volume 107," "bibinfo eid 113534 ("bibinfo year 2010).

[141] V. Carassiti, P. Dalpiaz, V. Guidi, A. Mazzolari, and M. Melchiorri, "bibfield journal "bibinfo journal Review of Scientific Instruments" "textbf "bibinfo volume 81," "bibinfo eid 066106 ("bibinfo year 2010).

[142] J. Czochralski, Zeitschrift fur physikalische Chemie **92**, 219 (1918).

[143] N. V. Abrosimov *et al.*, "bibfield journal "bibinfo journal Journal of Crystal Growth" "textbf "bibinfo volume 166," "bibinfo pages 657 ("bibinfo year 1996).

[144] N. V. Abrosimov *et al.*, "bibfield journal "bibinfo journal Journal of Crystal Growth" "textbf "bibinfo volume 174," "bibinfo pages 182 ("bibinfo year 1997).

[145] R. Smither *et al.*, "bibfield journal "bibinfo journal Review of Scientific Instruments" "textbf "bibinfo volume 76," "bibinfo eid 123107 ("bibinfo year 2005).

[146] N. V. Abrosimov, Proc. of the Focusing Telescopes in Nuclear Astrophysics Conference , 185 (2006).

[147] D. G. de Kerckhove *et al.*, "bibfield journal "bibinfo journal Applied Phys. Lett." "textbf "bibinfo volume 74," "bibinfo pages 227 ("bibinfo year 1999).

[148] M.B.H Breese *et al.*, "bibfield journal "bibinfo journal Nucl. Instrum. Methods Phys. Res., Sect. B" "textbf "bibinfo volume 171," "bibinfo pages 387 ("bibinfo year 2000).

[149] H.L. Seng *et al.*, "bibfield journal "bibinfo journal Nucl. Instrum. Methods Phys. Res., Sect. B" "textbf "bibinfo volume 215," "bibinfo pages 235 ("bibinfo year 2004).

[150] J. P. Dismukes, L. Ekstrom, and R. J. Paff, "bibfield journal "bibinfo journal The Journal of Physical Chemistry" "textbf "bibinfo volume 68," "bibinfo pages 3021 ("bibinfo year 1964).

[151] V. Guidi *et al.*, "bibfield journal "bibinfo journal J. Phys. D" "textbf "bibinfo volume 42," "bibinfo pages 182005 ("bibinfo year 2009).

[152] J. C. Aubry, T. Tyliszczak, A. P. Hitchcock, J. M. Baribeau, and T. E. Jackman, "bibfield journal "bibinfo journal Phys. Rev. B" "textbf "bibinfo volume 59," "bibinfo pages 12872 ("bibinfo year 1999).

[153] D. De Salvador *et al.*, "bibfield journal "bibinfo journal AIP Conference Proceedings" "textbf "bibinfo volume 1530," "bibinfo pages 103 ("bibinfo year 2013"natexlaba).

[154] D. De Salvador *et al.*, “bibfield journal “bibinfo journal Journal of Applied Physics“ “textbf “bibinfo volume 114,“ “bibinfo eid 154902 (“bibinfo year 2013“natexlabb).

[155] S. Carturan *et al.*, “bibfield journal “bibinfo journal Materials Chemistry and Physics“ “textbf “bibinfo volume 132,“ “bibinfo pages 641 (“bibinfo year 2012).

[156] D. Lietti, A. Berra, M. Prest, and E. Vallazza, “bibfield journal “bibinfo journal Nuclear Instruments and Methods in Physics Research Section A: Accelerators, Spectrometers, Detectors and Associated Equipment“ “textbf “bibinfo volume 729,“ “bibinfo pages 527 (“bibinfo year 2013).

[157] N. Shul’ga and A. Greenenko, “bibfield journal “bibinfo journal Physics Letters B“ “textbf “bibinfo volume 353,“ “bibinfo pages 373 (“bibinfo year 1995).

[158] S. Bellucci *et al.*, “bibfield journal “bibinfo journal Phys. Rev. Lett.“ “textbf “bibinfo volume 90,“ “bibinfo pages 034801 (“bibinfo year 2003).

[159] A. G Afonin *et al.*, “bibfield journal “bibinfo journal Nuclear Instruments and Methods in Physics Research Section B: Beam Interactions with Materials and Atoms“ “textbf “bibinfo volume 234,“ “bibinfo pages 122 (“bibinfo year 2005), ¡ce:title¿Relativistic Channeling and Related Coherent Phenomena in Strong Fields¡/ce:title¿.

[160] N. Barrière *et al.*, “bibfield journal “bibinfo journal Journal of Applied Crystallography“ “textbf “bibinfo volume 43,“ “bibinfo pages 1519 (“bibinfo year 2010).

[161] V. Bellucci, R. Camattari, V. Guidi, I. Neri, and N. Barrire, “bibfield journal “bibinfo journal Experimental Astronomy“ “textbf “bibinfo volume 31,“ “bibinfo pages 45 (“bibinfo year 2011“natexlaba).

[162] V. Bellucci, R. Camattari, V. Guidi, and A. Mazzolari, “bibfield journal “bibinfo journal Thin Solid Films“ “textbf “bibinfo volume 520,“ “bibinfo pages 1069 (“bibinfo year 2011“natexlabb), ¡ce:title¿Special Section: Proceedings of 7th International Workshop on Semiconductor Gas Sensors¡/ce:title¿.

[163] A. G. Afonin *et al.*, “bibfield journal “bibinfo journal Instruments and Experimental Techniques“ “textbf “bibinfo volume 54,“ “bibinfo pages 1 (“bibinfo year 2011).

[164] Afonin, A.G. *et al.*, “bibfield journal “bibinfo journal Journal of Experimental and Theoretical Physics Letters“ “textbf “bibinfo volume 67,“ “bibinfo pages 781 (“bibinfo year 1998).

[165] Z. Su and P. Coppens, “bibfield journal “bibinfo journal Acta Crystallographica Section A“ “textbf “bibinfo volume 53,“ “bibinfo pages 749 (“bibinfo year 1997).

[166] H. Backe *et al.*, "bibfield journal "bibinfo journal Nucl. Instrum. Methods Phys. Res., Sect. B" "textbf "bibinfo volume 266," "bibinfo pages 3835 ("bibinfo year 2008), radiation from Relativistic Electrons in Periodic Structures.

[167] J. Bak *et al.*, "bibfield journal "bibinfo journal Nuclear Physics B" "textbf "bibinfo volume 254," "bibinfo pages 491 ("bibinfo year 1985).

[168] S. Strokov *et al.*, "bibfield journal "bibinfo journal Journal of the Physical Society of Japan" "textbf "bibinfo volume 76," "bibinfo pages 064007 ("bibinfo year 2007).

[169] A. Kostyuk, "bibfield journal "bibinfo journal Phys. Rev. Lett." "textbf "bibinfo volume 110," "bibinfo pages 115503 ("bibinfo year 2013).

[170] D. Adejshvili *et al.*, "bibfield journal "bibinfo journal Radiation Effects" "textbf "bibinfo volume 87," "bibinfo pages 135 ("bibinfo year 1985), http://www.tandfonline.com/doi/pdf/10.1080/01422448508205209 .

[171] Y. Ivanov, A. Petrunin, and V. Skorobogatov, "bibfield journal "bibinfo journal Journal of Experimental and Theoretical Phys. Lett." "textbf "bibinfo volume 81," "bibinfo pages 99 ("bibinfo year 2005).

[172] M. Kiru, Kezuru, "Dicing before grinding (dbg) process," http://www.disco.co.jp/eg/solution/library/dbg.html.

[173] G. F. C. Searle, *Experimental elasticity* (Cambridge University Press, Cambridge, 1920).

[174] M. Tobiyama *et al.*, "bibfield journal "bibinfo journal Phys. Rev. B" "textbf "bibinfo volume 44," "bibinfo pages 9248 ("bibinfo year 1991).

[175] V. Baryshevsky and V. Tikhomirov, "bibfield journal "bibinfo journal Nuclear Instruments and Methods in Physics Research Section B: Beam Interactions with Materials and Atoms" "textbf "bibinfo volume 309," "bibinfo pages 30 ("bibinfo year 2013).

[176] V. Biryukov, "bibfield journal "bibinfo journal Physics Letters A" "textbf "bibinfo volume 205," "bibinfo pages 340 ("bibinfo year 1995"natexlabc).

[177] R. Assmann *et al.*, Proc. of European Particle Accelerator Conference: EPAC'02 , Report (2002).

[178] M. Pesaresi, W. Ferguson, J. Fulcher, G. Hall, M. Raymond, M. Ryan, and O. Zorba, "bibfield journal "bibinfo journal Journal of Instrumentation" "textbf "bibinfo volume 6," "bibinfo pages P04006 ("bibinfo year 2011).

[179] E. B. Holzer *et al.*, Proc. of HB2010 , CERN (2010).